Development of a Precipitation Free High-Nitrogen Alloy

by

Neeraj Karmarkar

**A dissertation submitted in partial fulfillment
of the requirements for the degree of
Doctor of Philosophy
(Mechanical Sciences and Engineering)
in the University of Michigan-Dearborn
2022**

Doctoral Committee:

**Professor Pravansu S Mohanty, Chair
Assistant Professor Tanjore V. Jayaraman
Associate Professor German Reyes-Villanueva
Professor Ya Sha Yi**

Neeraj Karmarkar

nkarmark@umich.edu

ORCID iD: 0000-0003-3376-6611

Dedication

This dissertation work is dedicated to all my family members and my beloved friends!

Acknowledgements

This journey of doctoral research has been a blissful adventure. A fruitful dissertation always has a strong backing of a team continuously supporting and guiding. I would like to take this opportunity to thank everyone involved in this journey of mine. I would like to thank my advisor Dr. Pravansu Mohanty who let me take up this innovative research topic and provided me necessary resources required to complete the research. I am grateful for his invaluable guidance and support to make this work possible. He has taught me to be an independent and innovative thinker. I express immense gratitude to my teammates Dr. Vikram Varadaraajan and Sharan Nagendiran for their continuous technical guidance. This study would have been impossible without their mentorship. A million thanks to William Walker (Billy) for assisting in sample preparation throughout the study. I am also thankful to my colleagues Ramcharan Palacode Visweswaran, Aniket Jadhav, Animesh Koneru. I would like to thank faculty and staff at Michigan Center for Materials Characterization - (MC)^2, Ann Arbor (Michigan) for providing the training on the use of analytical instruments: Dr. Bobby Kerns, Dr. Nancy Muyanja, Dr. Haiping Sun, Dr. Allen Hunter, and Ms. Deanna Wendel. This research period would have been no fun without my roommates and friends who kept me motivated and energetic the whole time. Thank you, Mayuresh, Prakash, Sanket, Ruturaj, Vishwajeet, Abhishek M, Abhishek K, Shantanu, Saurabh, Archana, Varun, Omkar, Prajwal, Narendra for all the fun times.

I am grateful towards my parents for their countless sacrifices and well-wishes. Their constant support let me sail this research journey very easily. Love you Ma and Pa!

Table of Contents

List of Figures

List of Equations

List of Tables

Abstract

High nitrogen steels provide excellent mechanical properties and corrosion resistance but are prone to form precipitates which adversely affect the corrosion resistance and toughness. High nitrogen steels available in the market are not claimed to be precipitate free. It is critical to avoid these precipitates and retain nitrogen in the dissolved form to realize the value of these alloys.

This study presents development of a high nitrogen ferrous powder precursor. The translation of this powder precursor to a functional coating is also discussed. To achieve dissolved nitrogen in the composition, two approaches are discussed. Retaining nitrogen by rapid solidification to bypass the $L \rightarrow \delta$ reaction promoting the $L \rightarrow \gamma$ reaction directly, where the nitrogen solubility is high is one possible route. The initial alloy design was done using such rapid solidification process with pre-formed nitrides to determine the right composition for desired mechanical and corrosion properties. This rapid-solidification approach was studied in detail by a few team members from the AMPL group at the UM-Dearborn. This study elaborates more of the solid-state dissolution route to avoid the molten state of the material. A solid-state solution annealing is proposed to treat a ferritic powder alloy (α-Fe) at high temperature in presence of nitrogen further quenching it to stabilize austenite at room temperature in-order to retain the dissolved nitrogen in the composition.

Pre-atomized nitrogen steel powders readily available in the market were also evaluated for their precipitations. A heat treatment of the nitrogen powder in inert argon media was considered to minimize /eliminate the nitrides.

In-order to evaluate the performance of these prepared precursors, coating development by cold-spray is considered. Cold spray being a solid-state deposition technique is carried out at low

temperatures which do not lead to any thermal phase transformations in the coatings as of the starting precursors. Low process temperatures maintaining the thermal equilibrium make cold spray an ideal candidate for coating development. The dissolved nitrogen content in the powder precursor can thus be easily maintained during this solid-state deposition. The properties of the material can be thus assessed in terms of a coating as there is possibly no chemical/metallurgical change from powder precursor to coating. Deposition efficiency was considered as a key performance parameter for different precursors. Mechanical properties, tribological properties and corrosion properties of the coatings were evaluated.

In-order to make an optimized use of these recent techniques in thermal spray and additive manufacturing family, it has been driving researchers to make use of artificial intelligence and machine learning techniques. Narrowing down to the current study, cold-spray technique has numerous parameters which affect the deposition quality. In-order to achieve an optimum parameter for deposition, numerous experiments are required which in-turn is time consuming and cost ineffective. A prescriptive data model is proposed in this study which uses a set of few experiments to develop a training data set in-order to predict the coating quality in terms of the deposition efficiency as well as porosity. This supervised prescriptive approach can be used as a tool in-order to achieve an optimized coating parameter to get the desired properties before performing the experiments. This algorithm could also be used in the nozzle design of the system to optimize for maximum particle velocity of the precursors which directly affects the deposition quality.

Chapter 1 Introduction

1.1 Steels-A Backbone of the Metal Industry

Ferrous alloys with a carbon content up to 2% widely known as steels are one of the most valued components in the metal industry. Processing of steels cycles back to the industrial age where the mankind started synthesizing steels as per their needs right from small tools to huge machineries. Alloying of steels has been evolving since, in-order to achieve enhanced properties in various applications. The main constituents in steels being Chromium, Nickel and Manganese and minor alloying elements like Carbon, Silicon, Aluminum, and Molybdenum help in retaining the mechanical strength and its chemical properties. Addition of Nitrogen to enhance these properties has also been picked up by the industry.

By altering the alloying constituents' steels are categorized as follows [1]:

⇒ Low Alloy steels (Low Carbon, Medium Carbon, High Carbon)

This category of steels is prone to corrosion attack and the mechanical properties are sensitive to carbon content. Increasing the carbon content makes the steel more brittle [1].

⇒ High Alloy Steels (Tool steels, Stainless Steel)

This category is heavily used in the industry. Steels may have a dominant phase of iron depending upon the synthesis of the alloy. A stable ferrite phase (α) which has a BCC structure or a stable Austenite (γ) phase having FCC structure are possible [1]. Depending upon the application of the alloy as well as the manufacturing process, the stable phases are determined. Recently duplex steels, having a combination of both ferrite and austenite are also used to combine advantages of both α & γ phases.

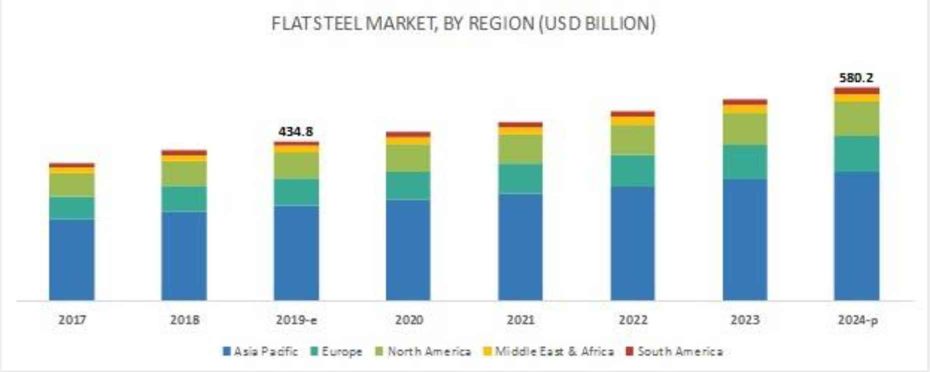

Fig 1.1 Growing Steel Market Forecast in the United States [2]

1.2 High Nitrogen Steels

Steels are a very generic term corresponding to its passive protective layer of chromium and other alloying contents also play a huge role in its performance [3]. Steels with Nitrogen included in the composition have been receiving tremendous research attention since late 60's. The main reason being Nitrogen providing significant improvement in yield of these steels. A steel with nitrogen content more than its solubility limit is coined as high nitrogen steel. Nitrogen is a heavy austenite stabilizer which occupies the octahedral positions in the FCC lattice (γ) [4, 5, 6]. Fig 1.2 shows the tetrahedral & octahedral positions occupied by Nitrogen atoms in Ferrite (α→BCC) and Austenite (γ→FCC) lattice respectively. The nitrogen atoms prefer the octahedral sites since the octahedral interstitial size is greater in FCC then in BCC lattice [4] making its volume larger.

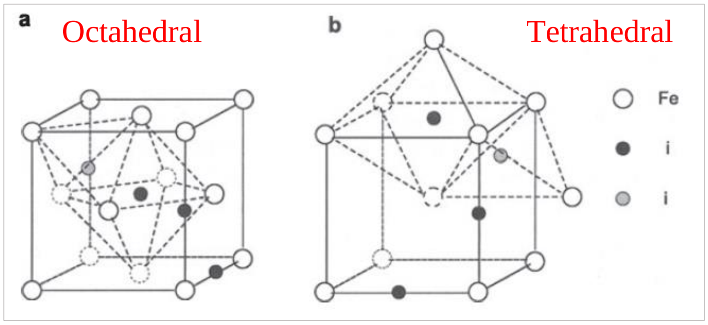

Fig 1.2 Positions Occupied by N/C in a) FCC b) BCC Lattice [4]

Fe-Mn-Cr-N system is one of the demanding branches of HNS with no nickel in the composition, however; Mn and N contents are responsible for austenite stabilization. These non-magnetic steels are in heavy demand in the oil industry.

Nitrogen has significant effect on the stacking fault energy (SFE) which in turn affects the dislocation. Petrov observed an increase in SFE for a Fe-Cr13-Mn19 alloy with nitrogen from 0.05-0.23 wt. % [7]. The increase or decrease of SFE due to nitrogen is still not distinct. A wide range of SFE has been reported before and after nitrogen uptake. The value of SFE essentially depends upon the free electrons in the alloy which directly correlates to the composition. The deformation mechanisms of these HNS alloys are dependent on a high/low SFE due to nitrogen uptake. This high/low SFE value corresponds to the constrained/unconstrained dislocation motions affecting the deformation. Fig 1.3 shows dislocation structure of a Cr15Mn17 alloy with Nitrogen varying from 0.22-0.45%N. A drop in dislocation energy from 25.5 J/m^2 to 17.7 J/m^2 was reported [4].

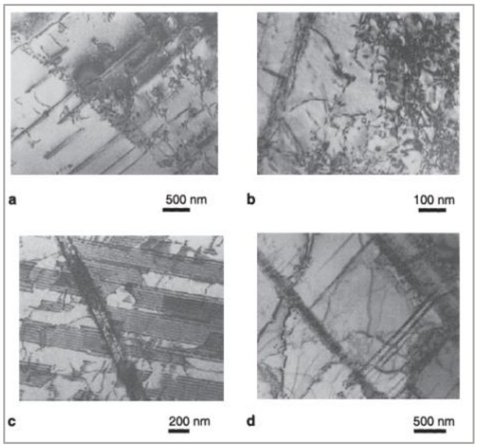

Fig 1.3 Dislocation Structure in Cr15Mn17 Steels a,b) 0.22%N ;c,d) 0.45%N

1.2.1 Mechanical Properties

Nitrogen as an alloying element in steel causes significant improvements in properties. In particular; an unusual combination of the yield strength and fracture toughness with improved corrosion resistance.

Irvine et al. [8] derived an empirical equation for determining yield strength ($Rp_{0.2}$) and ultimate strength (Rm) of steels dependent on composition as mentioned in Equation 1-1 and Equation 1-2

Equation 1-1 Yield Strength at 0.2% Strain Offset

$$Rp_{0.2} = 63.5 + 496N + 356.5C + 20.1Si + 3.7Cr + 14.6Mo + 18.6V + 4.5(W, \%)$$
$$+ 40.3Nb + 26.3Ti + 12.7Al + 2.5\delta + 7.1d^{-1/2},$$

Equation 1-2 Ultimate Strength

$$Rm = 449.5 + 852.5N + 542.5C + 37.2Si - 1.5Ni + 18.6Mo + 77.5Nb + 46.5Ti + 18.6Al + 2.2\delta + 7.1t^{-1/2}$$

δ is the content of δ -ferrite in vol. %, d is the grain size in nm and t is the number of twins per mm. This led to a conclusion that at ambient temperature, nitrogen is about 1.5 times more effective in strengthening the austenite as compared to carbon.

The yield strength of nitrogen in solid solution is dependent on 2 main factors: a) R_a being athermal strengthening and b) the second one R_T exhibiting a temperature dependence originating from a thermally activated overcoming of obstacles by moving dislocations [4].

1.2.2 Chemical Properties

Corrosion resistance is a unique feature of High nitrogen steels. Steels are usually rated by their resistance to pitting corrosion quantified by a number called PREN. An empirical relation previously coined by a few researchers is mentioned in Equation 1-3. The amount of Chromium, and nitrogen significantly affect the PREN. Hence Nitrogen plays a vital role affecting the corrosion performance of HNS [9].

Equation 1-3 Empirical Equation for PREN [4, 10, 3]

$$PREN = \%Cr+3.3\times\%Mo+16\times\%N.$$ [4, 10, 3]

A resistance to local corrosion which includes crevice corrosion, pitting corrosion etc. has majorly been reported to enhance by nitrogen uptake from 0.05 wt% upto 0.38wt%. Increase in nitrogen content has also been reported to improve the pitting resistance as well as resistance to stress corrosion cracking [9]. Corrosion reaction leads to the formation of NH_3 (Ammonia), increasing the pH value which leads the electrolyte to be less acidic making the corrosive attack mild [11]. HNS have an improved passivity primarily due to elemental Nitrogen as well as segregation of other alloying elements typically Mn, Cr and Ni [11]. The passivation is improved by the oxy-nitride layer [11].

1.2.3 Manufacturing of HNS

HNS can be manufactured by many traditionally established methods. Some of them like PESR (pressurized electro-slag remelting), HIP (High isostatic pressure melting) are well known to produce high quality HNS [5].

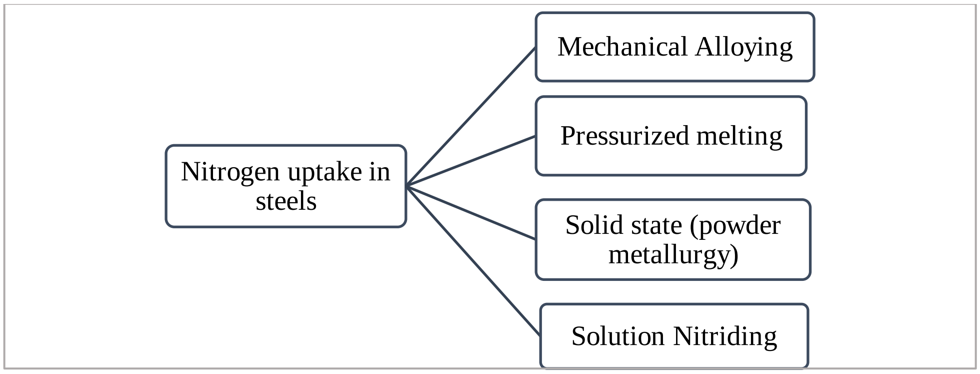

Fig 1.4 Possible Mechanisms for Improved Solubility of Nitrogen

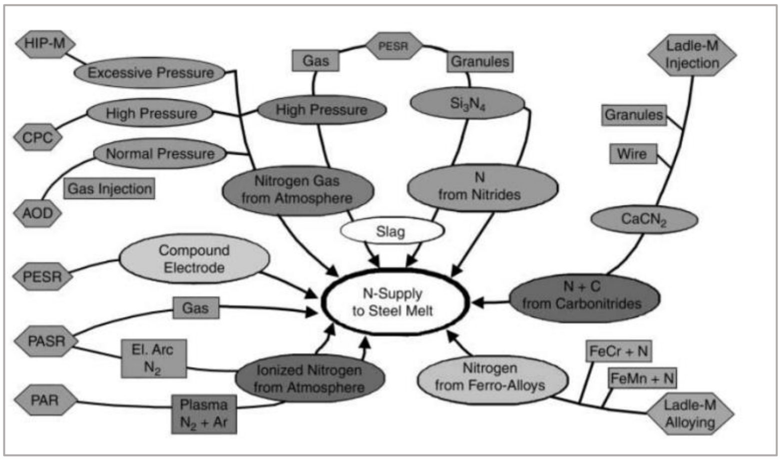

Fig 1.5 Possible Mechanisms of Nitrogen Uptake in the Melt [12]

- Open air melting:

Open air melting was initiated and patented by Schumacher et. al [13]. They manufactured High-nitrogen and nitrogen free compositions on a commercial basis. Electroslag remelting (ESR) is one of the most frequently used open-air melting techniques. In this process, an electrode is prepared by casting or forging. The electric resistance of the slag leads to melting of the electrodes As the electrode starts to atomize in the form of droplets, material refining begins and is collected at the bottom of the equipment. ESR process can ensure purity and cleanliness of the material.

The problem of macro-segregation can be eliminated in this process along with a homogenous distribution of desired alloyed elements. Presently, this technique is used for manufacturing heat-resistant steels such as Cr-Mo-V steels, advanced Cr-Mo-V steels and various 12Cr steels [14]. However, manufacturing of nitrogen steels with a higher nitrogen content is challenging due to open pressure.

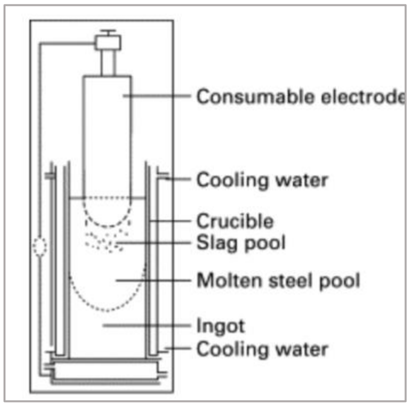

Fig 1.6 Schematic of a Typical ESR Setup [14]

- Pressure metallurgy

Increase in the system pressure above the atmospheric has shown to aid the nitrogen solubility to a greater extent. Nitrogen pickup, which takes place at the interface between molten metal and gas via the reaction N2 → 2N. Nevertheless, this type of furnace is excellent suitable for small experimental heats of up to 100 kg. Research has shown to improve the nitrogen content in CrMn steels from 0.35 wt. % to 0.42 wt.% using this technique.

  - Pressure electro slag remelting (PESR):

Pressure Electro Slag Remelting (PESR) has emerged as one of the processes for producing high nitrogen steels. This process involves solidification where nitrogen is introduced in the melt by dissolving nitrogen additives [15]. According to sievert's law nitrogen solubility is directly proportional to the square root of pressure of the system as shown in Equation 1-4.

Equation 1-4 Sievert's Square Root Law

$$\%N = k.\sqrt{P_{N2}}$$

The PESR process is a traditional remelting technique which operates under a certain pressure. This technique achieves both an ESR refining, and nitrogen pick up in steels. The metallurgical approach is identical to ESR melting.

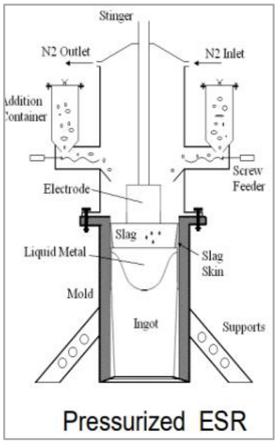

Fig 1.7 Schematic of PESR Setup Developed by Carpenter Technologies [15]

- Mechanical alloying:

Mechanical alloying is also one of the solid-state techniques considered for nitrogen addition in the composition [16]. Metal powders undergo cold-work in high-energy attrition ball milling which in-turn leads to nano grain structure. Mechanical alloying has been shown to increase the interstitial concentration of carbon in iron, although having a very low solubility limit for interstitial solid solution with nitrogen without precipitation [17].

Chapter 2 Background

Current processes of manufacturing viz. PESR, HIP melting etc. subject the alloy to a molten state followed by solidification in form of ingots. Given its multiple advantages; the current manufacturing processes of HNS have a few limitations. An oxide layer present on the alloy surface is detrimental towards the nitrogen uptake. During the solidification process of these alloys the transformation of L→ L+δ-ferrite takes place [5]. Due to this small region of δ-ferrite, much of the dissolved nitrogen content is lost due to a significantly reduced N solubility. Despite the further transition to γ (L+ δ →γ or δ →γ); the nitrogen cannot be re-dissolved even with its higher solubility in γ [18, 19].

Nitrogen in the steels can be present in the form of Cr-N short range order (SRO). CrN is an interstitial compound, in which nitrogen atoms reside in the octahedral spaces between the chromium atoms in an FCC lattice. During CrN formation in steels another compound called metallic dichromium nitride is also formed. (Cr_2N) [20, 21, 22, 23]. Dichromium Nitride (Cr_2N) is most likely to be formed in the ferritic (α) / austenitic (γ) phase of the steel [4, 3, 22, 24].

The cooling rates are also responsible for this precipitation of stoichiometric compounds. These phases/compounds are brittle in nature which is detrimental towards the strength of the alloy. Stable nitrides are typically formed at temperatures above 600°C [4]. Slow cooling during ingot formation or atomization of powders is one of the primary causes of nitride formation. Furthermore, the precise control of concentration of nitrogen in the entire composition is a challenge [25].Further di-chromium nitride (Cr_2N) precipitation often coined as “false pearlite” is typical in HNS. It is a biproduct of the eutectoid reaction $\gamma \rightarrow \gamma' + Cr_2N$ affecting the alloy performance [26, 27]. This undesirable compound is governed by diffusion of Cr atoms N atoms over a long spacing range [27, 28]. Formation of a covalent short-range order of Cr-N is also typical, although has not been reported to deteriorate the performance [18]. Research shows these Cr_2N precipitations to diminish the mechanical properties like toughness as well as corrosion properties of the alloys [21, 29, 18, 27, 3, 24, 30, 19]. This compound contains more chromium due to its stoichiometric ratio compared to short range Cr-N. This attributes towards depletion of chrome giving rise to more electrochemical activity thus impairing the corrosion resistance [31, 32]. Dissolved nitrogen is known to improve the stacking fault energy (SFE) due to the formation interstitial solid solution enhancing its strength [33]. However, formation of Cr_2N can affect the distribution of alloying elements within the crystal and diminish the essence of interstitial solid solution and the SFE [18, 19]. It has a trigonal structure as shown in Fig 2.1.

The addition of nitrogen improves the strength, ductility, and impact toughness in austenitic steels, while the fracture strain and fracture toughness are not affected at elevated temperatures. The strength of nitrogen alloyed austenitic steels arises from three components: strength of the matrix, grain boundary hardening, and solid solution hardening. The matrix strength is not appreciably impacted by nitrogen, rather correlates to the friction stress of the FCC (face centered cubic) lattice that is mainly controlled by the solid solution hardening of the substitutional elements like chromium and manganese. But grain boundary hardening which occurs due to dislocation blocking at the grain boundaries, increases proportionally to the alloyed nitrogen content. The highest impact on the strength results from the interstitial solid solution of nitrogen. Nitrogen increases the concentration of free electrons promoting the covalent component of the interatomic bonding and the formation of Cr-N short range order (SRO). Tweaking this SRO can enhance the strength, ductility, and impact toughness of the alloy which is affected by its stacking faults and dislocations [18]. However, the formation of nitrides such as Cr_2N, TiN, AlN, etc. at elevated N content, affects the distribution of alloying elements within the lattice and in turn diminishes the bulk effect of interstitial solid solution and the SFE. The formation of nitrides such as Cr_2N occurs when the nitrogen content goes beyond a certain threshold value (depends on the overall composition of the alloy) and should be discouraged to take advantage of the interstitial solid solution hardening phenomenon described above [18].

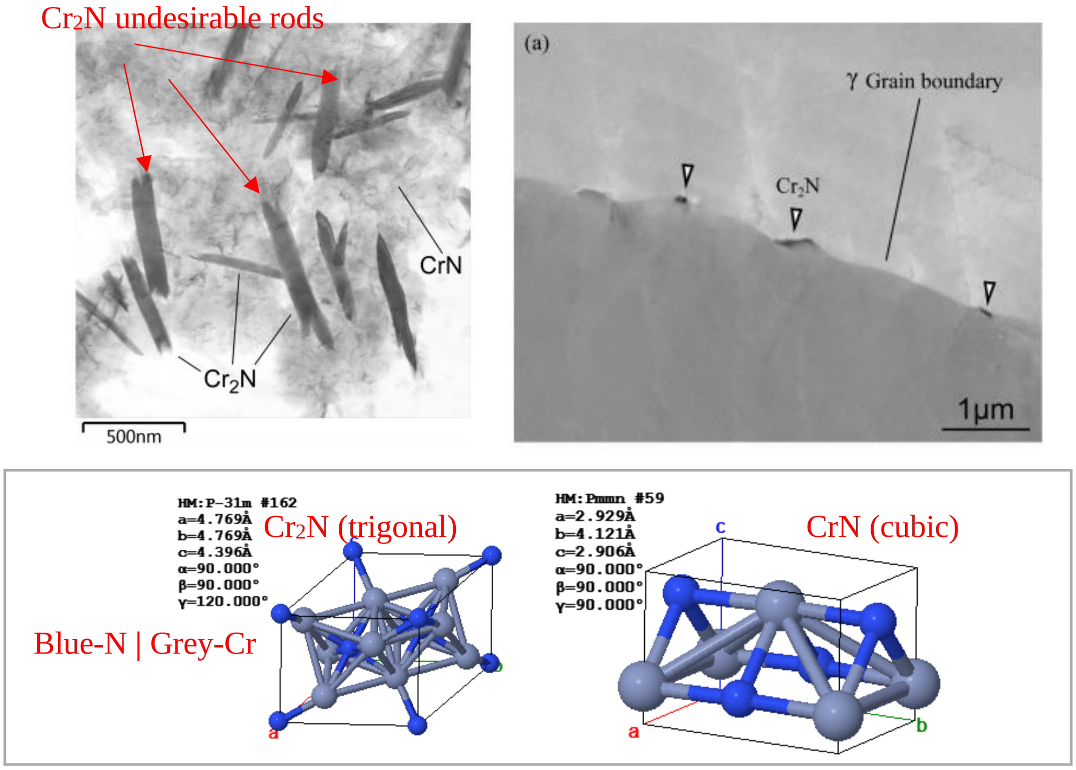

Fig 2.1 Cr_2N Rods and CrN Lattice With Their Crystal Structures (FCC) [3, 34]

In austenitic stainless-steel nitrogen stabilizes the austenitic phase, improves the mechanical properties, and increases the corrosion resistance. Nitrogen alloying enables to produce austenitic steels without the element nickel which is high priced and classified as allergy inducing. A novel production route is nitrogen alloying of CrMn-prealloyed steel powder via the gas phase. This is beneficial as the nitrogen content can be adjusted above the amount that is reached during conventional casting. A problem which must be overcome is the oxide layer present on the powder surface which impedes both the sintering process and the uptake of nitrogen. This study focuses to analyze if heat treatment under pure nitrogen is an appropriate procedure to enable sintering and nitrogen uptake by reduction of surface oxides. X-ray photoelectron spectroscopy (XPS) in combination with scanning electron microscopy (SEM) and energy dispersive X-ray spectrometry (EDS) are used to investigate the surface of powdered FeMn19Cr17C0.4N heat treated under nitrogen atmosphere. The analyses showed reduction of iron oxides already at 500 °C leading to oxide-free metallic surface zones. Mn and Cr oxides are reduced at higher temperatures. Distinct nitrogen uptake was registered, and successful subsequent sintering was reached

Anna Weddeling et al. [35] attempted a nitrogen alloying route using a Cr-Mn pre-alloyed steel powder by a gas phase. This study focused on heat treatment of metal powders (solid-state dissolution) under presence of nitrogen atmosphere. The investigations elaborate more on the XPS maps of the treated powders. The oxide layer formation prevented further uptake of nitrogen. CrN/Cr_2N peaks were observed as shown in Fig 2.2. Although this study used a solid-state dissolution, sintered compacts were used for the uptake. This method was thus helpful in manufacturing powder compacts with high nitrogen; all be it a novel method is necessary to avoid sintering of the powders to increase their usability in other manufacturing techniques.

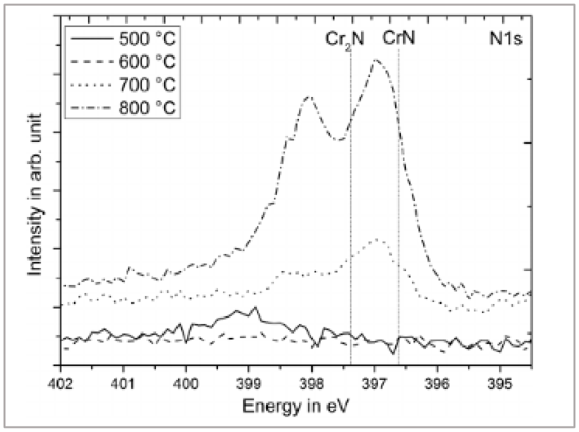

Fig 2.2 XPS Results After Heat Treatment of HNS Alloys [35]

Thus, making use of powder metallurgy to produce HNS is also an avenue to be considered. Interstitial solid solution could be easily formed by this route because of high solubility limit in slid state as well as a low absorption time required [36]. Fig 2.3 represents a proposed thermal history to avoid sintering as well as precipitation of the nitride phases. These parameters were derived from experiments and techniques mentioned in proprietary document by the author group [18, 19].

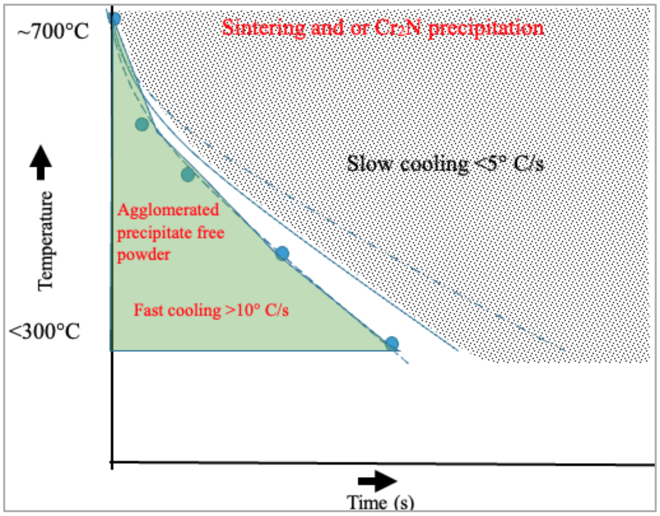

Fig 2.3 Schematic of Proposed Cooling Mechanism to Avoid Nitride Precipitation [18, 19]

Chapter 3 Objective, Scope, Research Approach & Workflow

3.1 Objective

As discussed in the introduction, overcoming the limitations of high nitrogen steels will escalate its demand by a very significant level i.e., by eliminating the obstacles caused by the presence of intermetallic/non-metallic phases present in the HNS. The objective of this study is thus to conceptualize an economical manufacturing process to retain dissolved nitrogen in the composition and to produce functional coatings with the same alloy. The primary objective of alloy development would be elimination/minimization of stoichiometric compounds formed, typically Cr_2N.

Optimization of manufacturing process is also a significant concern during commercialization. A data model is also considered which provides a supervised machine approach to optimize the cold-spray deposition process.

3.2 Scope

This study focuses on the development of a High Nitrogen steel (HNS) with dissolved nitrogen and its feasibility to upscale the process for commercial manufacturing. All the technical aspects in-terms of characterization are considered. The study does not include any case-study of the manufactured alloy / coating. A commercially available nitrogen steel is also evaluated for a nitride-free matrix.

The derived data-model presents a concept which can be deployed to optimize the cold-spray process. A training dataset using commercially available 316 SS powders is built. The developed high nitrogen precursor is not considered in the data model due to its limited lab-scale development.

3.3 Research Approach

In-order to retain dissolved nitrogen in the interstitial of γ, 3 approaches are considered.

1. An alloy with preformed nitrides e.g. SiN;Mn_xN_y;Fe-N etc. subjected to a rapid solidification technique involving high cooling rates to dissolve the nitrides.
2. An alloy with a desired composition solution annealed in the presence of nitrogen media; followed by quenching the alloy to prevent nitride formation.
3. Evaluation of pre-atomized nitrogen powders available in the market for their nitride contents and post processing of these alloys for elimination of nitrides.

Nitrogen uptake during rapid solidification	Solid state nitrogen uptake in γ (Preferred option)	Post-treatment of Pre-atomized nitrogen powders
• Use of pre-formed nitrides for N uptake • Low solubility limit of Nitrogen • Crosses δ-ferrite region during solification→ precipitation of Cr_2N • low diffusion rates due to low contact area • Rapid solidification required to achieve to bypass L→δ-ferrite reaction and promote L→γ transition	• Use of N media • Extended Solubility limit of nitrogen • Elimination of δ-ferrite region due to existing γ phase • High diffusion rates due to Maximum contact area • Quick temperature ramp • Low dwell/residence times • High cooling rates possible due to more exposed area of particles	• Use of inert media • Solid-state solution annealing will aid in removal of precipiates followed by faster cooling rates to reatin dissolved nitrogen.

Fig 3.1 Nitrogen Uptake Techniques

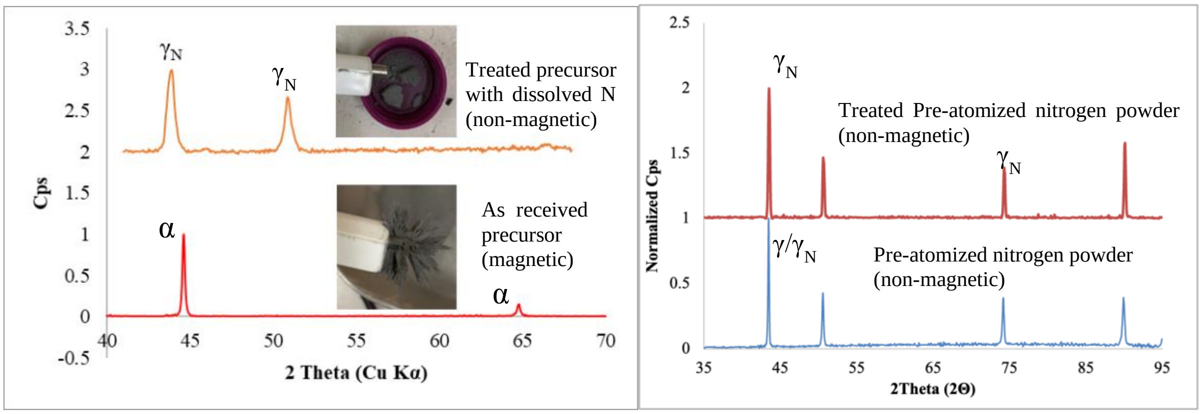

Fig 3.2 Phase Transitions with Proposed Powder Treatment

3.4 Workflow

This study will be divided in 2 main sections. The initial part of the research will focus on development of a high nitrogen precursor used to develop functional coatings with the help of cold-spray technique. The later part will focus on optimization of the cold-spray process using a SS136 precursor study and development of a data model.

3.4.1 Material Development

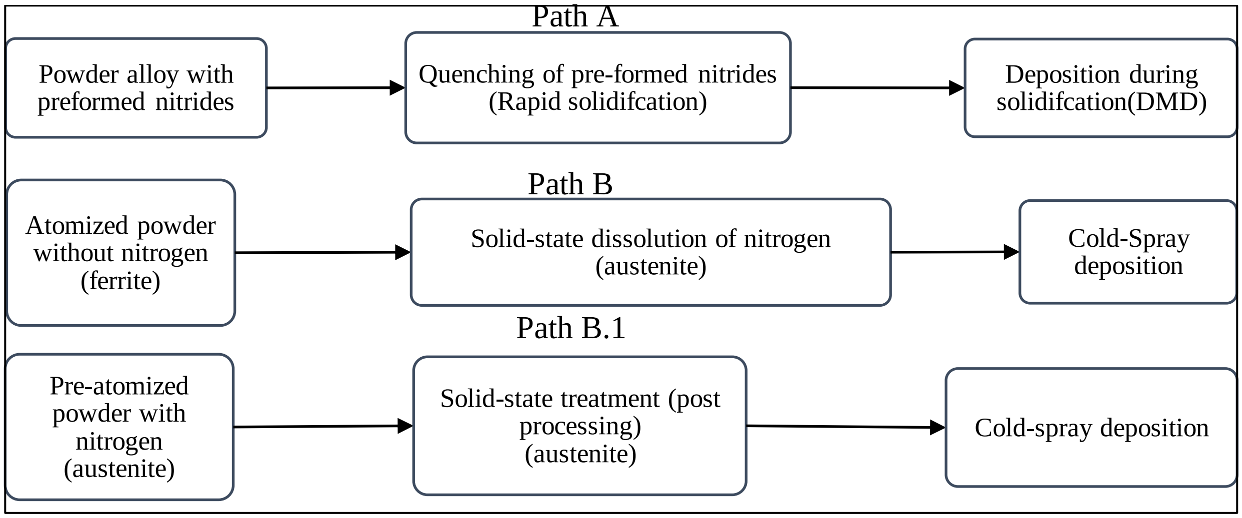

Fig 3.3 Research Approach Flow Chart

3.4.2 Algorithm/Data Model Development

Narrowing down to the current study, cold-spray deposition technique has numerous parameters which affect the deposition quality. In-order to achieve an optimum parameter for deposition, numerous experiments are required which in-turn is time consuming and cost ineffective. A prescriptive data model is proposed in this study which uses a set of few experiments to develop a training data set in-order to predict the coating quality in terms of the deposition efficiency as well as porosity of the coating. This supervised prescriptive approach can be used as a tool in-order to achieve an optimized coating parameter to get the desired properties before performing the experiments. This algorithm could also be used in the nozzle design of the system to optimize for maximum particle velocity of the precursors which directly affects the deposition quality. A supervised machine learning algorithm is considered. The data model will be split in 2 different approaches for prediction.

3.5 Analysis Techniques

3.5.1 Microstructural Characterization

Microstructural characterization of the powders and cold-sprayed coatings was done with scanning electron microscopy (Secondary/Back scattered images) on a Hitachi S-3600N SEM to analyze the grain size and the quality of the powders and the coating. Standard metallographic procedures were followed using an epoxy resin to prepare mount samples for the SEM. Etching was carried out to reveal the microstructure grains of the precursor (powder). A Rigaku Miniflex X-ray Diffractometer (Cu Kα radiation λ~1.5402Å) was used to determine the phases in the powders as well as the coatings. Fluorescence was observed in the diffraction patterns due to the Cu Kα radiation (8.04 keV) being

Fig 3.4 Rigaku Miniflex XRD

greater than that for all the samples used → Mn Kα (5.894 keV), Fe Kα (6.398 keV) [37]. Background removal/reduction was further done to eliminate the fluorescence using the commercially available XRD software Jade 7. Indexing of peaks was done by importing JCPDS files for every phase [38]. Electron Back Scattering Diffraction measurements (EBSD) were carried out on powder precursors to observe the grain size and crystallographic orientation of the powder grains. A Tescan MIRA SEM with an EBSD detector was used for the measurements at the MC^2 lab in Ann Arbor. Diffraction patterns were recorded at a 30kV signal with a beam intensity of 20. Swab etching was carried out using Adler's etchant in-order to reveal the grain boundaries on powders and coatings. A standard concentration of 1:1 by volume was used with an etching time varying from 5-10 seconds.

3.5.2 LECO Analysis

Fig 3.5 LECO 736 Analyzer

Nitrogen measurement on the powders and developed coatings was done using a combustion method on a LECO analyzer. The measurements were done at Element Materials Technology, Wixom, MI [39]. A sample with known weight is placed in a graphite crucible which when heated to elevated temperature liberates various gases. Oxygen reacts with the crucible to form CO and CO_2. Inert gas, typically helium is used to sweep the gas out of the system. Oxygen is converted to CO_2; and Hydrogen is converted into H_2O which is later scrubbed out of the system. A thermal conductivity detector later measures the remaining Nitrogen in the sample [40].

3.5.3 Differential Scanning Calorimetry

To understand the phase transition properties of the FMC-AS powder, heat flow measurements were recorded using a differential scanning calorimetry (DSC). A Q600 SDT analyzer by TA instruments was used. A melting spectrum was obtained characterized by endothermic peaks. A heat cycle from 24°C to 1200°C at a rate ramp rate of 10°C/min was used. Pure argon was used as a shield gas for these measurements. A solidification behavior of the alloys was also observed using a ramp rate of 10°C/min to equilibrate at 50°C.

3.5.4 Micro-Hardness

The micro hardness was measured on the coatings using a Vickers Hardness equipment (Streurs, USA). A load of 10gF and 300gF for 20 secs was applied for hardness measurement on powder particles and on the cold-sprayed coatings, respectively. The indents on the powder cross section were measured on the same particle as well as different particles to ensure homogeneity of the precursor micro-hardness. Micro-hardness on coatings was determined at 3 different positions/locations away from the substrate. An average of 5 readings at each offset from the substrate have been reported.

Fig 3.6 Vickers Hardness Tester

3.5.5 Nano-Indentation

Mechanical properties were also determined using a nano-indentation technique. A hysitron 950 tribometer equipped with a 2D-Berkowich probe (half-angle 65.23°, $E_{indenter}$ =1140GPa, $\nu_{indenter}$=0.07) was used for measurements. Particles >35μm only were considered for nano-measurements to avoid the effect of immersion in epoxy [41]. Load was applied at a constant displacement of 250nm for 5 seconds to avoid the surface effect on the measurements. Multiple indents separated at significant distances were taken on a same particle to prevent local strain effects during indentation.

3.5.6 Wear Characteristics

The tribological properties of the coatings were measured using a CSM ball/pin-on disk tribometer. Machined coatings were used for the testing in order avoid excess loading on the tribometer. A 6mm tungsten carbide ball (WC) (McMaster Carr) was used as a friction media. Test was conducted at room temperature (~24°C) with a 3.25 cm/s sliding speed and a load of 9N for 25000 cycles. Corresponding wear profiles were later measured for a travel span of 6mm using a Mitutoyo Surftest equipment. The resulting plot Ra value v/s the length is reported for repetitive and uniform measurements.

3.5.7 Corrosion Testing-Potentiodynamic /Open Circuit Tests

The corrosion behavior of the coatings was measured by the electrochemical/galvanic technique. An Ag/AgCl and Pt wire were used as reference and counter electrode respectively in a 0.5% NaCl solution used as an electrolyte. Two tests were conducted at room temperature (~25°C) to measure the Open circuit potential (OCP) and the polarization behavior (potentio-dynamic curve).

All the samples were polished up to 1200 grit SiC paper to ensure a 15µm finish with a flat surface for homogenous electrolyte exposure. The collected data was analyzed for Tafel-fitting using a commercially available software (EC-lab).

3.5.8 Corrosion Testing- Zero Resistance Ammetry (ZRA)

ZRA tests were conducted on coatings to analyze the effect of 2 metal corrosion or in other words known as galvanic corrosion. Aluminum A356 alloy was used as a counter electrode for galvanic coupling. All the coatings were benchmarked with standard available materials i.e coldsprayed SS316 coating.

3.5.9 Salt-Bath Testing

An in-house test rig was set-up as per the ASTM B117 [42] standard to check for corrosion performance of the coatings in a 5% NaCl mist. Humidity and temperature of the system were manually controlled and maintained at 100°F.

3.5.10 Analysis Techniques, Abbreviations & Acronyms

This section will brief about the sample names and notations used here forward in this study. Table 3-1 represents a summary of all the analysis techniques used in this study. Table 3-2 presents the abbreviations corresponding to the type of samples. Table 3-3 presents the Sample IDs and their parameters used in the experimental data model.

Table 3-1 Analysis Techniques Used in the Study

Analysis technique	**Motive**	**Sample type**
SEM	To observe the microstructure	Powder & Coatings
Etching	To reveal grain size and structure	Powder & Coatings
EDS	Chemical Composition map	Powder
EBSD	Mis-orientation map / Phase Map for CrN/Cr_2N detection	Powder
Nano-indentation	Mechanical properties of components	Powder & Coatings
LECO analysis (combustion method)	N_2 content achieved	Powder & Coatings
Vickers Hardness	Particle/coating hardness	Powder & Coatings
XRD patterns	Phase Analysis	Powder & Coatings
Corrosion	Polarization behavior	Coatings
Tribological wear and wear depth (profilometer)	Wear characteristics (ball on disk type), and wear rate	Coatings

Table 3-2 Sample Abbreviations Used in the Study

Sample name	**Sample type**	**Comments**
Treatment N1	Treatment parameter (850°C,4hrs dwell)	Used for Mn_xN_y preparation
Treatment N2	Treatment parameter (1000°C,2hrs dwell)	Used for Mn_xN_y preparation
Composition C1	Powder Alloy,Coating (With N1 treatment)	Used for DMD study
Composition C2	Powder Alloy,Coating (With AlN only)	Used for DMD study
Composition C3	Powder Alloy, Coating (With N2 treatment and AlN)	Used for DMD study
Fe271-3	Powder Alloy, Cold-sprayed Coating	Stainless Steel 316 (Gas Atomized, Praxair inc.)
Biodur	Powder Alloy, Cold-sprayed Coating	Biodur 108 alloy (Carpenter technologies)
FMC-AS	Powder Alloy, Cold-sprayed Coating	Fe-Mn-Cr candidate un-treated (As received from the supplier)
FMC-N	Powder Alloy, Cold-sprayed Coating	Fe-Mn-Cr-N alloy with desired Nitrogen content
FMC-Ar	Powder Alloy, Cold-sprayed Coating	Fe-Mn-Cr-AS alloy treated with Argon only
FMC-N-Ar	Powder Alloy, Cold-sprayed Coating	Fe-Mn-Cr-N alloy with desired Nitrogen content retreated with Argon
FMN-AS	Powder Alloy, Cold-sprayed Coating	Centrifugally atomized Fe-Mn-Cr-N alloy with desired Nitrogen content
FMN-AS	Powder Alloy, Cold-sprayed Coating	Centrifugally atomized Fe-Mn-Cr-N alloy with desired Nitrogen content
GA 316	Powder Alloy, Cold-sprayed Coating	Gas atomized SS316 alloy alloy
CA 316	Powder Alloy, Cold-sprayed Coating	Gas atomized SS316 alloy alloy

*** Treatments and sample details are mentioned in the respective experiment section*

Table 3-3 Example Sample IDs Used for Data-Model Using Experimental Approach

Sample ID	**Parameters**				
#	**Main Gas pressure (psi)**	**Feed (mm/s)**	**Powder Feed (g/min)**	**Powder Preheat (°C)**	**Standoff (mm)**
1	500	10	150	600	10
1.1	500	10	150	600	10
2	500	10	300	600	10
2.1	500	10	300	600	10
3	500	30	150	600	10
3.1	500	30	150	600	10
4	500	30	300	600	10
4.1	500	30	300	600	10
5	500	10	150	600	30
5.1	500	10	150	600	30
6	500	10	300	600	30
6.1	500	10	300	600	30
7	500	30	150	600	30
7.1	500	30	150	600	30
8	500	30	300	600	30
8.1	500	30	300	600	30
9	500	10	300	225	10
9.1	500	10	300	225	10
10	500	10	150	225	10
10.1	500	10	150	225	10
11	500	30	150	225	10
11.1	500	30	150	225	10
12	500	30	300	225	10
12.1	500	30	300	225	10
13	500	10	150	225	30
13.1	500	10	150	225	30
14	500	10	300	225	30
14.1	500	10	300	225	30
15	500	30	150	225	30
15.1	500	30	150	225	30
16	500	30	300	225	30
16.1	500	30	300	225	30
17	360	10	150	600	10
17.1	360	10	150	600	10
18	360	10	300	600	10
18.1	360	10	300	600	10
….	…..	…..	…..	…..	……

Chapter 4 Functional HNS Coatings With Rapid Solidification (Path A)

Few members from the additive manufacturing group at the U-M Dearborn actively participated in investigating the nitrogen dissolution by a rapid-solidification route using Direct metal Deposition. This chapter elaborates a few results and findings from the study. The outcome of this investigation was further used to explore the solid-state dissolution route (Path B).

4.1 Composition Formulation

An in-house treatment was set-up to treat pure manganese powders in the presence of nitrogen to for manganese nitrides (Mn_xN_y). Two iterations of powder treatments with different treatment temperatures and times were conducted. Table 4-1 shows the LECO measurements on the Mn_xN_y powders. In-order to understand the phases of Mn_xN_y, an X-ray diffraction as well as Rietveld refinement was carried out as shown in Fig 4.1 and Table 4-2.

Table 4-1 LECO Analysis Measurements on Treated Mn Powders

Treatment Type	**N (% wt.)**
N1	8.09%
N2	8.08%

The Mn-N system has typical 4 phases as a combination of Mn and N together (Mn_xN_y). The FCC ε-phase, called Mn_4N (Mn 94.01 wt. %; N 5.99 wt. %; space group: Pm¯3¯m cubic); and face centered tetragonal η-phase named as Mn_3N_2 (Mn 85.47 wt. % N14.53 wt. %; space group: I4/mmm tetragonal) are the phases of interest considered in this study for the treatment temperature range. The Close packed hexagonal ζ-manganese nitride-$Mn_6N_{2.58}$ (Mn 90.12 wt. % N9.88 wt. %;

space group: P6322 hexagonal) along with its orthorhombic polymorph $MnN_{0.43}$ is also considered [43]. The crystallographic information of this polymorph has been used for further analysis. $Mn_6N_{2.58}$ is most recurring at this temperature range of 850°-1000°C [44, 45]. Formation of Mn_4N and Mn_3N_2 is also favorable [46, 47]. The peaks for the treated powders were indexed using ICDD 2019 database. Mn_3N_2 –PDF #04-011-7277; $Mn_6N_{2.58}$ –PDF #00-031-0824/#04-007-2198; Mn4N –PDF #00-01-1202 [38] were used. The Pure manganese powder matched with the PDF #00-032-0637 (space group I¯4¯3m) [38]. These diffraction peaks are also in accordance with those reported by few researchers [44, 45]. A minor phase shift of 0.1-0.2° was observed. This could be possible due to a non-equilibrium process as well as the instrument error. Previous research shows that in pure nitrogen stream only Mn_4N can be synthesized in pure form at higher temperatures [47]. In this study using a $90\%N_2/10\%H_2$ stream stable phases of Mn_3N_2; Mn_4N and $Mn_6N_{2.58}$ were achieved in different proportions.

Table 4-3 shows the starting compositions used to prepare functional coatings by rapid solidification. Composition 1 and Composition 3 contained the pretreated manganese powders N1 and N2 respectively. A standard AlN (Al-501) powder (Al-65.8 wt. %; N_2- 34.2 wt. %) procured from Atlantic Equipment Engineers (AEE) was included in composition 2 and 3. These nitrides present in the composition were responsible for the nitrogen content in the prepared coatings.

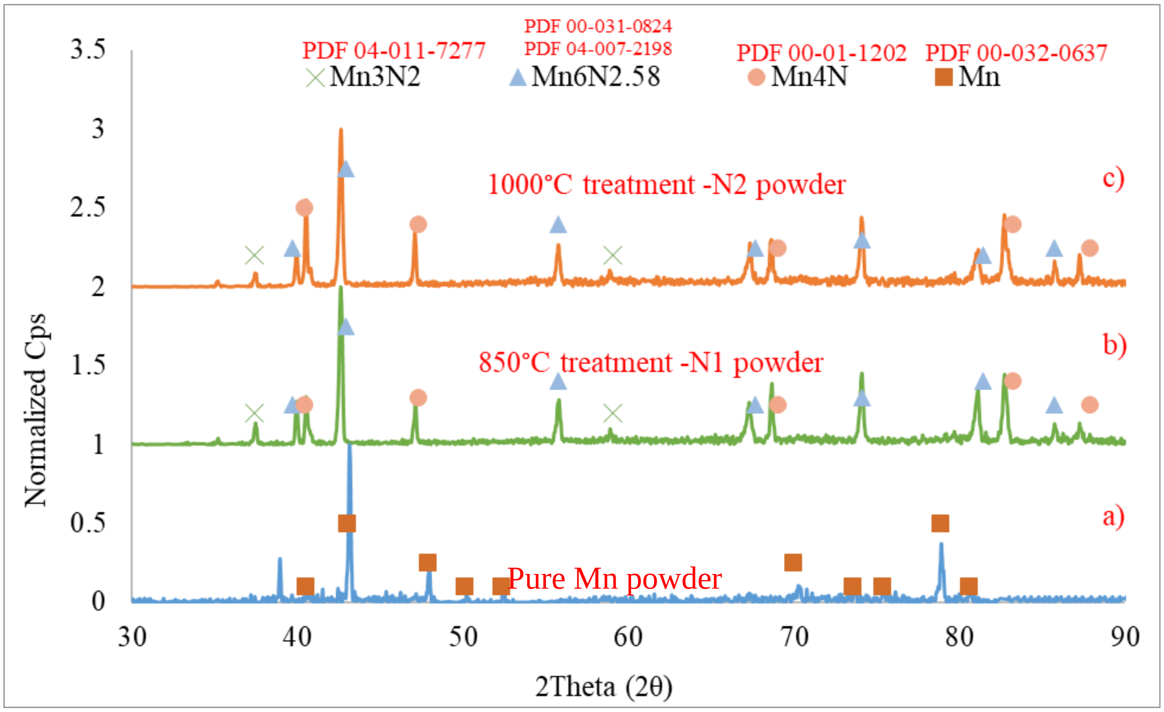

Fig 4.1 Diffraction Patterns for Treated Powders N1 and N2 Benchmarked With Pure Mn Pattern

Table 4-2 Rietveld Analysis Quantification

	$Mn_6N_{2.58}$/$MnN_{0.43}$	**Mn_4N**	**Mn_3N_2**
N1 powder	76.09 ± 2.74%	22.76 ± 0%	1.1407 ± 0.2%
N2 powder	68.238 ± 1.36%	29.45 ± 0%	2.304 ± 0.418%

Table 4-3 Compositions With Mn_xN_y and AlN Mix

	Al (%wt.)	**Mn (%wt.)**	**Cr (%wt.)**	**C (%wt.)**	**MnN (%wt.)**	**AlN (%wt.)**	**Fe (%wt.)**
Composition 1 (C1) (with N1 powder)	6	-	10	0.1	22	-	Bal.
Composition 2 (C2)	-	22	10	0.1	-	6	Bal.
Composition 3 (C3) (with N2 powder)	-	-	10	0.1	22	6	Bal.

4.2 Functional Coatings Using DMD

Since preformed nitrides were used in the composition; it was necessary to dissolve these nitrides and retain nitrogen in the composition. This was possible by using a rapid-solidification technique to produce functional coatings. DMD technique is widely known for its rapid solidification ability after melting. In-order to analyze this alloy for its mechanical properties, coatings were prepared using laser cladding with the DMD (Direct metal deposition) technique.

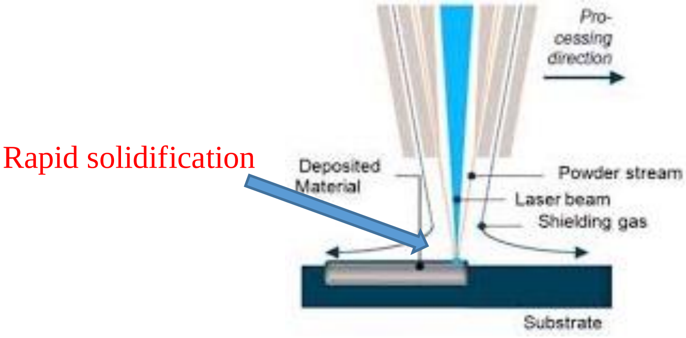

Fig 4.2 Schematic of a DMD Process

A DMD-105D equipment from POM Inc. was used to manufacture coatings on stainless steel substrates [48]. Depositions were done in-order to achieve a ~1.5mm thick coating. The scan speed, input current was derived after a few trial runs.

4.3 Analysis of DMD Coatings

The prepared coatings were further analyzed for their performance in-order to finalize a required composition for the final concept.

4.3.1 Nitrogen Content

Table 4-4 represents the retained nitrogen content in the clad materials. Composition C1 had a mean retained nitrogen of ~0.28 wt. %. The nitrogen content varied from 0.03% to 0.39% in the C1 coating. This non homogeneity of nitrogen content could be a result of hand-mixed composition as well as lack of nitrogen content to stabilize austenite. The Nitrogen content being non uniform and low wasn't enough for a complete austenite transformation. Similarly, for Composition C2 this nitrogen content being ~0.3% with a lower variance; would indicate a presence of Austenite. However, the achieved nitrogen in Composition C3 was high enough to retain austenite. This was further supplemented with XRD pattern. Compositions C2 and C3 would be the samples of interest for a better corrosion and wear resistance.

Table 4-4 LECO Measurements for N Retained in Clad Materials (Average of 4 Readings at Different Locations)

Sample	**Avg. N (% wt.)**
Composition C1	0.287±0.17
Composition C2	0.32±0.04
Composition C3	0.58±0.03

The nitrogen measurement on C1 coating noticeably had a high standard deviation implying a non-homogenous distribution of nitrogen content all over the coating. A desired nitrogen content with a minimized variance was achieved for compositions C2 and C3.

4.3.2 Microstructural Characterization

Fig 4.3 and Fig 4.4 show the basic characterization performed on the coatings. The cross-section images are separated by a red- dotted line to easily distinguish the stainless-steel substrate and the coating. Pure austenitic microstructure was achieved in the coating C3 with a residual ferrite content in C2. Coating C1 was primarily in ferrite phase which further explains its non-homogenous presence of nitrogen over the cross-section with a high variance. Coating C3 thus proved to be a coating of interest given that it had the desired FCC phase which improved the solid solubility of nitrogen.

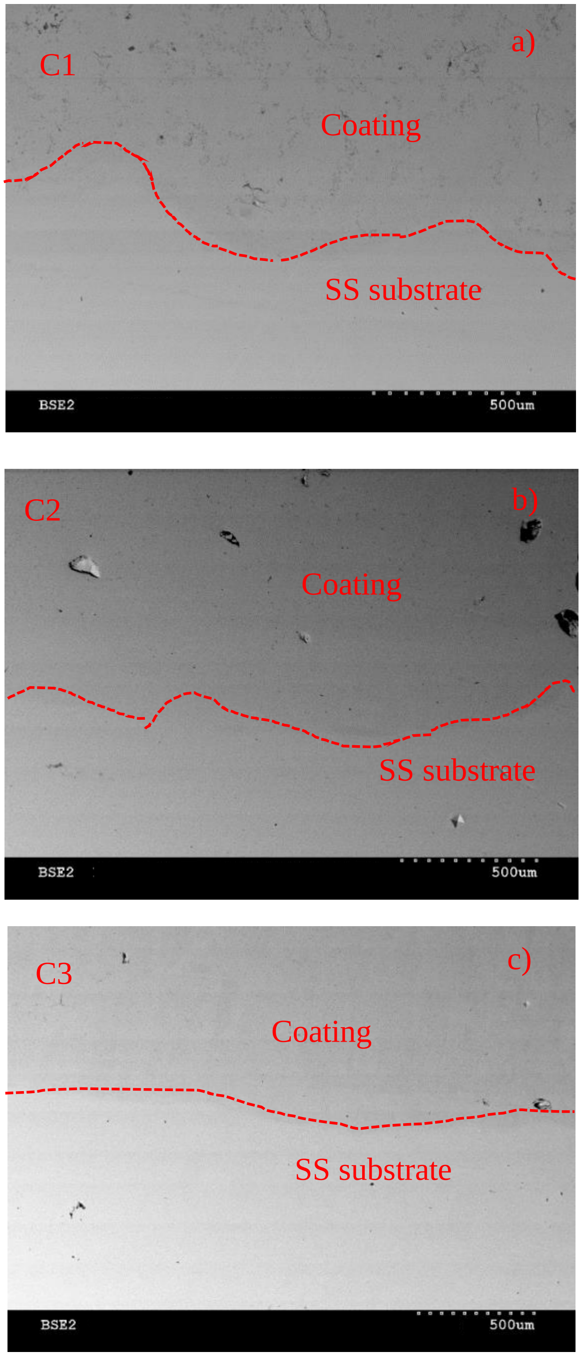

Fig 4.3 Unetched Cross-Sections of Deposited Coatings a) C1, b) C2, c) C3

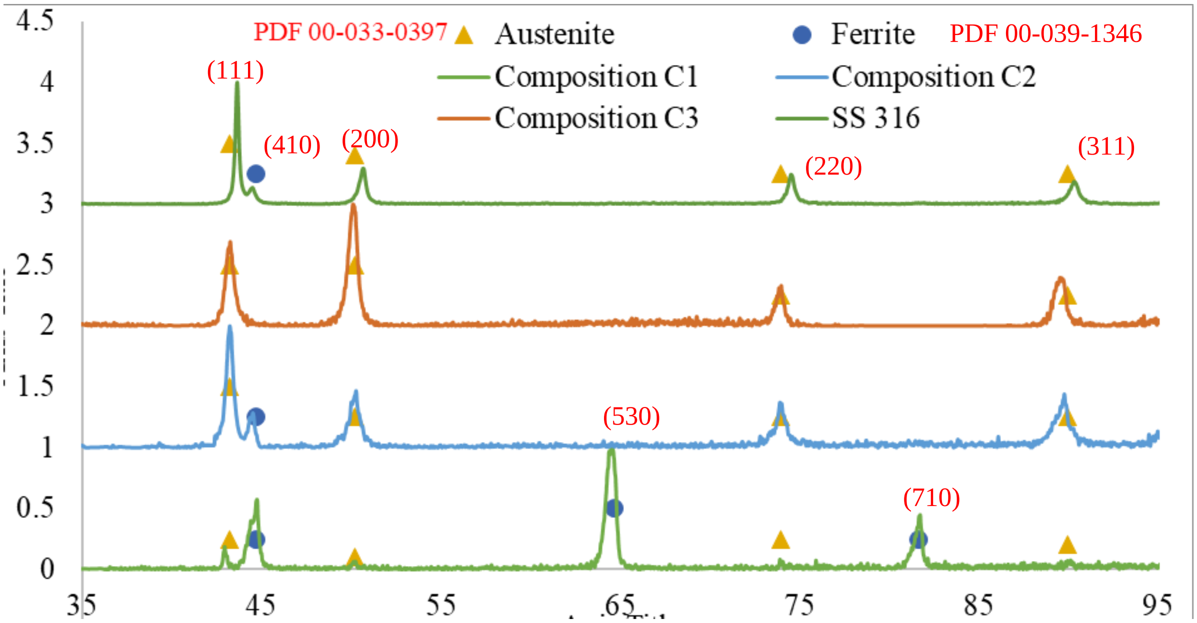

Fig 4.4 XRD Patterns for DMD Coatings

4.3.3 Micro-Hardness

Fig 4.5 represents a variation of micro-hardness along different positions with respect to the bond line of the clad coatings. A consistent softer micro-hardness of ~170$HV_{0.3}$ was measured on the SS substrate. A softer bond-line was observed for all the clad coatings. The hardness progressively increased towards a constant value away from the bond-line. Composition C3 was observed to have the highest hardness value of ~345$HV_{0.3}$. Composition C2 also relatively had more hardness of ~315$HV_{0.3}$. The hardness values could correlate with the nitrogen content and validate the point of a stronger material with Nitrogen in Austenite phase of the alloy.

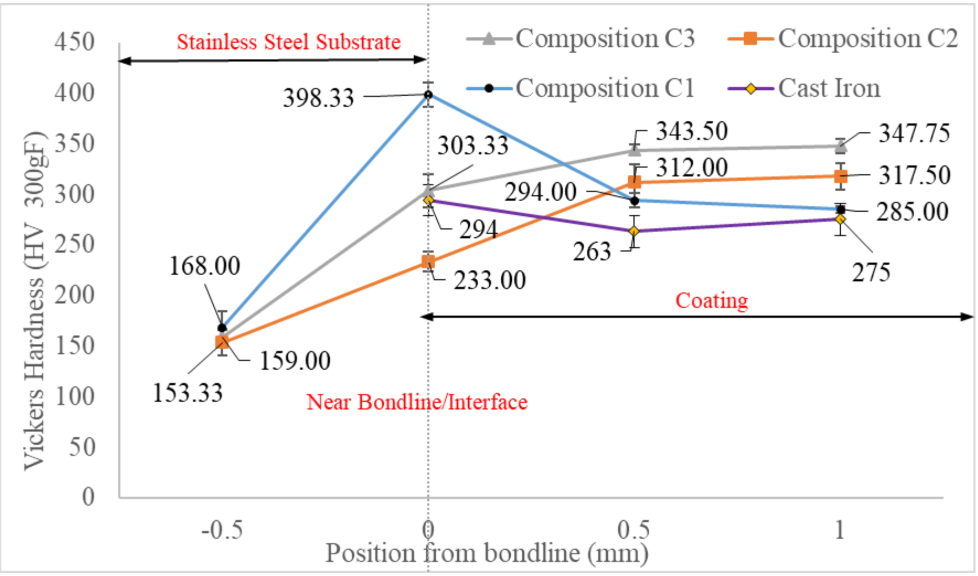

Fig 4.5 Micro-Hardness Profile of Clad Coatings Benchmarked with Cast Iron and SS Substrate

4.3.4 Corrosion Properties

The corrosion behavior of the coatings was measured by the electrochemical/galvanic technique. An Ag/AgCl and Pt wire were used as reference and counter electrode respectively in a 0.5% NaCl solution used as an electrolyte. Two tests were conducted at room temperature (~25degC) to measure the Open circuit potential (OCP) and the polarization behavior (potentio-dynamic curve). The collected data was analyzed for Tafel-fitting using commercially available software (EC-lab). Fig 4.6 represents a potentio-dynamic curve for the prepared coatings benchmarked with a standard SS316 and a Cast iron specimen. The prepared coatings had a corrosion potential essentially between the referenced samples.

A recommended nitrogen content of 0.15-0.3% has been proven to improve the corrosion resistance of steel alloys [49]. Passivation of transition was observed for the prepared coatings compared to the reference samples.

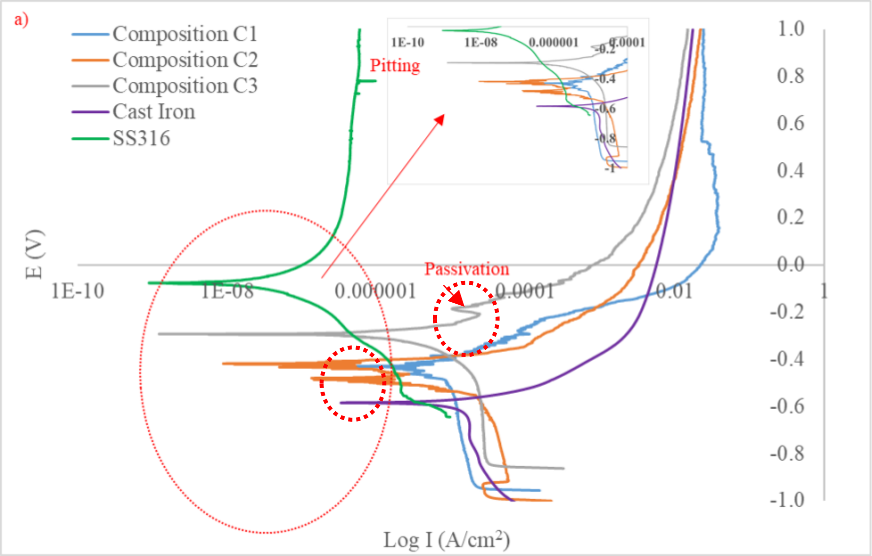

Fig 4.6 Potentio-Dynamic Curves of Clad Materials (Ref. Cast Iron and Aluminum)

Table 4-5 Corrosion Potential and Tafel Slopes for DMD Coatings

Sample	**Ecorr (mV)**	**Icorr (µA/cm2)**	**ßa**	**ßc**
Composition C1	-430.305±7.72	8.94±0.81	152.733±4.99	1692±89.8
Composition C2	-442.765±2.79	6.699±0.94	43.6±2.80	104±76.38
Composition C3	-290.708±5.42	1.783±0.08	103.36±46.75	230.23±51.85
Cast Iron	-606.467±19.64	13.477±1.67	98.86±23.34	749.5±68.01
Stainless Steel 316	-76.495±3.56	0.044±0.02	224.1±91.32	181.2±68.56

4.4 Summary and Conclusions

Functional coatings with High nitrogen content were successfully produced using a rapid solidification technique. A nitrogen content of 0.3 wt.% - 0.4 wt. % was thus sufficient to provide a functional coating with high mechanical and corrosion performance. Thus, this study helped formulate a desired composition to provide optimized mechanical properties and corrosion resistance of the alloy.

However, a rapid solidification technique which involves molten state of the alloy, has a lower solubility limit of nitrogen compared to that in a solid-state form [5, 21]. Process control and quality control are very critical to be maintained for the precise nitrogen concentration. The scalability of this process is thus a challenge because of following factors:

1. Homogeneity of nitrogen along the cross-section:

   During this investigation, a varied nitrogen content at different positions over the cross-section of deposited samples was observed. This further needs to be optimized in-order to homogenize the nitrogen content all over the coating.

2. Process control for quality assurance:

   Due to lack of homogeneity, a precise process control would be essentially required to improve the quality assurance of the process.

3. Uniform cooling rate:

   During rapid solidification, maintaining a uniform thermal history would be very critical in-order to maintain the microstructure and avoid precipitation. Although this technique involves rapid solidification, the cooling rates at every point on the depositions would depend on the process parameters

4. Cost feasibility:

   The economics of a rapid solidification technique depends on multiple parameters viz. Laser apparatus and the power used, equipment parameters, and the general infrastructure of the process, which put it up on a higher note. This thus limits the commercialization of this process to manufacture protective functional coatings.

Chapter 5 Solid-State Precursor Development (Path B)

Single Stage/Double stage treatment of Fe-Mn-Cr powder

Paper 1: A novel high nitrogen steel powder designed for minimized Cr_2N precipitations

This article summarizes a solid-state dissolution treatment of an Fe-Mn-Cr precursor with an optimized thermal history as displayed in Fig 2.3 in-order to avoid precipitation in the powder simultaneously preventing sintering. This method will thus increase the usability of the alloy in multiple manufacturing methods (preferably solid-state) simultaneously providing high corrosion resistance and excellent mechanical properties.

The approach of rapid solidification as discussed in Chapter 4 has a few limitations in terms of quality assurance and homogeneity of the nitrogen content all over the deposited coating. Despite the elimination of the δ-ferrite region; rapid solidification involves a precise process-control. A solid-state diffusion followed by rapid cooling is thereby another route to manufacture the steel since the nitrogen solubility limit is higher in solid-state [21, 5, 19]. Replacing/minimizing the precipitates by retaining more amount of nitrogen interstitially dissolved in the expanded γ matrix (S-phase), can provide an optimized alloy strength simultaneously improving the corrosion resistance [29, 18].

5.1 Alloy Composition

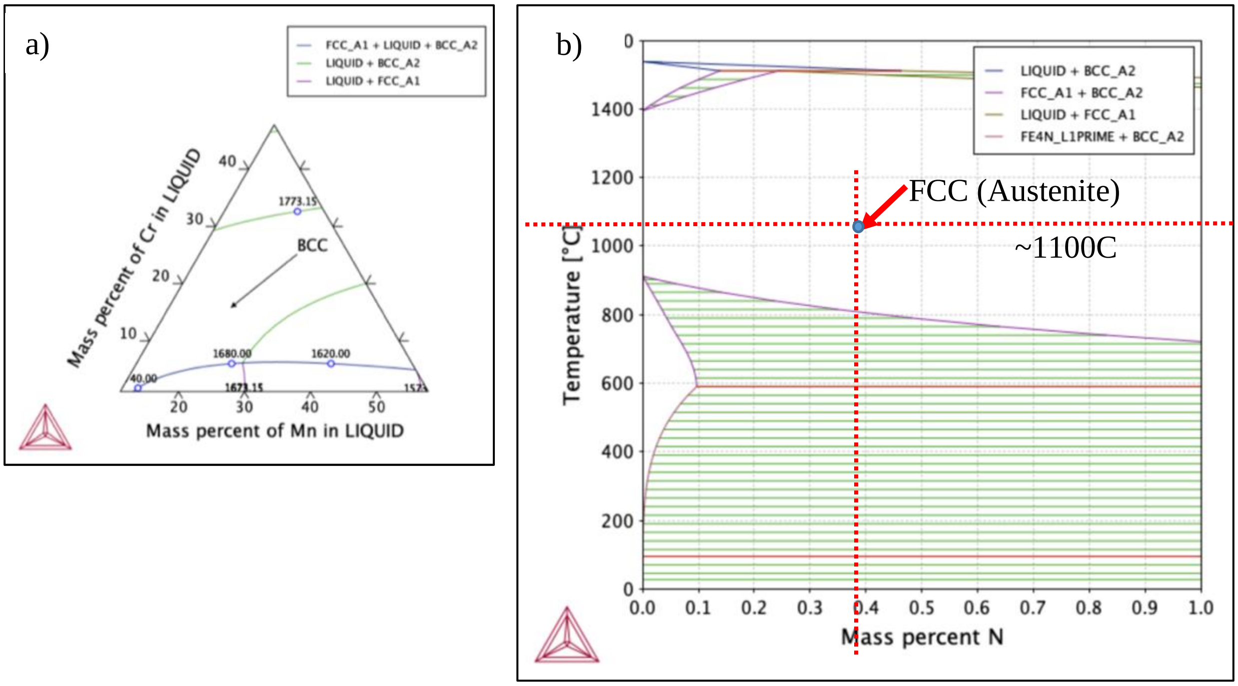

Fig 5.1 Single Point Equilibrium Phase Diagrams for a) Fe-Mn-Cr b) Fe-N Systems

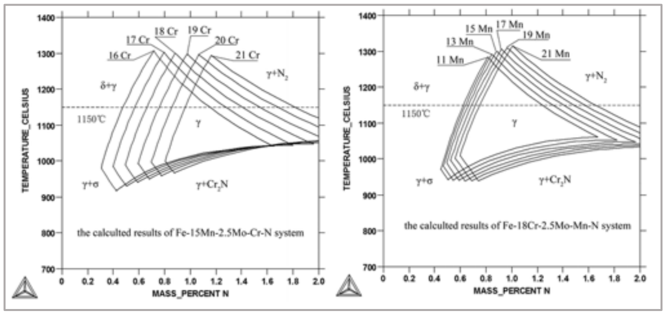

Fig 5.2 Effect of Cr and Mn Contents on Stable γ Phase [6]

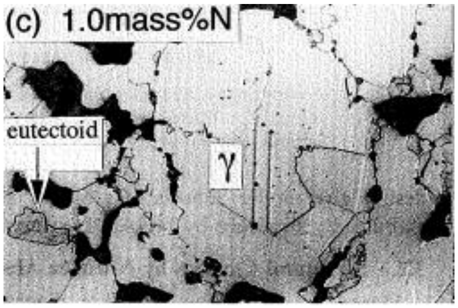

Fig 5.3 Nitride Precipitation Due to Air Cooling

[36]

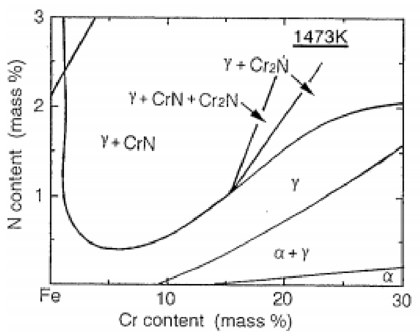

Fig 5.4 Effect of Cr&N Content on Stable Phases in HNS Alloys [36]

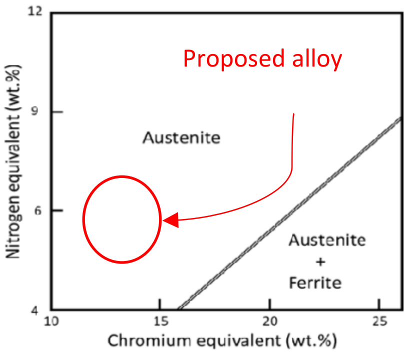

Fig 5.5 Resultant Alloy Phase for Nitrogen and Chromium Equivalent [6]

Alloying elements like Mn,Cr,V,Nb can be included to improve the nitrogen solubility; whereas elements like C,Si,Ti are known to promote nitride formation [18, 19].

With a few experimental data points an empirical equation has been reported for Nitrogen and Chrome equivalent in HNS. This equation aids in determining the right composition with respected to the desired phase in equilibrium.

Fig 5.5 displays a Schaeffler diagram [6, 3] for Nitrogen equivalent and chrome equivalent to predict the final phase.

Equation 5-1 Nitrogen Equivalent

$N\_eq = 10\,(\text{wt. \% N}) + 0.25\,(\text{wt. \% Mn}) - 0.02(\text{wt. \% Mn})^{2} + 0.00035(\text{wt. \% Mn})^{3}$ [6]

&

Equation 5-2 Chromium Equivalent

$Cr\_eq = \text{wt. \% Cr}$ [6]. Thus, based on findings from Chapter 4 , the compositions were finalized using Equation 5-1and Equation 5-2.

Table 5-1 Base Composition of the Proposed Alloy by Atomization (FMC-AS)

Elements	**Cr**	**Mn**	**Al+Si+C+Mo+impurities**	**Fe**	**N_2**
Composition (% wt.)	14-15%	22-24%	1-2%	Bal.	~0.01-0.05%

Table 5-2 Proposed Composition of the Alloy After Solution Treatment (FMC-N)

Elements	**Cr**	**Mn**	**Al+Si+C+Mo+impurities**	**Fe**	**N_2**
Composition (% wt.)	14-15%	22-24%	1-2%	Bal.	**0.3-0.5%**

With the base compositions mentioned in Table 5-1 a centrifugally atomized alloy was procured from Erwin Industries, Tecumseh, MI [50]. Fig 5.6represents the analysis results as received from the supplier with the desired composition.

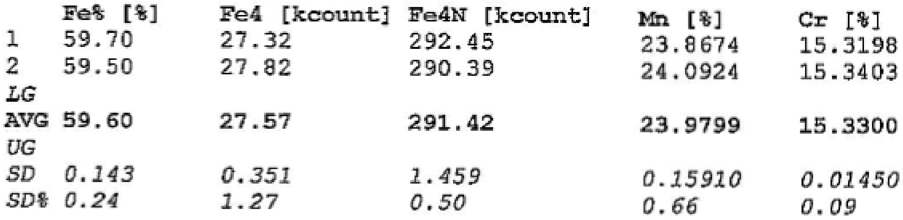

```
     Fe% [%]    Fe4 [kcount] Fe4N [kcount]   Mn [%]     Cr [%]
1    59.70      27.32        292.45          23.8674    15.3198
2    59.50      27.82        290.39          24.0924    15.3403
LG
AVG  59.60      27.57        291.42          23.9799    15.3300
UG
SD   0.143      0.351        1.459           0.15910    0.01450
SD%  0.24       1.27         0.50            0.66       0.09
```

Fig 5.6 Chemical Analysis Results as Received From the Supplier (FMC-AS)

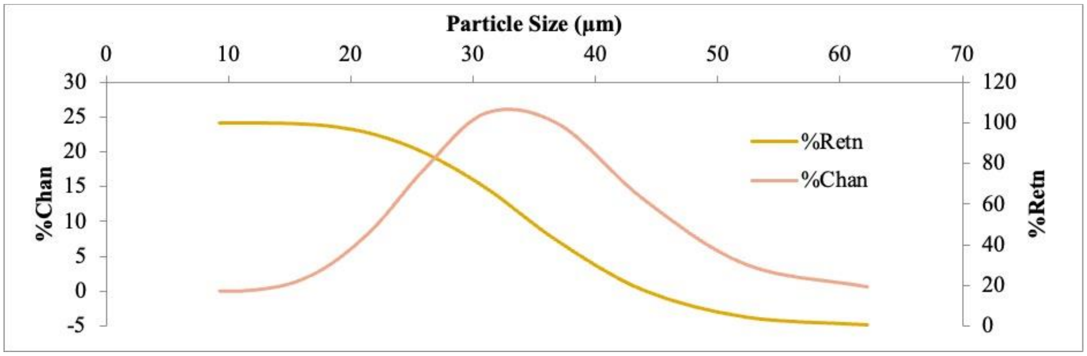

Fig 5.7 Particle Size Distribution for the FMC-AS Powder

5.2 Initial Characterization

Fig 5.8 shows a cross-section of the powder alloy. The procured powder had a pure ferritic matrix as seen in Fig 5.9. Fig 5.10 and Fig 5.11 show the EBSD measurements on the powder cross-section.

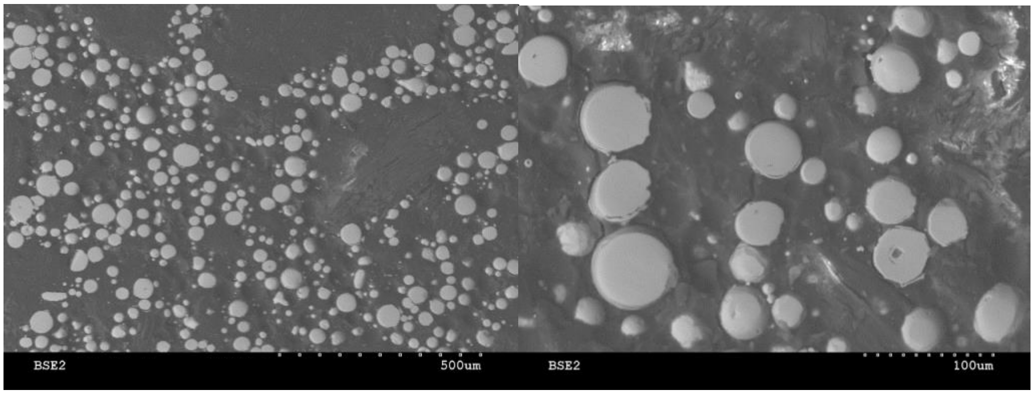

Fig 5.8 FMC-AS Alloy Powder Cross-Section

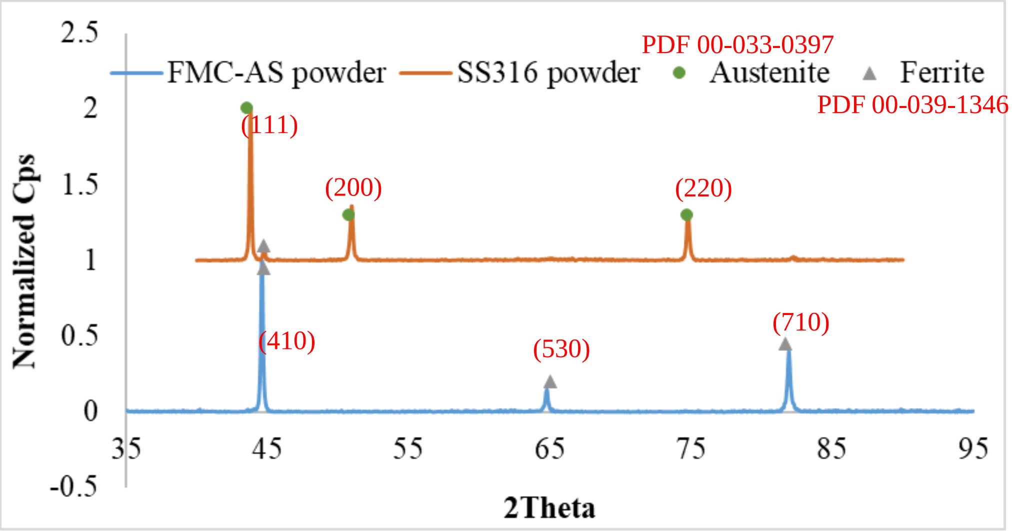

Fig 5.9 XRD Pattern for As-Received FMC-AS Alloy

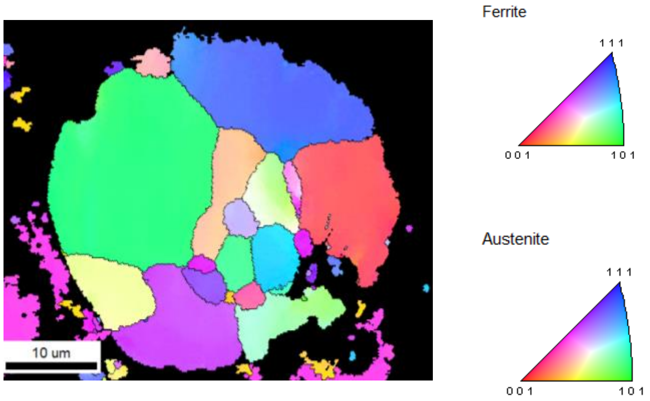

Fig 5.10 IPF Map of FMC-AS Powder

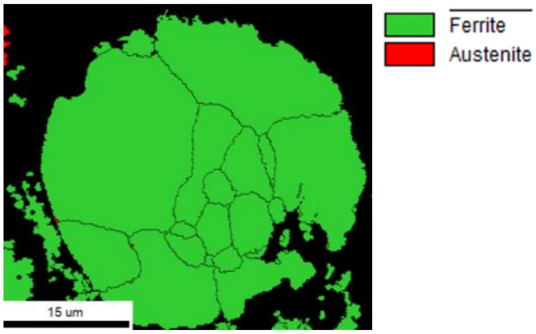

Fig 5.11 Phase Map of FMC-AS Powder

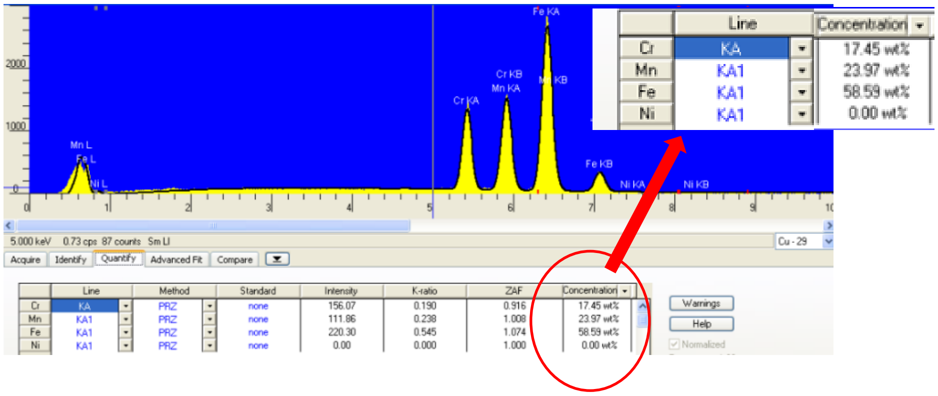

5.000 keV 0.73 cps 87 counts Sm LI

	Line	Method	Standard	Intensity	K-ratio	ZAF	Concentration
Cr	KA	PRZ	none	156.07	0.190	0.916	17.45 wt%
Mn	KA1	PRZ	none	111.86	0.238	1.008	23.97 wt%
Fe	KA1	PRZ	none	220.30	0.545	1.074	58.59 wt%
Ni	KA1	PRZ	none	0.00	0.000	1.000	0.00 wt%

Fig 5.12 EDS Spectra With Elemental Maps for FMC-AS Alloy

5.3 Background Work

A transient-thermal simulation model using Ansys Workbench (Mechanical) was set-up to achieve optimum parameters for a dwell time. These simulations were performed in-order to get a baseline reference to achieve the austenizing temperature as quickly possible in the heat zone, allowing enough time for the Nitrogen uptake. The powder mass was assumed as a lumped mass for the simulation with the alloy material properties. This simulation model assumes the convection properties of inert media i.e N_2. Thus, a greater hatched region is favorable for more dwell time at higher temperature i.e 120W/m^2K with a 10g lumped mass. Similarly for cooling, a faster cooling rate is essentially desired to bypass the Cr_2N formation region which is ~600°-900°C [3, 22, 24].

Fig 5.13 shows a heat flow behavior of the FMC-AS alloy. A change from an exothermic flow to endothermic flow was observed around ~653°C. This possibly could be an indicator towards α→γ transition.

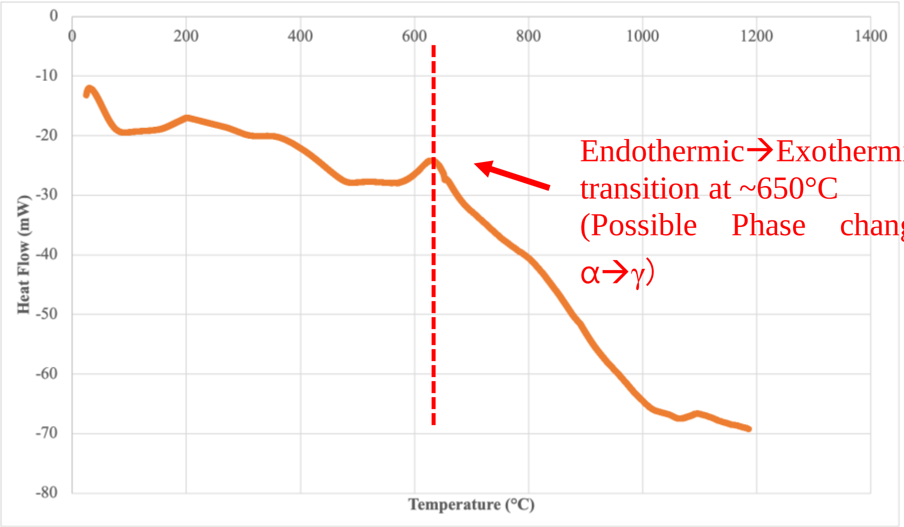

Fig 5.13 Dsc Plot for As-Received Candidate Alloy

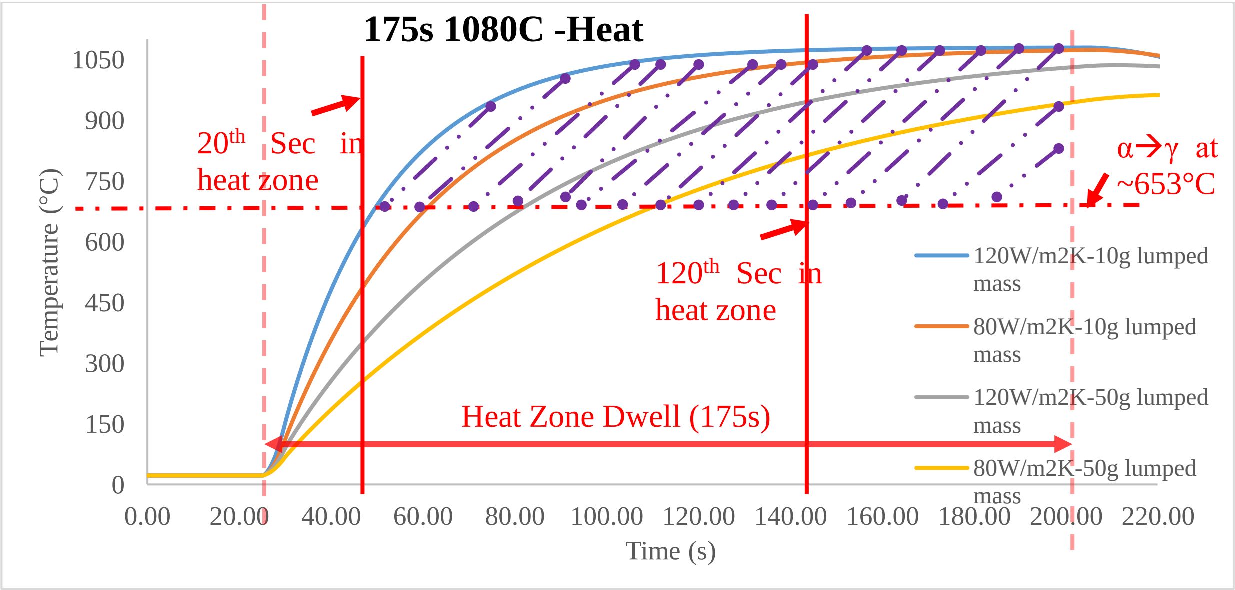

Fig 5.14 Temperature vs Time Curves at Various Film Coefficients -Heating

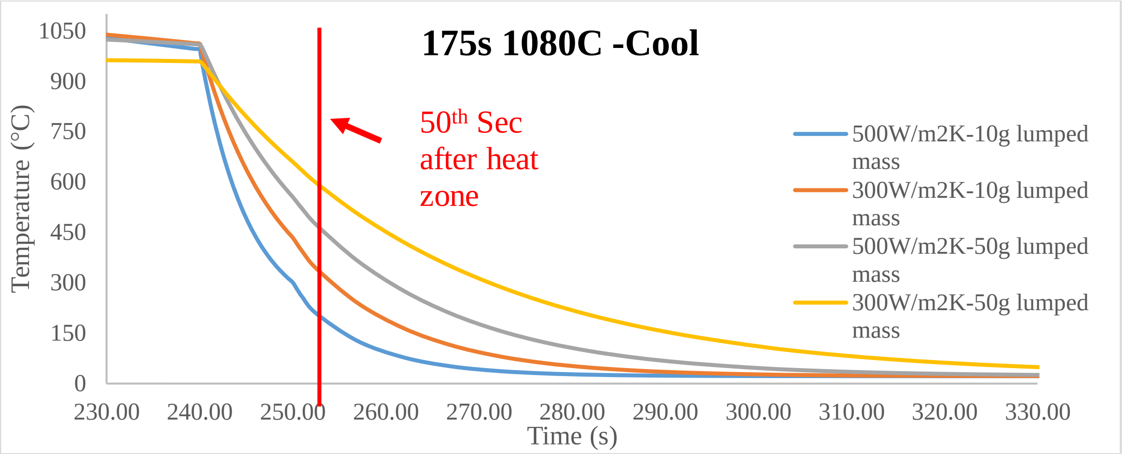

Fig 5.15 Temperature vs Time Curves at Various Film Coefficients -Cooling

** Data points were recorded at steps of 5s

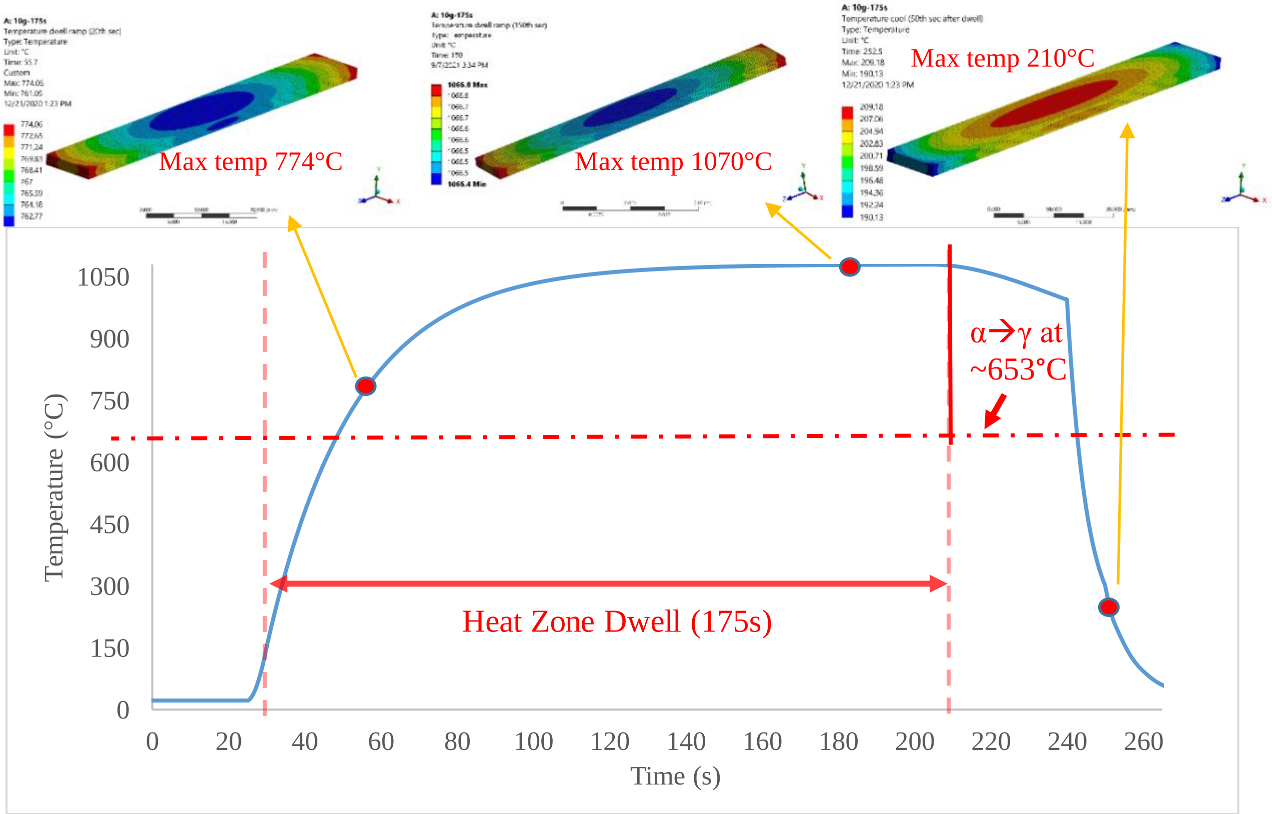

Fig 5.16 Heating Curve for 175s Dwell Time (10g Lumped Mass)

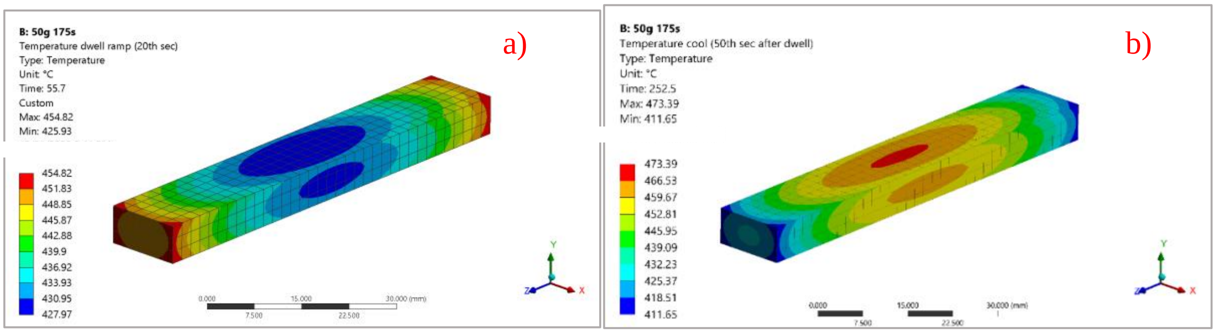

Fig 5.17 Temperature Contour for 50g Lumped Mass - Temperature Snippet at a) 20th Sec in the Heat Zone; b) 50th Sec After Heat Zone(cool)

Using the film coefficients optimized from the simulation; temperatures curves were plotted for various dwell times in the heat zone. It was thus evident from that a 100s dwell time was not enough for the lumped mass to achieve 1080°C and dwell for enough nitrogen intake.

5.4 Powder Treatment (System Design)

A stagnant treatment style was chosen for the powder treatment. The idea of treatment was adopted from a push-pull furnace mechanism. Fig 5.18 represents a schematic of the design powder-treatment setup.

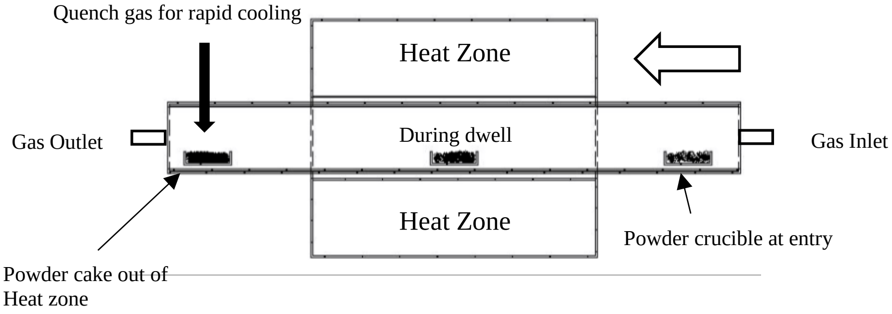

Fig 5.18 Powder Treatment Schematic

Fig 5.19 represents a sample nitride precipitation appearing as black spots on one of the initial treatments done on the FMC-AS powder with a dwell time of 10 minutes at 1080°C. More precipitation was observed with higher dwell times proving the fact that the nitrogen content was reaching beyond its solubility limit. The treatment times were thus optimized for desired nitrogen content without such precipitation.

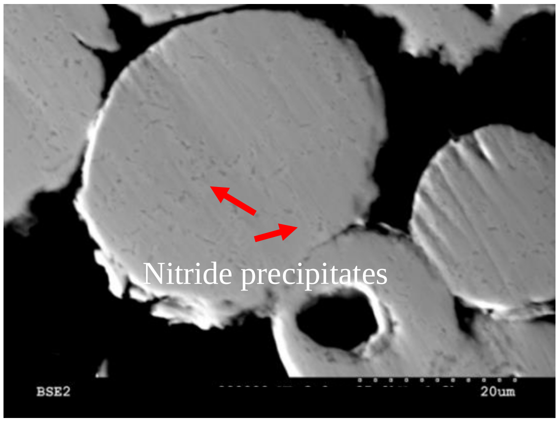

Fig 5.19 Nitride Precipitates in FMC-N Alloy (10min Treatment at 1080°C)

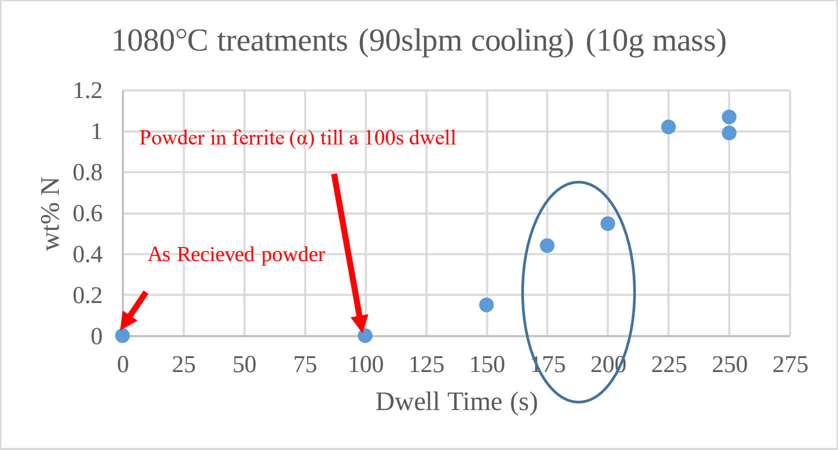

Fig 5.20 Nitrogen Content With Different Dwell Times at 1080°C for FMC-AS Single Stage Treatment

Fig 5.20 represents a variation spectrum of LECO measurements obtained at different dwell times for 1080°C treatments. With the required Nitrogen contents (i.e., 0.3-0.5 wt. %) an optimum dwell time of 175s was thus selected. The above spectrum presents an average reading of 4 experiments at each dwell times. The simulation results from Fig 5.17 were thus validated with a fact that a 100s dwell time is not enough for the nitrogen uptake compared to 175s dwell in the heat zone. A near-linear trend was observed with the nitrogen uptake for dwell time beyond 125seconds at 1080°C treatment temperature.

Table 5-3 Crystal Information for Phases Used for EBSD Indexing [34]

Samples	**Temperature (K)**	**Dwell time (s)**	**Purge gas**
FMC-Ar	1353	175	Ar/H_2 only
FMC-N	1353	175	N_2/H_2 only
FMC-N-Ar-175 (*retreat FMC-N)	1353	175	Step1) N_2/H_2 only
	1353	175	Step2) Ar/H_2 only

5.5 Powder Characterization and Analysis

With the parameters mentioned in Sec 5.4 a lot of powder was prepared with a 10g powder treated per experiment.

5.5.1 Nitrogen Content

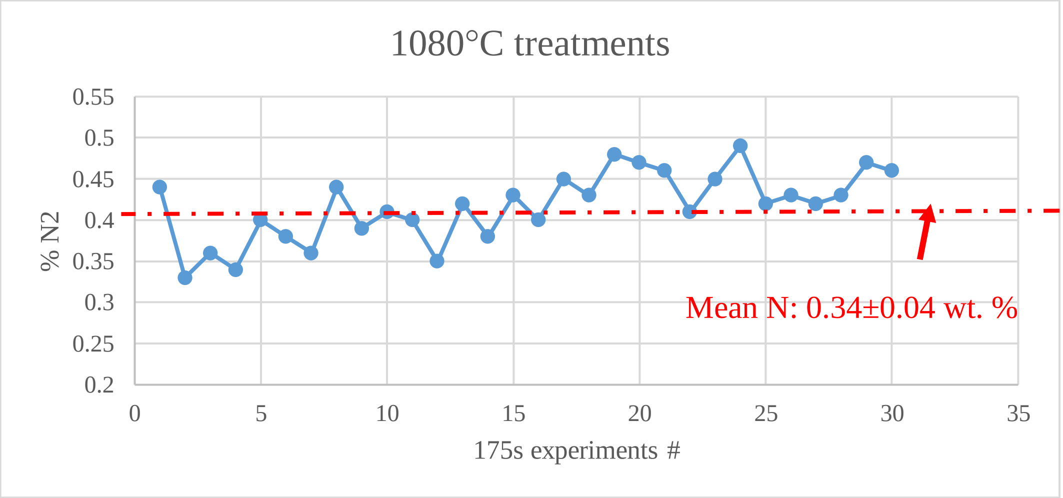

Fig 5.21 Nitrogen Content Achieved at 175s Dwell Time for Single Stage Treatment.

Fig 5.21 shows a batch-wise variation achieved for every 10g treatment using the single-stage (nitrogen). An average nitrogen content of ~0.34% was achieved. These batches were then mixed and later used for deposition as well as retreatment (FMC-N-Ar 175/500s).

Table 5-4 shows a summary of LECO measurements for the treated powders. The FMC-AS and the argon treated alloy FMC-Ar measured a negligible nitrogen content ~0.05 wt. % corresponding to their inert atmospheres. It increased up to ~0.34 ± 0.05 wt% for the FMC-N treatment and was further improved after the 2-stage treatment in the FMC-N-Ar alloy measuring 0.38 ± 0.04 wt. %. This nitrogen content in FMC-N and FMC-N-Ar could correspond to the stabilized austenite which was verified by the XRD measurements. Nitrogen present in the γ-matrix of steels influences grain size and solid solution strengthening [51]. The treatment time and temperature ensured a minimal sintering and prevented densification of powders. This enabled an easy nitrogen uptake due to more surface area exposure [18].

Table 5-4 LECO Analysis Measurements on Powders

Powder samples	Nitrogen content (wt%.)
FMC-AS	0.05±0.01
FMC-Ar	0.05±0.01
FMC-N	0.34±0.05
FMC-N-Ar	0.38±0.04

5.5.2 EBSD Measurements

Indexing of phases was done using standard ICSD files imported in the analysis software [34, 32]. The microstructure of the treated powders is shown as IPF maps, phase maps and CI maps in Fig 5.22 through Fig 5.24. The presented scans show indexed particle portions only. Fig 5.25 shows a compiled distribution of the grain orientation spread of the treated powders. Fig 5.26 represents the grain size distribution for the powders. Fig 5.27 shows a mis-orientation angle distribution for the grain fraction of measured for the powders. Fig 5.28 presents image quality maps superimposed with grain rotation angle for the treated powders [Red (LAGB): 2°-15°; Blue (HAGB): ≥15°].

Partial grain refinement was observed in the single stage argon treatment (FMC-Ar) with a primary austenite(red) along with residual ferrite (green). However, the misorientation angles being predominantly under 15° entails relieving of internal residual stresses in the parent. Single stage nitrogen treatment led to the formation of a Cr-N short range order (yellow) and di-chromium nitride (white) precipitation along with a fine austenite microstructure (red). The precipitation was confirmed by a high-resolution scan on a small area as highlighted in Fig 5.22b. Cr_2N precipitation is associated with ferrite content typically in duplex steels. However, it has also been reported to occur in austenite(γ) in the as visible FMC-N powder [32]. Influence of nitrogen on refinement of grain boundary has been reported for solid ingots in previous studies [51, 52]. A similar behavior was observed in FMC-N powder particles. The fraction of higher angle grain boundary (HAGB) was higher for FMC-N powder which indicates grain boundary refinement and could be due to a combination of high lattice strain and precipitation of CrN/Cr_2Nphases.

The 2-stage annealing treatment (FMC-N-Ar) had a significant reduction in the HAGB fraction. According to Fig 5.28 a high density of sub-grain formation (red) was visible in the 2 stage particles indicating a relative low level of strains achieved compared to FMC-N. The grain boundary submicron-precipitates of Cr_2N as well as Cr-N diminished to a significant amount. Coarse grain sites were visible with a possible indicator towards grain growth relieving the stresses typically at the grain boundaries. The derived dwell time for the 2-stage treatment thus proved to be sufficient for minimizing the precipitates. Annealing of high nitrogen steels could also relieve high energy sites from precipitation [51, 30]. Intra-granular precipitates are not harmful towards reducing the toughness of HNS [51]. However, no such intra-granular sites were observed in the 2-stage treatment. All the grains had a confidence index of at least 0.1. This provides a support to the claim of growth of larger grains in the 2-stage treatment.

Table 5-5 Crystal Information for Phases Used for EBSD Indexing [34]

Phase	**a(Å)**	**b(Å)**	**c(Å)**	**α**	**β**	**γ**	**Crystal system**	**Space group**	**ICSD #**
CrN	2.97	4.12	2.88	90°	90°	90°	Cubic	PmmnS (59)	53146
Cr_2N	4.752	4.752	4.429	90°	90°	120°	Triclinic	Pm-3m (162)	67400
Austenite	3.66	3.66	3.66	90°	90°	90°	Cubic	Fm-3m (225)	631733
Ferrite	2.87	2.87	2.87	90°	90°	90°	Cubic	Im-3m (229)	180969

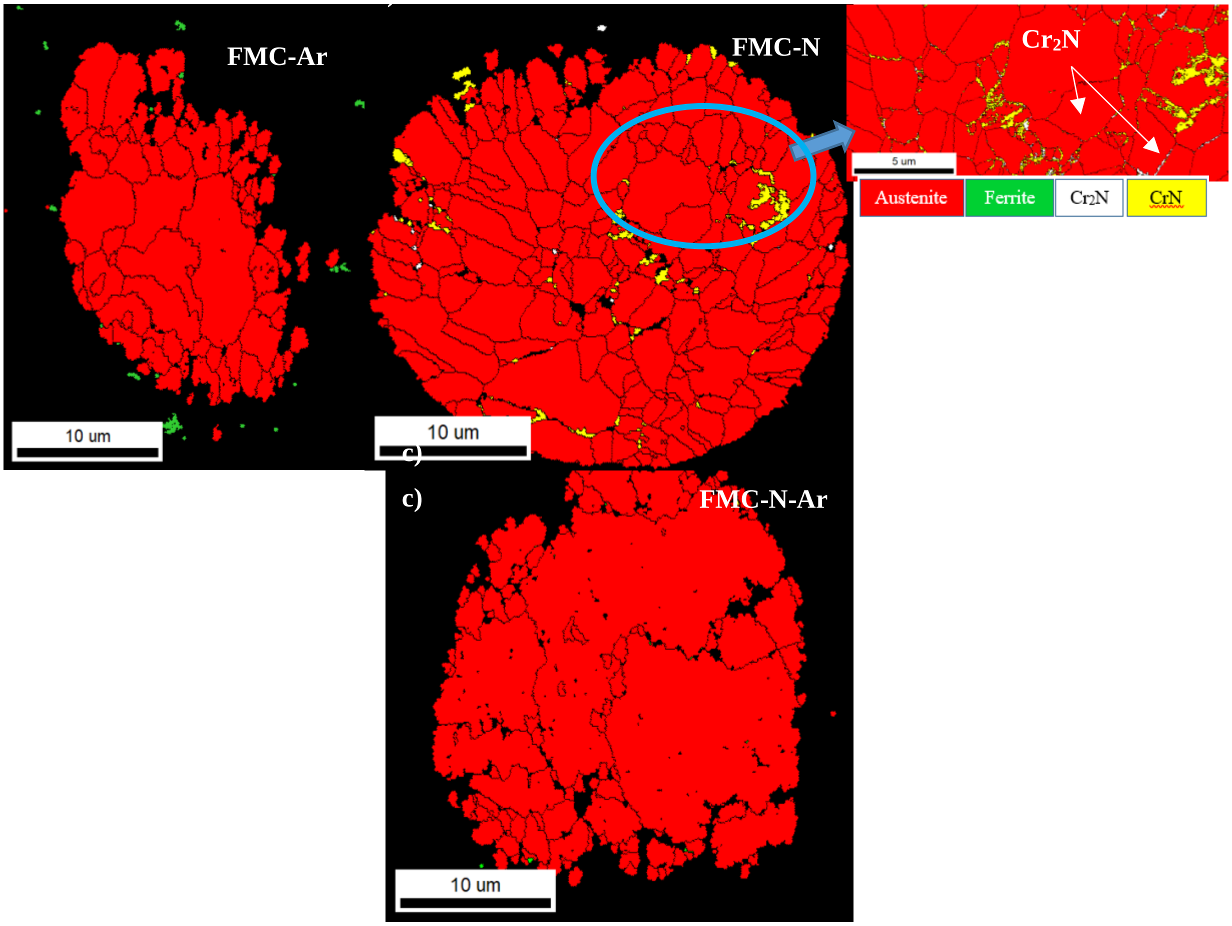

Fig 5.22 Compiled Phase Maps for Treated Powders a) FMC-Ar, b) FMC-N

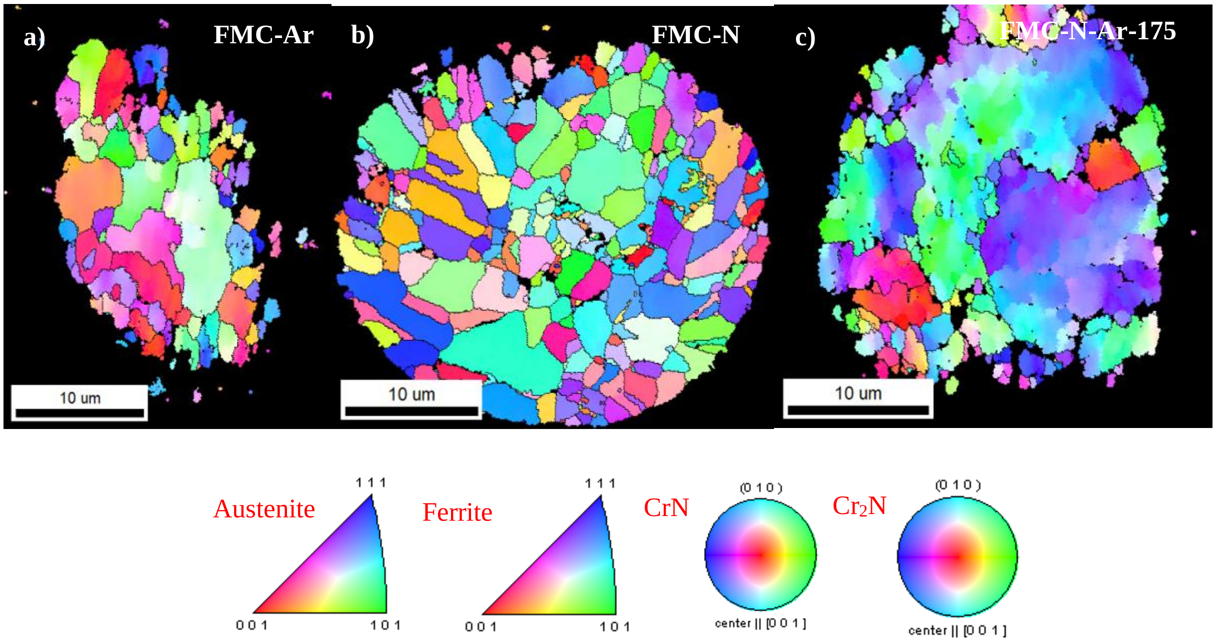

Fig 5.23 Compiled IPF Maps of Treated Powders a) FMC-Ar b) FMC-N c) FMC-N-Ar (175s)

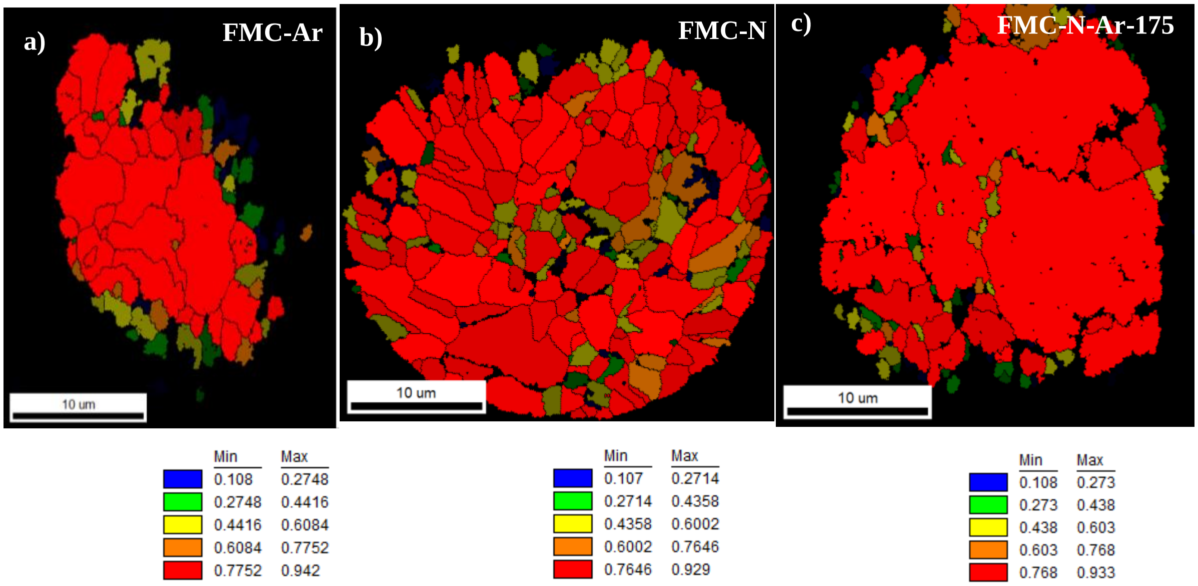

Fig 5.24 Compiled Confidence Index Maps of Treated Powders a) FMC-Ar b) FMC-N c) FMC-N-Ar (175s)

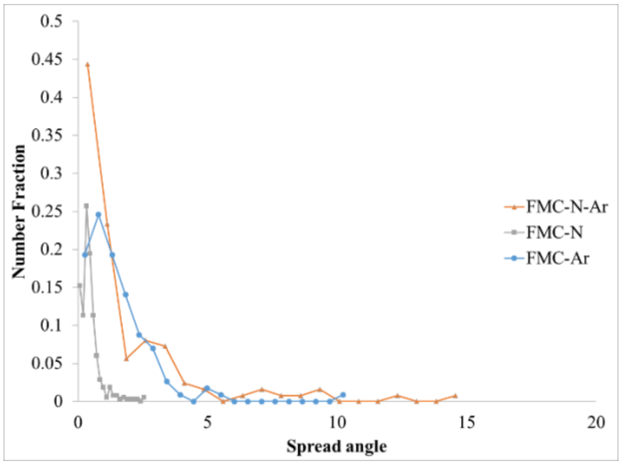

Fig 5.25 Compiled GOS Distributions for Treated Powders a) FMC-Ar b) FMC-N c) FMC-N-Ar-175

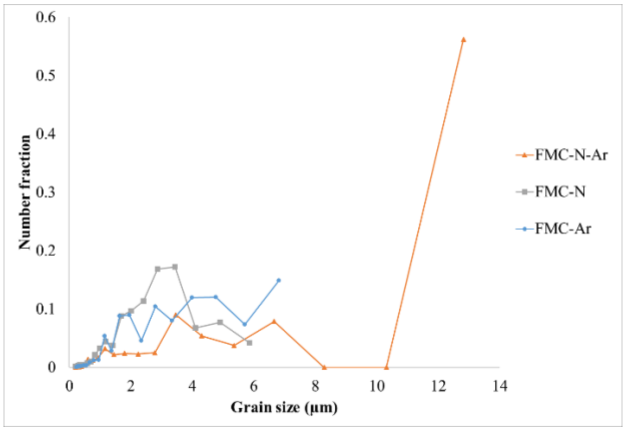

Fig 5.26 Grain Size Distribution of Treated Powders

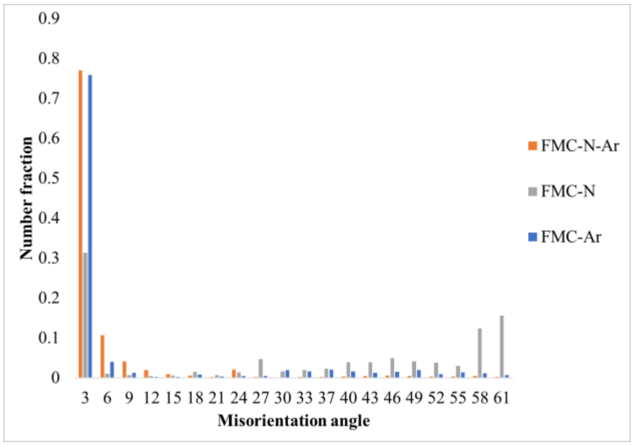

Fig 5.27 Misorientation Angle Distribution Powders

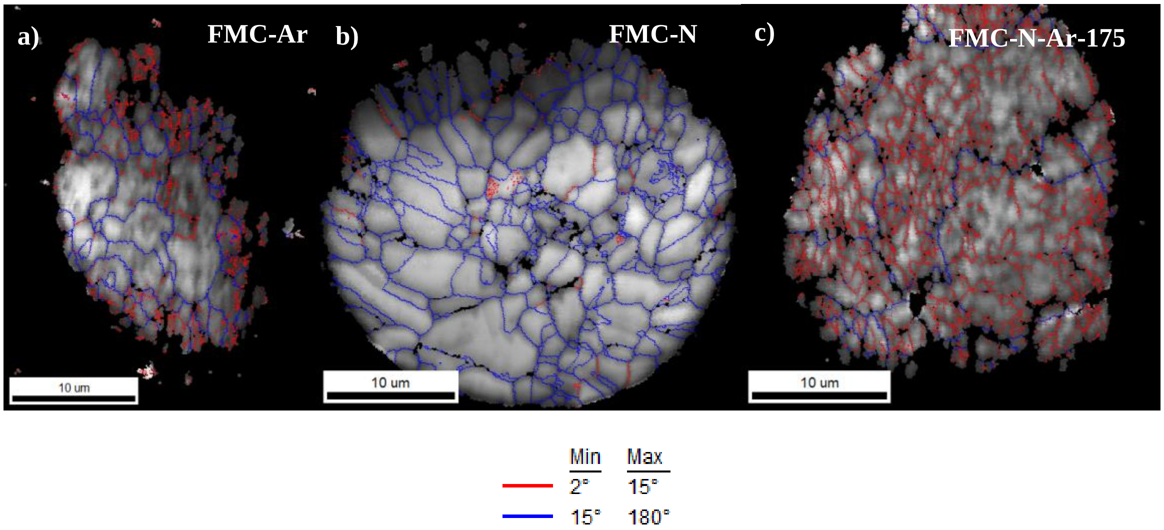

Fig 5.28 Compiled Image Quality Superimposed With Grain Boundary Angle a) FMC-Ar b) FMC-N c) FMC-N-Ar-175s

Coincident Site lattice (CSL) have known to play an important role in deformation mechanisms of materials. These typically noted as Σ boundaries. The CSL theory defines grain boundary geometry based the number of coincident lattice sites between adjacent grains. It follows an inverse relation i.e., a Σ5 boundary notes coincidence for 1/5 of the lattice points. Σ values less than 29, are known to possess special properties compared to other boundaries [53]. These sigma boundaries are represented in Fig 5.29. The single stage FMC-N powder was observed to have a higher Σ3 sites which could possibly impact the deformation mechanism during cold-spray. The FMC-Ar and FMC-N-Ar powders had more deposition efficiency compared to the FMC-N powder. This is further discussed in Chapter 6 . These Σ3 sites are also known to be twin boundaries. The higher amount of Σ3 in FMC-N could be a result of grain refinement caused by nitrogen and the thermal history of the prescribed process. Research reports for these boundaries to add a greater resistance to corrosion although in this case includes the presence of Cr_2N [54].

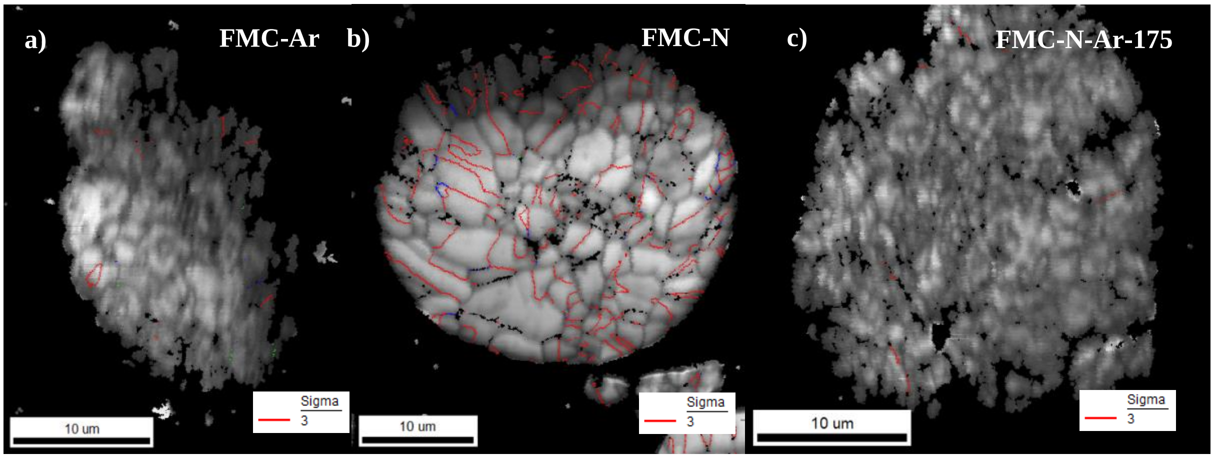

Fig 5.29 Compiled Image Quality Superimposed Sigma Boundaries a) FMC-Ar b) FMC-N c) FMC-N-Ar-175s

5.5.3 XRD

Fig 5.30 shows the compiled diffraction patterns of the powders. Table 5-6 summarizes the crystallite size, micro strain and dislocation density calculated using the diffraction peaks. The parent FMC-AS alloy had a primary ferrite (α) phase. An endothermic peak around 650°C was observed using the differential scanning calorimetry (DSC). This temperature can be ascribed to α→γ transformation. Austenite transformation with a residual ferrite phase was achieved in the single stage argon treatment (FMC-Ar) implying lack of sufficient austenite stabilizers in the composition. The reduced crystallite size from FMC-AS to FMC-Ar corresponds to grain boundary refinement possibly caused due to cold-work induced by mechanical milling.

When treated in presence of nitrogen complete austenite transformation was achieved (FMC-N). This γ phase continued to be observed in the 2-stage treatment (FMC-N-Ar). Austenite stabilization was thus provided by the elemental nitrogen [22, 18]. The crystallite size shows a significant reduction for the FMC-N alloy compared to the FMC-Ar powder. The reduced crystallite size could correspond to grain boundary refinement by nitrogen uptake which was verified in the microstructure as explored in the EBSD section of this study. Dawei, Manuel et. al [55, 56] observed similar reduction in crystallite size during nitrogen uptake of steel powders produced by high energy ball milling. A combined effect of milling and solid-state nitrogen uptake can be attributed to these changes typically seen in FMC-N. The milling time being constant post-treatment, helped in identifying the prime factor responsible for changes in the grain size.

The crystallite size later increased to a value of ~38 nm after the 2-stage treatment (FMC-N-Ar). Previous research for nitrogen powders prepared by attrition based mechanical alloying shows loss of crystallinity in the form of broadened peaks with high FWHM values [57, 58, 59, 56]. Nitrogen content exceeding beyond its solubility limit is possibly responsible for this loss due to presence of non-metallic precipitates [58, 35]. The measured XRD patterns illustrate sharp peaks indicating the maintained crystallinity of the powder particles after the treatment [60, 61]. A smaller peak shift (2θ=~0.1°) for the γ reflections is evidence of the S-phase (expanded austenite γN) [62]. Researchers also suggest a wide peak shift at α/γ reflections indicative towards a high Cr_2N content [59]. No such wide shifts were observed in this study. No CrN/Cr_2N reflections were observed. Further microstructural study was carried out to evaluate these micron/sub-micron precipitates if any.

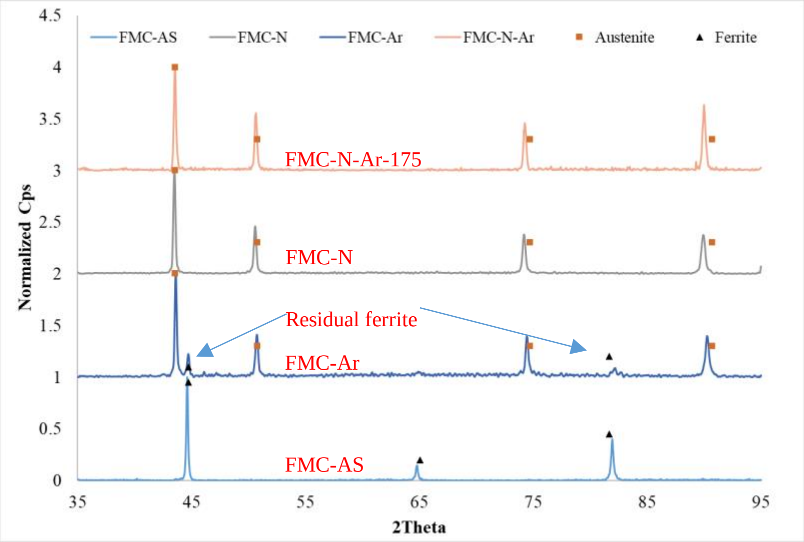

Fig 5.30 XRD Patterns of Powder Alloys for Comparison

Table 5-6 Average Crystallite Size per Scherrer Constant (K) 0.9

		γ reflection		(α reflection)	
Samples	**Crystallite size (d) (nm)**	**Dislocation density $\delta\times10^{-3}$ (nm^{-2})**	**Micro-strain $\varepsilon\times10^{-3}$**	**Dislocation density $\delta\times10^{-3}$ (nm^{-2})**	**Micro-strain $\varepsilon\times10^{-3}$**
FMC-AS	42.85±2.35	-	-	0.59	2.22
FMC-Ar	32.71±5.29	0.70	2.48	0.74	2.49
FMC-N	29.39±4.95	0.79	2.19	-	-
FMC-N-Ar-175	37.63±4.88	0.53	2.16	-	-

5.5.4 Hardness Measurements

Table 5-7 represents a summary of the mechanical properties of the powders. The base alloy measured an average hardness of 2.6-2.7 GPa which increased up to ~3GPa for FMC-Ar. Significant increase in presence of nitrogen up to ~4GPa was observed. The 2-stage annealing (FMC-N-Ar) led to softening of the particles with a significant drop in the hardness. Fig 5.31 represents compiled L-D curves obtained for all the treated powders by nano-indentation. A single indentation curve for all the powders representing the average values is presented. An elastic-plastic contact was observed for all the indentations. A maximum load of ~8000mN was recorded on the FMC-N powder particles. A lower load value of ~6000mN was recorded for the remaining powders indicating a lower hardness.

Table 5-7 Hardness Measurements on Precursors

Samples	**Micro-Hardness (GPa)/ $HV_{0.01}$**	**Nano-Hardness (GPa)**	**Reduced Modulus (E_r) (GPa)**
FMC-AS	2.6±0.25 265.105±25.63	2.72±0.37	113.37±11.75
FMC-Ar	2.869±0.33 292.56±34.45	3.13±0.73	113.61±11.25
FMC-N	4.01±0.59 409.57±60.49	3.68±0.32	125.69±13.35
FMC-N-Ar-175	**2.59±0.2** 264.55±20.86	**3.08±0.26**	134.59±10.16

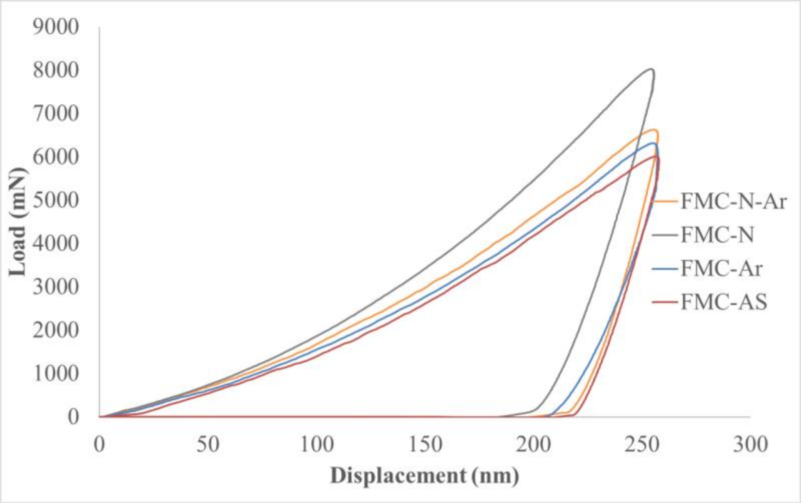

Fig 5.31 Compiled L-D Curves for Treated Alloys

Further improvements were made in the double stage procedure in-order to achieve a desired nitrogen content between 0.3-0.4 wt.% simultaneously having a maximum cold-spray deposition efficiency as discussed in Chapter 6 . The double-stage (retreatment) times were optimized to a value between 175s and 500s.

Pre-Atomized Nitrogen Powders

The method described above thus uses a base untreated alloy followed by a single stage (FMC-N) and a double stage treatment (FMC-N-Ar) in-order to eliminate nitrides. However, there are a few Nitrogen powders which can be manufactured by atomization; albeit not claimed to be precipitate free. This section focusses on evaluating these powders and post-treatment using the proposed technique.

5.6 Alloy Composition

Centrifugally atomized powders were procured from Erwin industries, MI [50]. These batch of powders were atomized in presence of nitrogen. 2 different powders with an average nitrogen content of 0.2 wt.% and 0.4 wt.% were procured. The nominal compositions of both the powders are mentioned in Table 5-8 and Table 5-9. A powder distribution of 15-60µm was procured.

Table 5-8 Nominal Composition of FMN-AS

Elements	**Cr**	**Mn**	**Al+Si+C+Mo+impurities**	**Fe**	**N_2**	**D_{mean} (µm)**
Composition (% wt.)	14-15%	22-24%	1-2%	Bal.	~0.4%	40.68

Table 5-9 Nominal Composition of FMN2-AS

Elements	**Cr**	**Mn**	**Al+Si+C+Mo+impurities**	**Fe**	**N_2**
Composition (% wt.)	14-15%	22-24%	1-2%	Bal.	~0.2%

Table 5-10 shows a LECO analysis conducted to validate the nitrogen content for the atomized powders in presence of nitrogen as claimed by the supplier.

Table 5-10 LECO Analysis of Pre-Atomized Nitrogen Powders

Powder samples	**Nitrogen content (wt %.)**
FMN-AS	0.39
FMN2-AS	0.2

Fig 5.32 shows the heat flow profiles of both the as-received nitrogen precursors. The profiles were studied for both melting and solidification behavior between 50°C-1200°C at a ramp rate of 10C/min. It was evident from the profiles that FMN-AS had a higher heat flow for a temperature range of 800°C-1200°C. This was possibly a result of higher nitrogen content in the FMN-AS powder (0.4 wt. %). Thus FMN-AS powder was chosen for further retreatment due to its high nitrogen content. FMN2-AS was just used for evaluation of microstructure in-order to understand how nitrogen content would influence the precipitation as well as the grain structure.

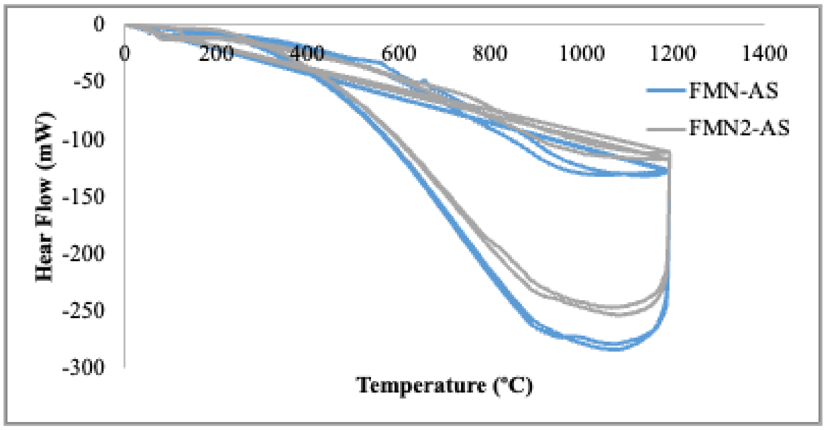

Fig 5.32 DSC Curves for a Heat-Cool Cycle of FMN As Received Powders

Table 5-11 shows the experimental parameters used for the retreatment of FMN-AS powder. This retreatment time was optimized for a desired nitrogen content and maximum cold-spray deposition efficiency as discussed in Chapter 6 . As mentioned in previous sections, the treated agglomerated powder was mechanically milled post the treatment to recover the original particle size. Table 5-12 shows the LECO analysis of the retreated powder compared to the as received nitrogen powder. An average measurement of 4 readings is presented with a nominal standard deviation of ± 0.02 wt.%.

Table 5-11 Experimental Parameters for Retreatment of FMN-AS

Samples	**Temperature (K)**	**Dwell time (s)**	**Purge gas**
FMN-Ar-500	1353	500	Ar/H_2 only

Table 5-12 LECO Analysis of FMN-AS and the Retreated Powders

Powder samples	**Nitrogen content (wt %.)**
FMN-AS	0.39
FMN-Ar-500	0.31

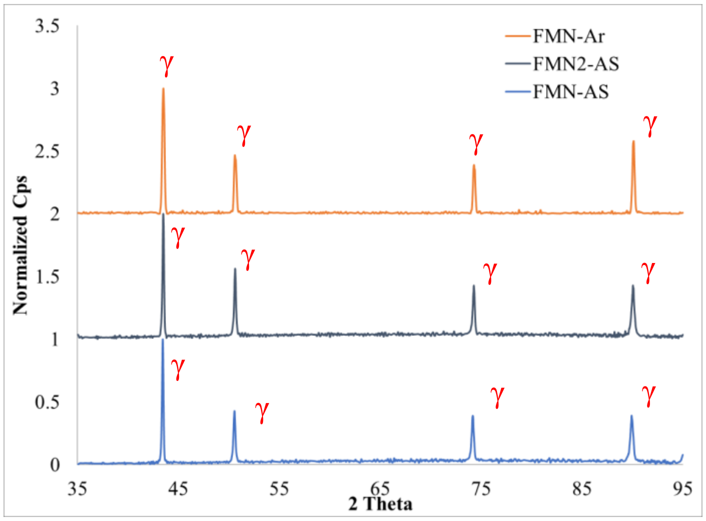

Fig 5.33 X-ray Diffraction Patterns for As Received and Retreated FMN Powders

Table 5-13 Average Crystallite Size per Scherrer Constant (K) 0.9

		γ reflection	
Samples	**Crystallite size (d) (nm)**	**Dislocation density $\delta \times 10^{-3}$ (nm^{-2})**	**Micro-strain $\varepsilon \times 10^{-3}$**
FMN-AS	45.15±9.17	0.53	1.452
FMN2-AS	47.77±7.75	0.46	1.546
FMN-Ar (500s)	43.81±6.76	0.54	1.679

Fig 5.33 and Table 5-13 show the results of the crystal structure of the precursors measured with the aid of X-ray diffraction. A crystalline structure was maintained; evident by sharp peaks [60, 61]. Purely austenitic microstructure was visible across the entire FMN family.

Fig 5.34 through Fig 5.37 shows EBSD scans of all the FMN precursor family. Fig 5.34 describes the data for FMN2-AS powder. Only indexed portions are shown. Nitrogen was clearly presented a short-range order (Cr-N) which is desired. Although a nitrogen content of 0.2wt. % has low corrosion and mechanical performance compared to a higher nitrogen content. This powder was not used for further development due to its low nitrogen content.

Fig 5.35 represents scans for the FMN-AS powder which was used as a base precursor for its retreatment as per parameters in Table 5-11. No Nitride precipitation was visible in this precursor as well. This precursor contained a non-homogenous grain structure with a varied population of coarse as well as fine grains. Although this powder had its desired nitrogen content the respective cold-sprayed coating had a very less deposition efficiency due to the grain structure.

Fig 5.36 represents the scans for retreated FMN-AS i.e FMN-Ar-500s powder. While marinating the SRO (CR-N) without any precipitation a relatively homogenous grain structure was achieved simultaneously maintaining the particle hardness. This grain structure was thus proven beneficial for the cold-sprayed coating as discussed in the next chapter. Relative to FMN-AS the population of LAGB (2°-15°) was reduced after the retreatment.

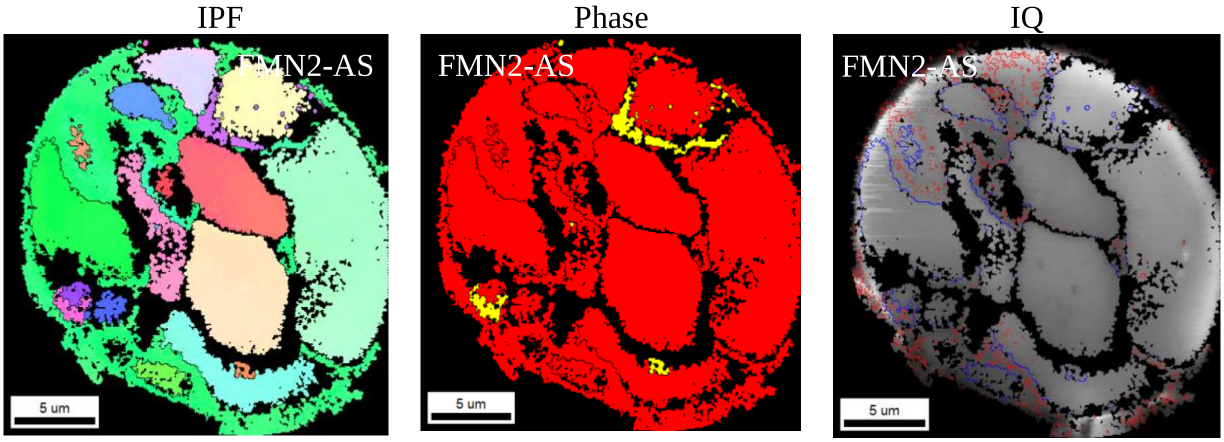

Fig 5.34 EBSD Scans with IPF, Phase Maps and Misorientation Grain Boundaries for FMN2-AS Precursor

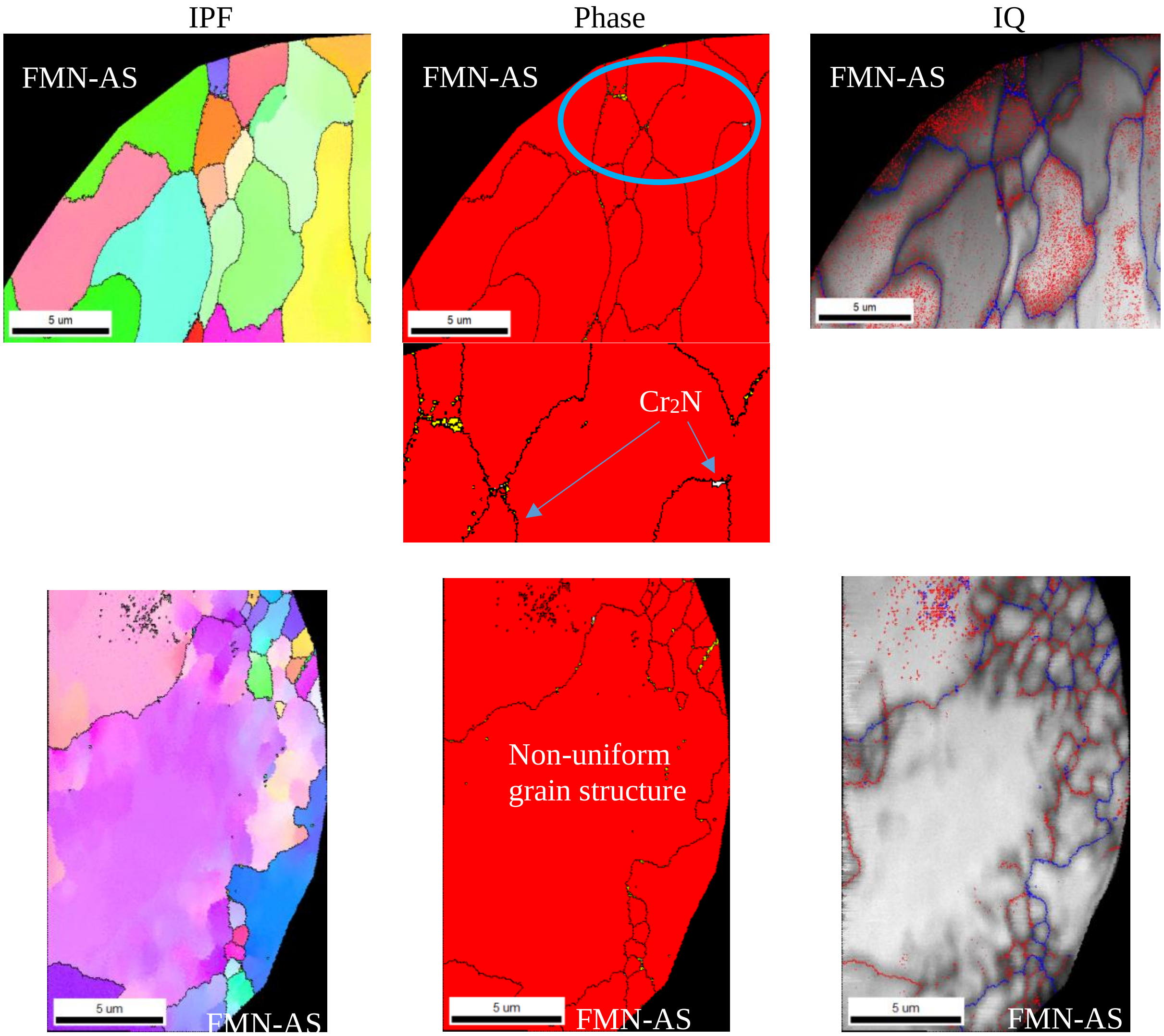

Fig 5.35 EBSD Scans with IPF, Phase Maps and Misorientation Grain Boundaries for FMN-AS Precursor

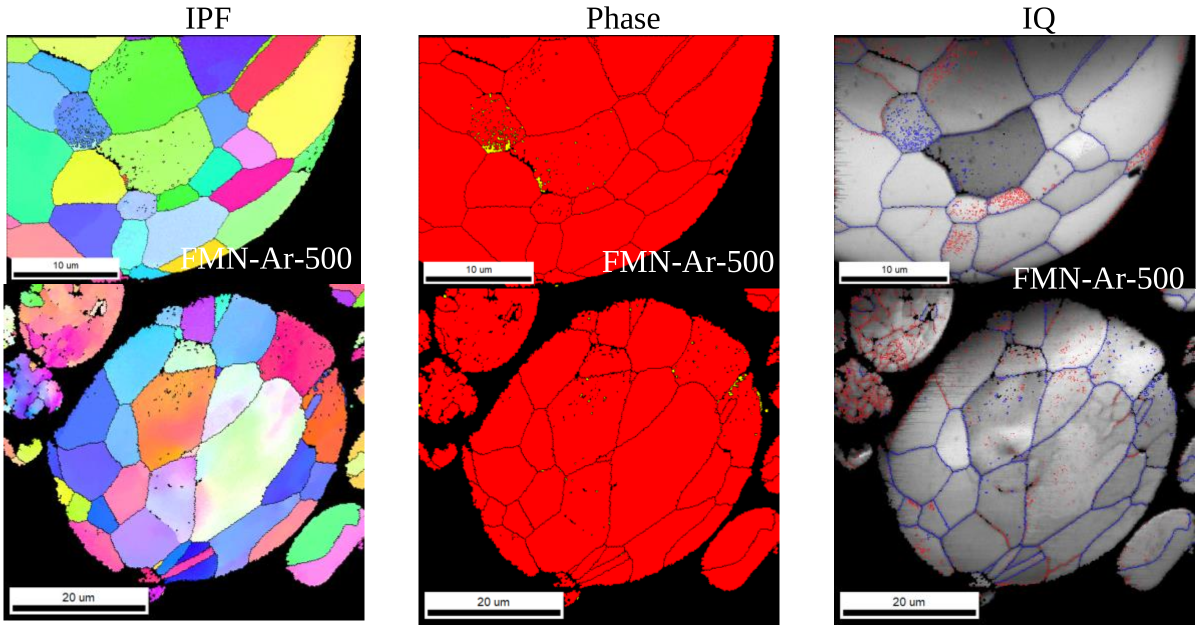

Fig 5.36 EBSD Scans with IPF, Phase Maps and Misorientation Grain Boundaries for FMN-Ar-500s Precursor

Fig 5.37 Legend for EBSD Scans

Table 5-14 represents a summary of the mechanical properties of the powders (pre-atomized with nitrogen). The as received alloy FMN-AS measured an average hardness of 3.9-4.0 GPa. This higher value was a result of the high nitrogen content (0.39 wt.%) achieved during atomization. The FMN2-AS with a slightly lower nitrogen content (0.2 wt.%) displayed a lower hardness value of ~ 3.6 GPa. Retreatment of the FMN-AS powder aided in retaining the nitrogen content simultaneously maintaining the hardness value of ~3.9 GPa. Fig 5.38 represents compiled L-D curves obtained for all the treated powders by nano-indentation. A single indentation curve for all the powders representing the average values is presented. An elastic-plastic contact was observed for all the indentations. A maximum load of ~7500mN was recorded on the FMN powder particles. A lower load value of ~6000mN was recorded for the remaining powders indicating a lower hardness.

Table 5-14 Hardness Measurements of Precursors

Samples	**Micro-Hardness (GPa)/ $HV_{0.01}$**	**Nano-Hardness (GPa)**	**Reduced Modulus (E_r) (GPa)**
FMN-AS	4.36±0.84 444.85±86.48	3.928±0.13	125.44±1.36
FMN2-AS	3.94±0.61 402.2±62.39	3.68±0.22	127.45±7.99
FMN-Ar-500s	4.11±0.37 420±38.3	3.8±0.13	177.04±2.98

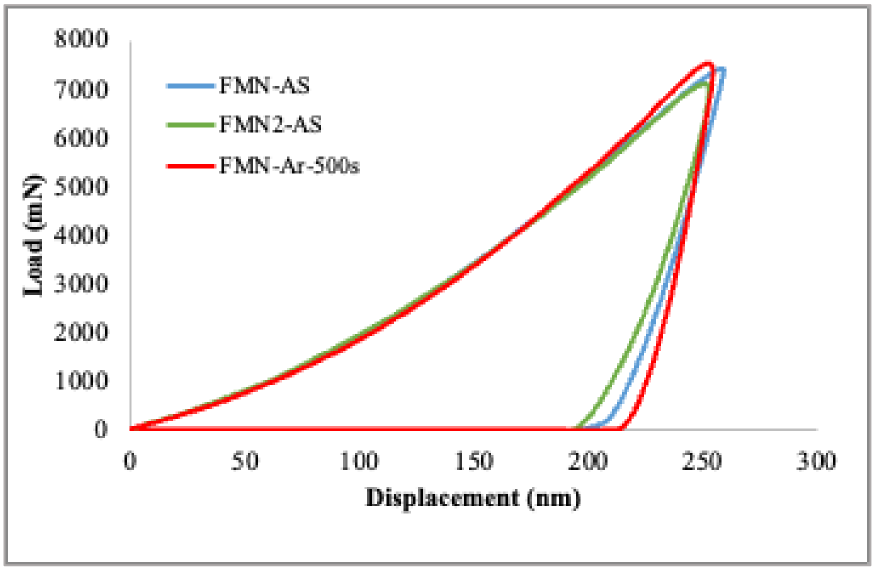

Fig 5.38 Load vs. Displacement Curves for as Received and Retreated FMN Powders

This process thus demonstrates an ability to utilize nitrogen powders existing in the market and increase their usability while ensuring the short-range order. A retreatment of such powders is thus recommended in-order to ensure the short-range order as well as maximize the mechanical properties of the material. In-order to investigate the mechanical properties and corrosion properties of the powders they were further translated to functional coatings using a solid-state deposition as discussed in the next chapter.

Chapter 6 Performance Evaluation Using Cold-spray Technique

6.1 Functional Coating Development with Solid-State Deposition

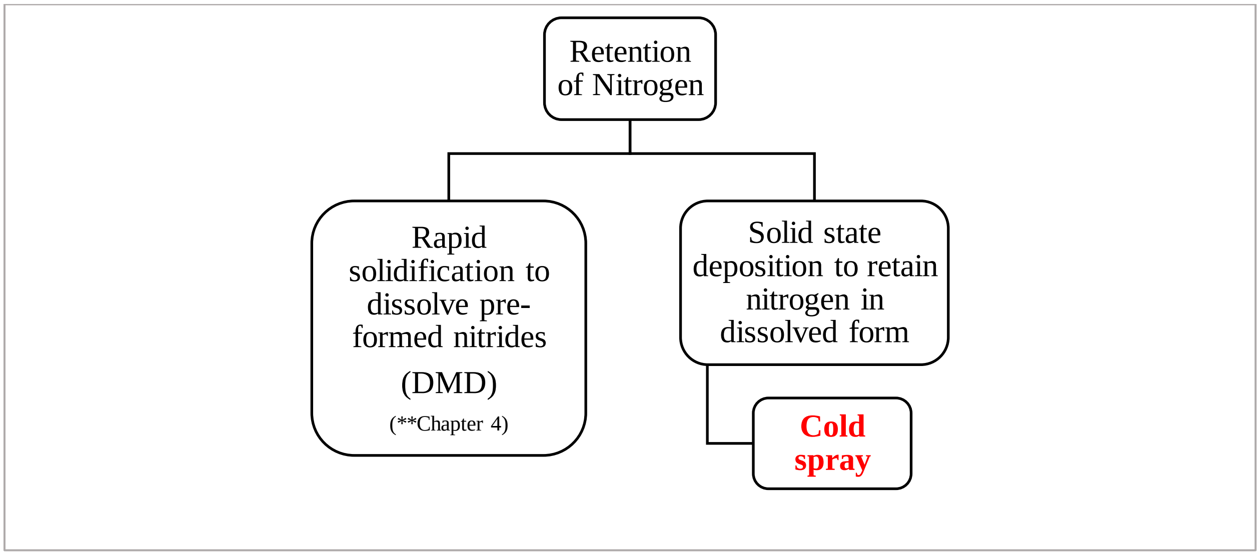

Fig 6.1 Coating Development Strategies

Functional coatings were produced by assistance of solid-state deposition technique in-order to retain the dissolved nitrogen or in the short-range order (SRO) to avoid further precipitation by other techniques involving melting of the powder alloy.

6.1.1 Cold-Spray

Cold spray is one of the prime technologies of the thermal spray family which is a traditional AM method. It was discovered and patented by a Russian scientist Anatolli Papyrin et al. in late 80's [63]. The name cold spray is derived from the process temperatures, where it doesn't involve any melting of the particle and is carried out at low temperatures relative to other AM techniques. This process uses a high-pressure gas usually helium/nitrogen subject to a convergent divergent a.k.a

De-Laval nozzle. The expansion ratio due to the con-di feature enables a super-sonic gas jet. When powder precursors are allowed to enter the nozzle, they exit with a very high particle velocity. The expansion ratio plays a vital role in affecting the particle velocity achieved. These high velocity particles after reaching a critical velocity adhere to the substrate thereby creating a bond. Fig 6.2 shows a typical particle velocity schematic relative to the deposition stages. An optimized particle velocity depends upon the particle size and the process parameters as well as the mechanical ability of the precursors to undergo plastic deformation.

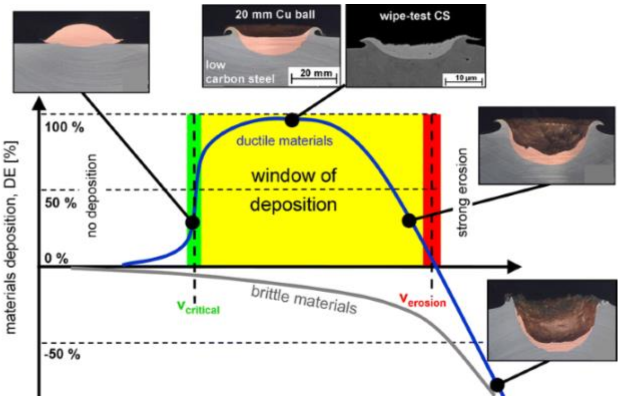

Fig 6.2 Effect of Particle Velocities on Cold-Spray Deposition [64]

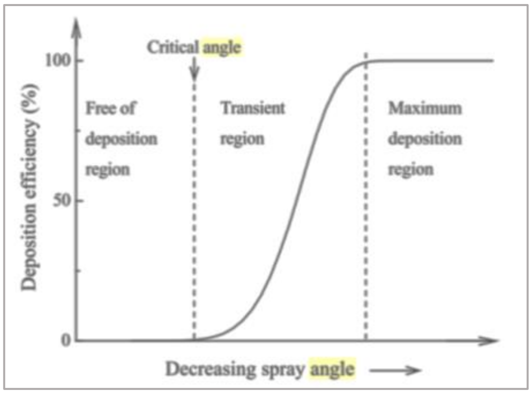

Fig 6.3 Effect of Spray Angle on Deposition Efficiency [65]

This process involves a set of numerous parameters which need to be optimized for a coating with desired properties. Following are the typical parameters necessary for optimization:

- Type of Nozzle used (convergent –divergent nozzle)
- Type of gas used (Helium/N_2
- Gas pressure
- Nozzle Standoff
- Powder flow rate
- Career gas flow
- Gas temperature
- Type of substrate

Affect particle velocity

When a powder precursor is subjected to high pressure through a convergent-divergent nozzle it achieves high velocities which help in adhesion when impacted on the substrate. Thus, particle velocities are highly influenced by the type of gas, type of nozzle used (throat size), gas pressure powder flow rate, etc. Fig 6.5 shows the effect of spray angle on the deposition efficiency.

All the other thermal spray/AM techniques typically involve a high-temperature processes which lead to phase transformations, degassing etc. However, coldspray technique being deployed under low temperatures is known to translate the powder precursor as is to a functional bulk coating without any oxidation and phase transformations [66]. In this case cold-spray deposition would thus aid in retention of the nitrogen in its interstitial solid-solution and a short-range order (SRO) as achieved in the treated precursors.

Researchers are striving to make cold spray may a reliable and practical technique that will enable 3D printing of engineering components at low temperatures. [67].

6.2 Coating Deposition

A convergent-divergent nozzle with a rectangular cross section was used in this study. The details of the nozzle and deposition parameter optimization are presented in a research article from one of the members of the additive manufacturing group at the UM-Dearborn [68]. Nitrogen was used as process and carrier gas. Deposition was conducted with 3.44 Mpa process gas pressure and 0.47 Mpa carrier gas pressure. Powder was fed using a Thermach AT-1200HP (Appleton, WI, USA) powder feeder. Substrates were degreased with alcohol; no additional surface preparation was performed. During deposition, nozzle was stationery while substrate was rotated on a 2 axis CNC system. A 50% overlap of coating was maintained during deposition. The rotation speed was varied to maintain constant linear surface velocity of approximately 12mm/s across the surface. Due to limited development of the powder, a small sector area was deposited as shown in Fig 6.4 and later evaluated for their performance.

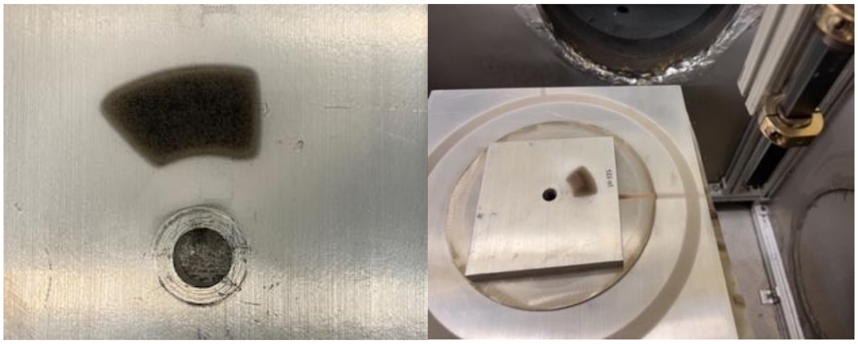

Fig 6.4 Cold-Spray Deposit of High Nitrogen Alloy on 6061 Substrate

6.3 Coating Characterization and Analysis

6.3.1 Deposition Efficiency

All the prepared precursors (as received as well as treated) were deposited on lightweight Al 6061 substrates. Al 6061 was chosen as the substrate candidate because of its ductility and softness as well as its lightweight in-order to aid more amount of deposition when subjected to high particle velocities.

Optimizing Retreatment Time for Deposition Efficiency:

The prepared nitrogen precursors were analyzed thoroughly for their micro-structure and micro/nano hardness. However, in-order to optimize the deposition efficiency the double stage treatment times were varied from 175-500s simultaneously maintaining the desired nitrogen content. Fig 6.5 shows a variation of the deposited coatings as an increase of the double stage dwell time. Fig 6.6 shows the deposition efficiencies of all the FMC based precursors.

The base precursor without nitrogen deposited up to ~40%. A single stage retreatment (FMC-N) in presence of nitrogen significantly reduced the cold spray ability of the powder due to the hard precipitates as visible from the powder EBSD maps. A deposition efficiency of ~10% explains the presence of nitrides and their difficulty to undergo plastic deformation. The Retreating the FMC-N in presence of argon (double stage) the deposition efficiency was observed to climb with the retreatment time. A maximum deposition efficiency of ~30% was reported for a double stage retreatment time of 500s. thus a retreatment time of 500s was chosen as the best parameter for the treatment. As discussed in Chapter 5 for the FMN based precursor a retreatment time of 500s was used based on the optimized times from the FMC based precursors. Fig 6.7 shows the deposition efficiencies of all the FMN based precursors. The as received FMN (FMN-AS) had a lower deposition efficiency about ~16% which significantly increased to ~36% in FMN-Ar (500s) coating.

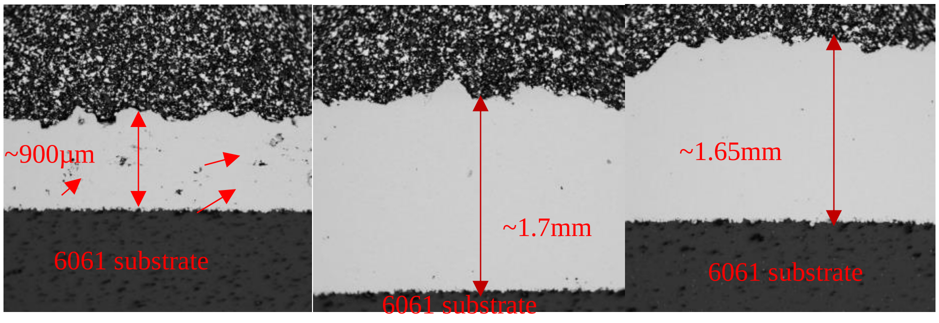

Fig 6.5 Cross-Section Profiles for Double-Stage (FMC-N-Ar) Treatment Times

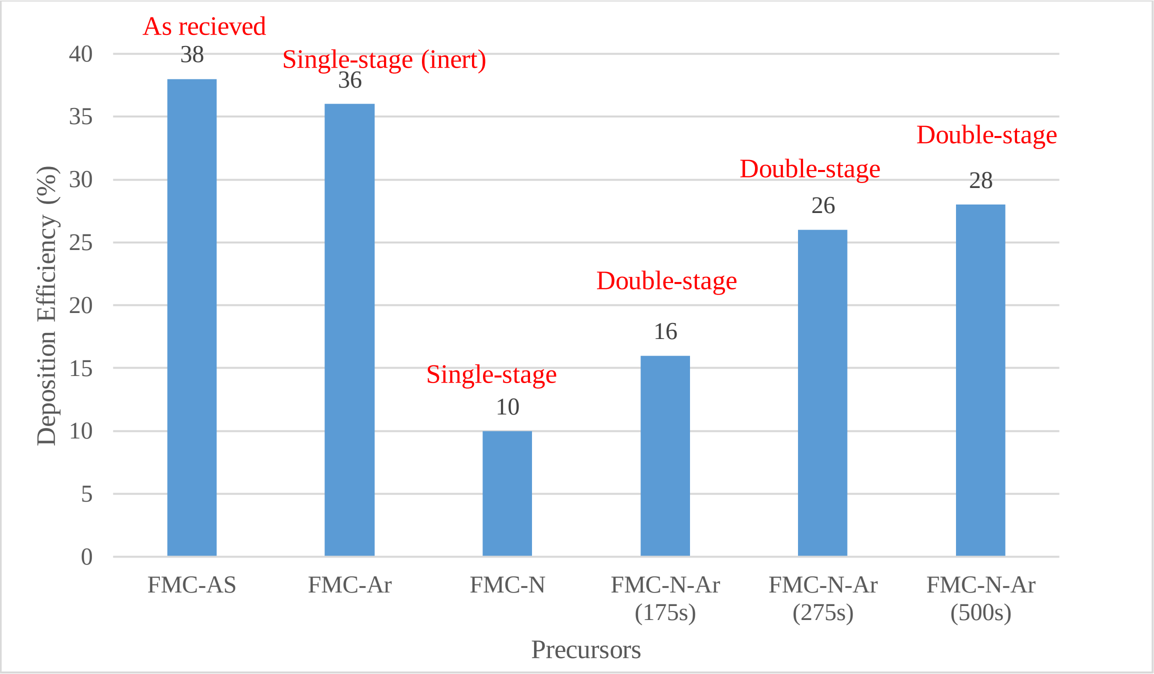

Fig 6.6 Comparison of Deposition Efficiencies for Various Treatment Times for Double Stage (Argon retreatment)

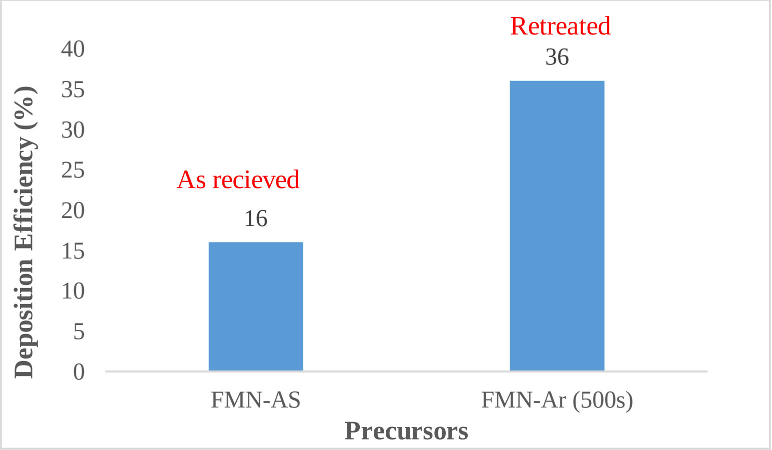

Fig 6.7 Comparison of Deposition Efficiencies for FMN and FMN-Ar-500s

6.3.2 Nitrogen Content

While achieving a higher deposition efficiency it was necessary to ensure a minimized nitrogen loss i.e., degassing of nitrogen content from the powder precursor. LECO measurements were thus taken at various points on the cross-section of the coating to ensure homogeneity. Table 6-1 displays the nitrogen content translated from the starting precursor to its coating. The FMC-N coating showed a significant nitrogen loss from ~0.34 to ~0.25 wt.% This possibly explains the presence of nitride precipitates in the powder, which makes the plastic deformation of this powder difficult. The retreatment of FMN powder i.e., the FMN-Ar powder and its coating showed a minimized loss in the nitrogen content.

Table 6-1 Average Nitrogen Content for Prepared Powders and Respective Cold-Sprayed Coating

Sample Type	**Nitrogen content (%wt.)**	**Std. deviation**
FMC-AS Powder	0.05	0.01
FMC-N Powder (175s)	0.34	0.05
FMC-N Cold-sprayed coating	0.25	0.02
FMN-AS powder	0.39	0.01
FMN-Ar-500s Powder	0.31	0.02
FMN-Ar-500s cold sprayed coating	0.29	0.02

6.3.3 Microstructural Characterization

Fig 6.8 through Fig 6.14 show various cross-sections of the deposited coatings. The FMC-AS coatings i.e untreated precursor displayed a higher porosity as visible in Fig 6.8. This porosity seemed to disappear for the double stage and FMN coatings. A dense coating was achieved with the FMN-Ar(500s) powder. Fig 6.13 and Fig 6.14 show an etched cross-section of the Double stage FMC-N-Ar (500s) and FMN-Ar (500s) coatings. Particle boundaries were clearly revealed in the microstructure. Because of the hardness and presence of nitrogen in the coating the etching process did not reveal grain boundaries. Further microstructural studies are thus recommended to understand the grain size of the coatings.

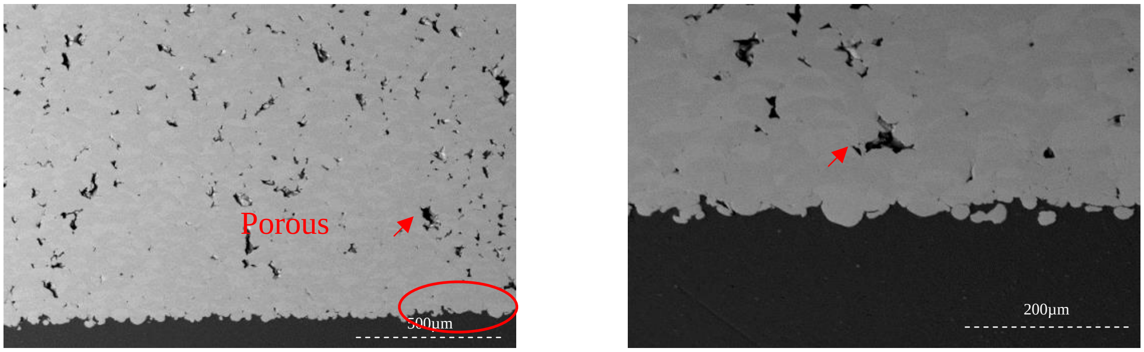

Fig 6.8 FMC-AS Coating Cross-Section a) Low Mag b) High Mag at Bond Line (Red)

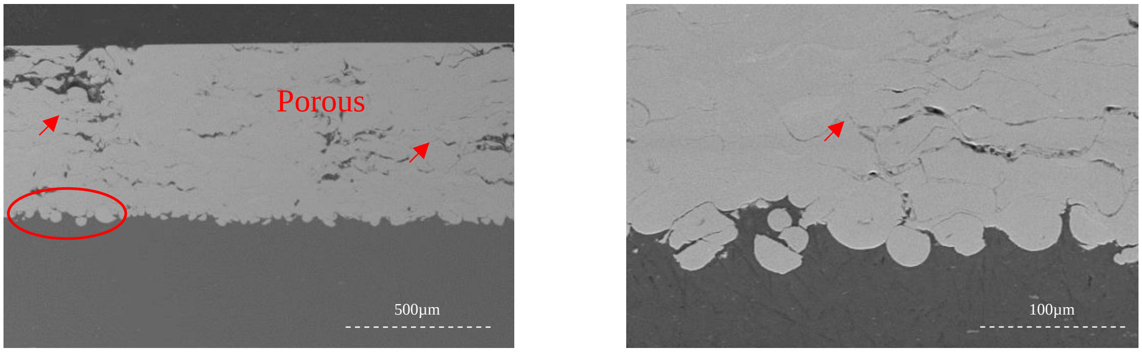

Fig 6.9 FMC-N Coating Cross-Section a) Low Mag b) High Mag at Bond Line (Red)

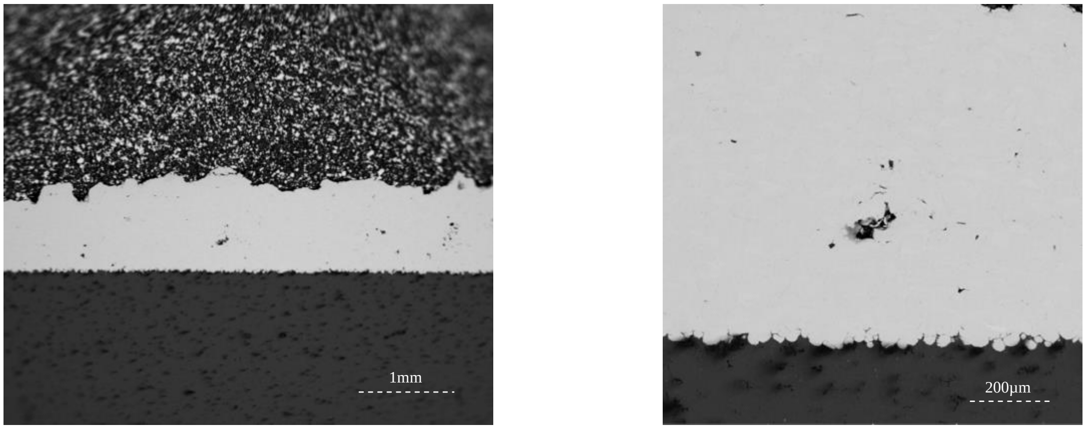

Fig 6.10 FMC-N-Ar (175s) Coating Cross-Section a) Low Mag b) High Mag at Bond Line (Red)

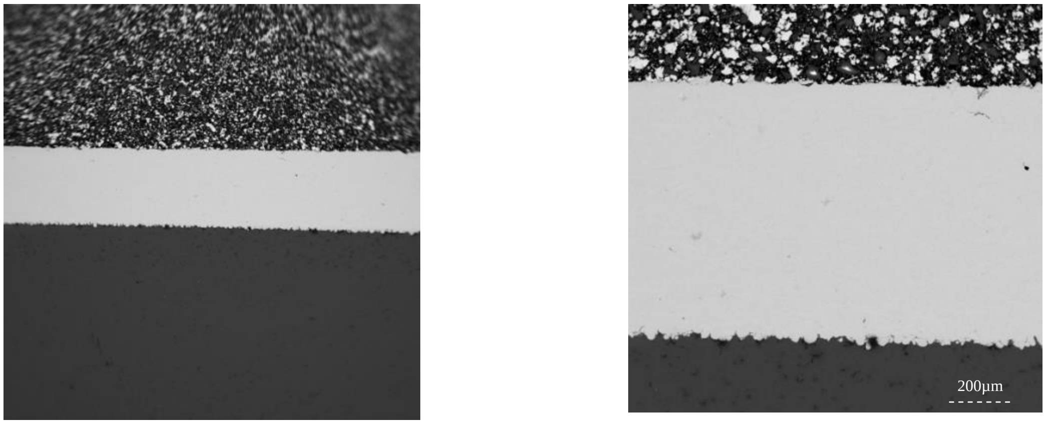

Fig 6.11 FMN-AS Coating Cross-Section a) Low Mag b) High Mag at Bond Line (Red)

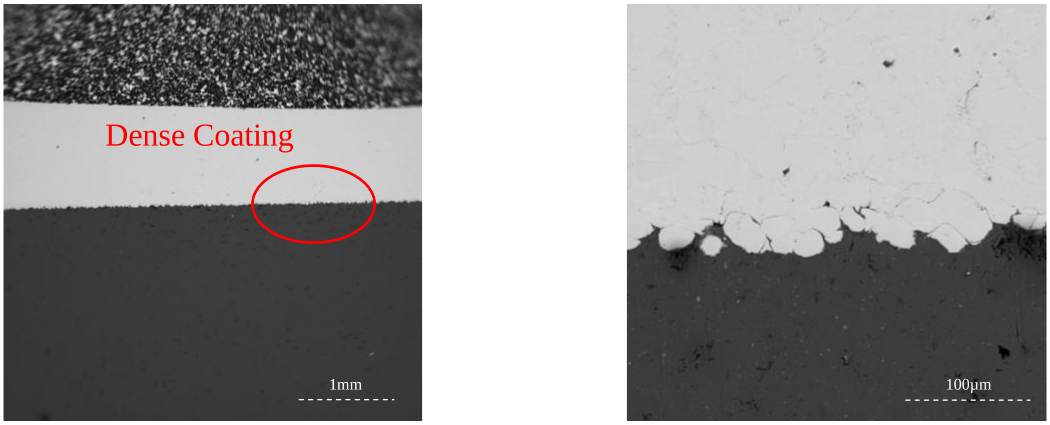

Fig 6.12 FMN-Ar-500s Coating Unetched Cross-Section a) Low Mag b) High Mag at Bond Line (Red)

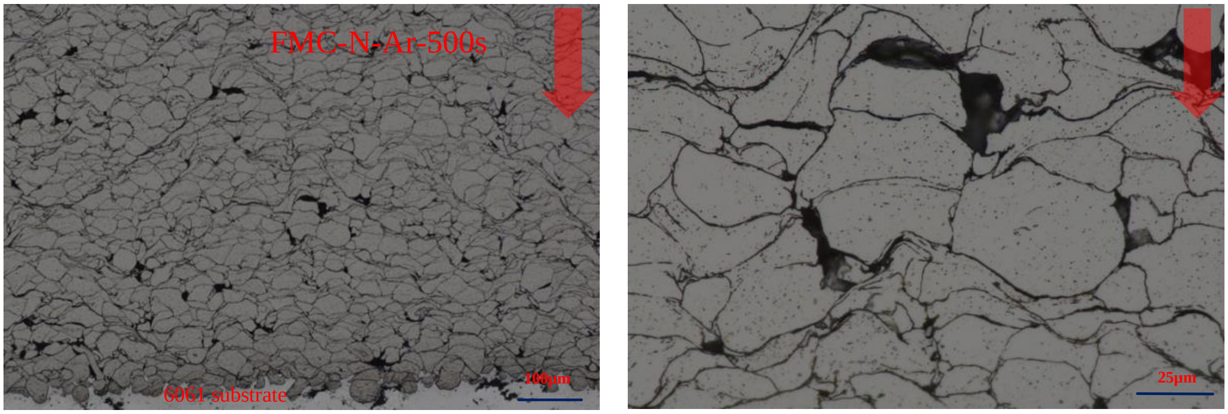

Fig 6.13 Optical Image of Etched Cross-Section of a) FMC-N-Ar (500s) Coating Revealing Particle Boundaries

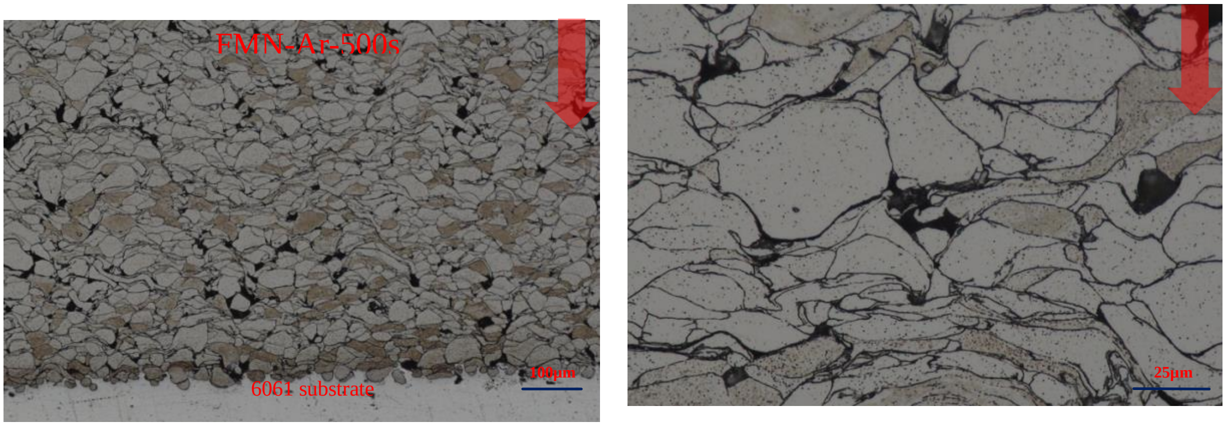

Fig 6.14 Optical Image of Etched Cross-Section of FMN-Ar (500s) Coating Revealing Particle Boundaries

6.3.4 Micro-Hardness

Fig 6.15 presents a Vickers hardness profile taken at 3 different locations along the cross-section. SS316 despite known for its extreme corrosion resistance measured a very low hardness of ~240HV. The untreated precursor FMC-AS due to the absence of nitrogen measured a lower hardness value ~265HV. This value was observed to increase significantly to ~410HV after a single stage treatment (FMC-N). This rise in the hardness value was possibly due to the grain refinement and presence of nitrogen. Retreating this powder i.e the double stage treatment (FMC-N-Ar) softened the coating to a certain extent simultaneously maintaining the nitrogen content. The coating softening could be result of the grain coarsening due to the retreatment.

The FMN-AS coating had a hardness value of ~390 HV. Retreating this powder by the parameters mentioned in Chapter 5 (FMN-Ar 500s) didn’t alter the hardness simultaneously maintaining the desired nitrogen content. The homogeneity in the grain structure of the powder in FMN-AS could be the reason of the variance in corresponding coating hardness.

To summarize, by the double stage treatment as well as retreatment of pre-atomized powder, cold-sprayed coatings of a high hardness value were produced, with no Cr_2N precipitation and maintaining the nitrogen in interstitial solid solution.

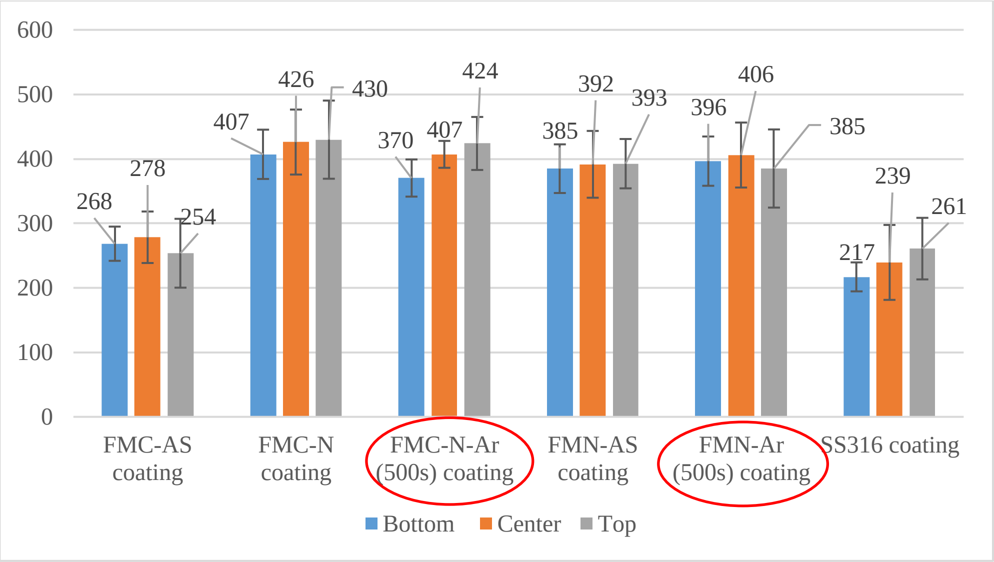

Fig 6.15 Hardness Profiles of Coatings

6.3.5 Wear Characteristics

Fig 6.16 shows a tribometer profile of the coatings representing a sliding behavior against WC ball. The sliding tests usually show a rapid change in the COF values before achieving a steady state. The coefficient of friction corresponds to a ratio of friction force and applied normal force which was 9N in these tests. This is a function of the starting surface finish of the coatings. After this initial rapid change, a debris starts to collect on the wear track causing increase in the friction. This debris then leads to surface fretting. Micro-cut or Micro-plough effects are common during such events. A highest COF was measured for the stainless-steel coating. The FMC-N and FMN-Ar coatings displayed a similar COF value representing the presence of nitrogen. A low debris was collected from these coatings relative to FMC-AS and SS 316 coatings. Fig 6.17 presents the wear depths of these profiles. The U-shape wear scars indicate bulk material removal. An higher depth at the edge of the contact is an indicator of plastic deformation or embedding of debris. A highest wear depth with a wider track was measured for the FMC-AS coating which is justified by the absence of elemental nitrogen as well as the presence of micro-pores as seen in the cross-section of the coating in Fig 6.8. The FMC-N (singe stage) coating had relatively higher wear depth despite of nitrogen content which could possibly be due to the pores as seen in Fig 6.9. Comparable wear depths were achieved for FMN-AS, and FMN-Ar coatings which were a result of dense coatings as seen from the morphology along with the presence of elemental nitrogen. The figure represents the best reading taken from 3 repetitive experiments.

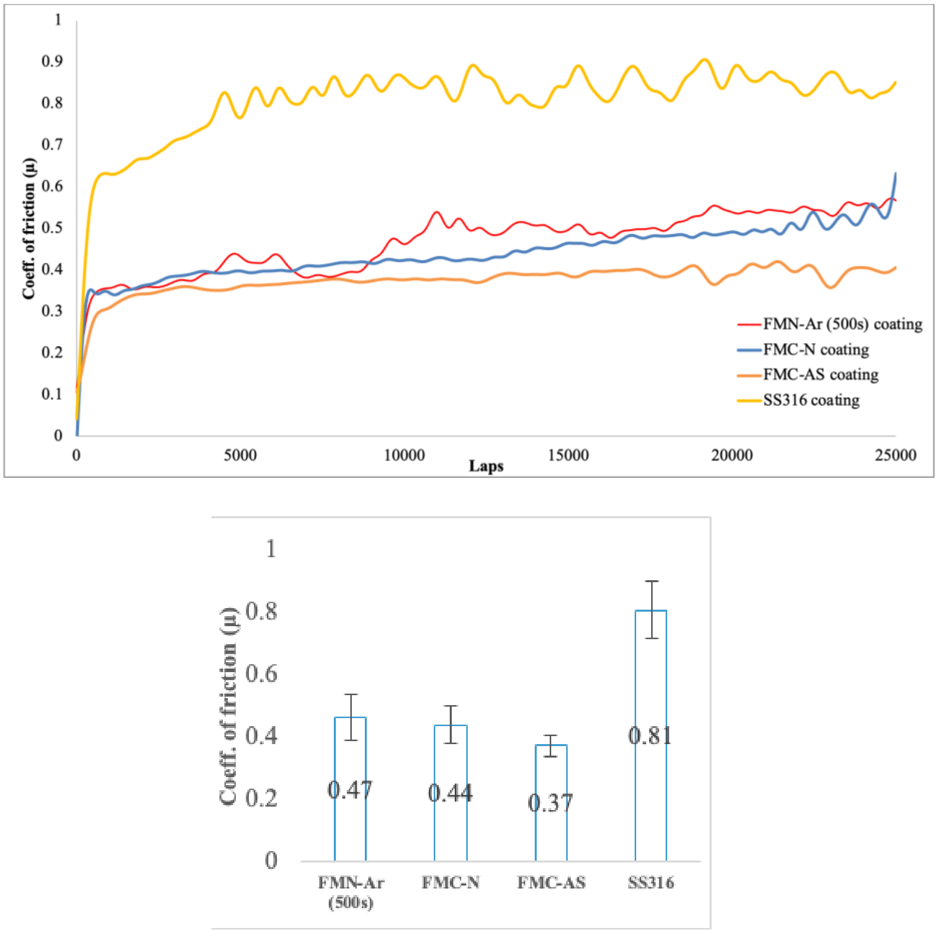

Fig 6.16 Tribometer Profile of Cold-Sprayed Coatings

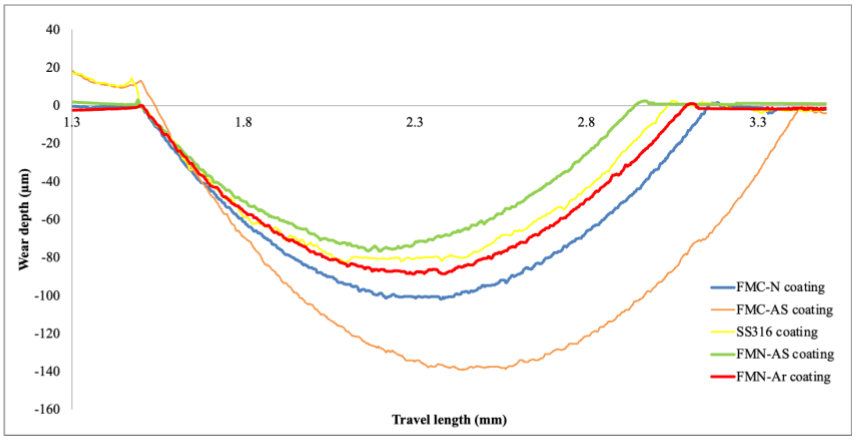

Fig 6.17 Surface Profile for Wear-Depth of Coatings

6.3.6 Corrosion Characteristics

Stainless steel is one of the widely used alloy well known for its corrosion resistance in any kinds of media be it alkaline, neutral, or acidic [69]. Cold-sprayed stainless-steel (typically SS316) coatings are also widely used as protective layers on lightweight or corrosive surfaces. A primary austenite phase; as well as the elemental constituents viz. Mn and Cr the corrosion resistance of these steels is high. However, these stainless coatings are reported to delaminate when exposed to a saline media for a longer time. In-order to validate this fact, a salt bath- test was conducted for the SS316 cold-sprayed coating. A standard setup was built complying the ASTM B117 [42]. A 5% NaCl solution mist was used during the exposure. Fig 6.18b represents the SS316 coating post 96 hours of salt-bath exposure. The SS316 coating delaminated from its aluminum substrate. In-order to validate the proposed composition for a higher Mn and lower Cr content the untreated precursor coating was also subjected to the salt bath exposure. Fig 6.19 represents the in-tact bond line of the Untreated FMC-AS coating showing no signs of delamination.

Fig 6.18 Cold-Sprayed Coating a) FMC-AS; b) SS316 on Al 6061 Substrates After a 96hrs Salt-Fog Test

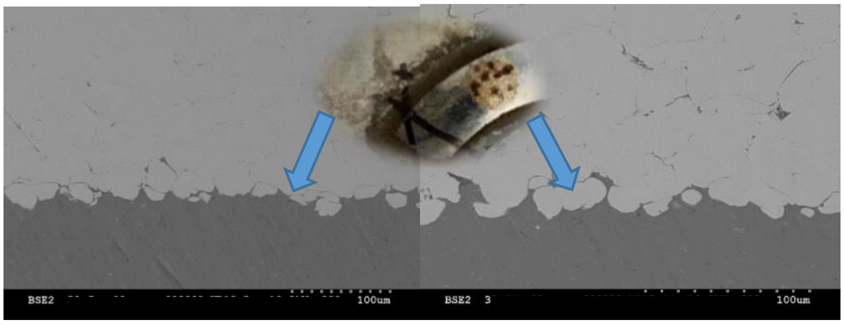

Fig 6.19 Bond Line of Untreated FMC-AS Alloy Post Salt Bath Test (No Delamination Observed)

Fig 6.20 shows the Open-circuit profiles for all the cold-sprayed coatings. The OCP value was observed to drop steadily within the timeframe of 3600 sec. This could be a possibility of lack of passivation in a chloride environment [70].

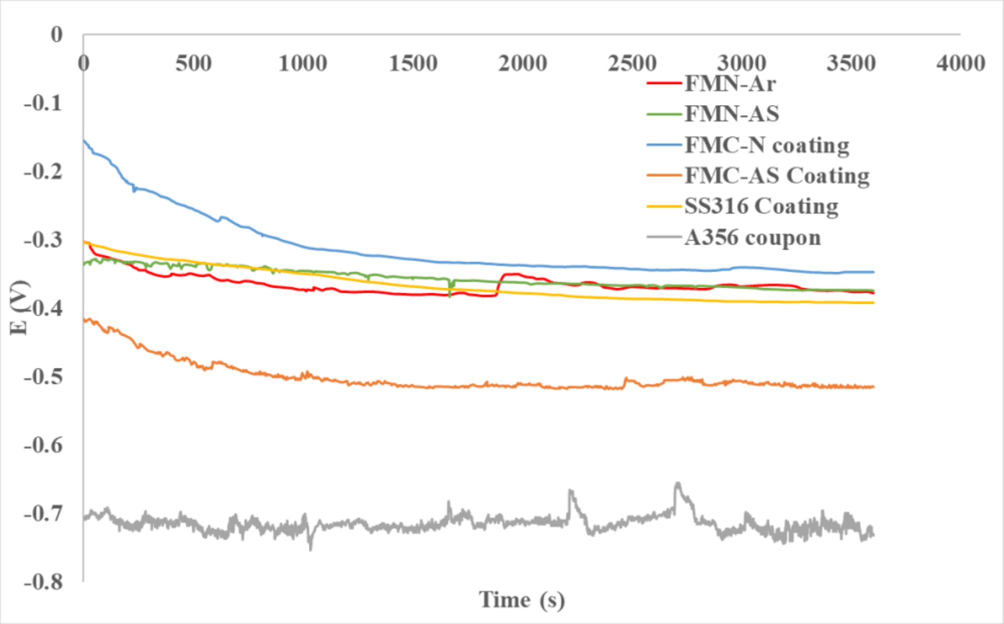

Fig 6.20 Open Circuit Profiles for Cold-Sprayed Coatings

Fig 6.21 shows potentio-dynamic behavior of the cold-sprayed coatings of the treated and as-received precursors. Table 6-2 summarizes the Tafel fitting results of the coatings. SS316 cold-sprayed coating (yellow curve) displayed a passivation peak which clearly delineates from other coatings. The Single stage FMC-N coating (blue) also displayed a distinct passivation transition. Other coatings were also observed to have passivation transitions not as distinct as FMC-N and SS316. No passivation transition was observed for A356 coupon which is typical. The FMN-Ar displayed superior characteristics in terms of a lower Ecorr as well as Icorr value. The corrosion current (Icorr) being a kinetic value thus represents the corrosion rate of the material. A low Icorr was obtained for FMN-Ar relative to any other coatings.

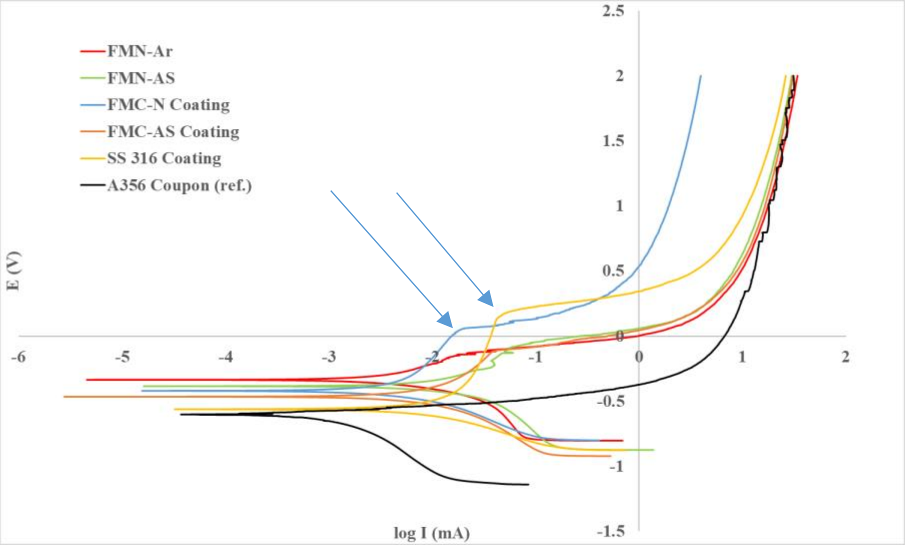

Fig 6.21 Potentiodynamic Curves of Cold-Sprayed Coatings

Table 6-2 Corrosion Potential and Tafel Slopes for Cold-Sprayed Coatings

Sample	**Ecorr (mV)**	**Icorr (µA/cm2)**	**ßa**	**ßc**
FMN-Ar-500s Coating	-332.62	2.327	175.2	119.2
FMN-AS Coating	-381.412	9.785	341.7	214.1
FMC-N Coating	-413.338	1.694	141.9	116
FMC-AS Coating	-468.004	7.51	408.4	279.4
SS316 Coating	-553.88	7.268	359.4	226.7
A356 Coupon	-600.611	0.692	55.5	249.0

Fig 6.22 shows the galvanic corrosion performance of the coatings w.r.t current density levels over a period. A A356 coupon was used as the reference material in terms of a galvanic coupling. The FMC-N and FMN-Ar coatings displayed a similar corrosion current over time axis. The test was conducted for 5 repetitive cycles to ensure stability.

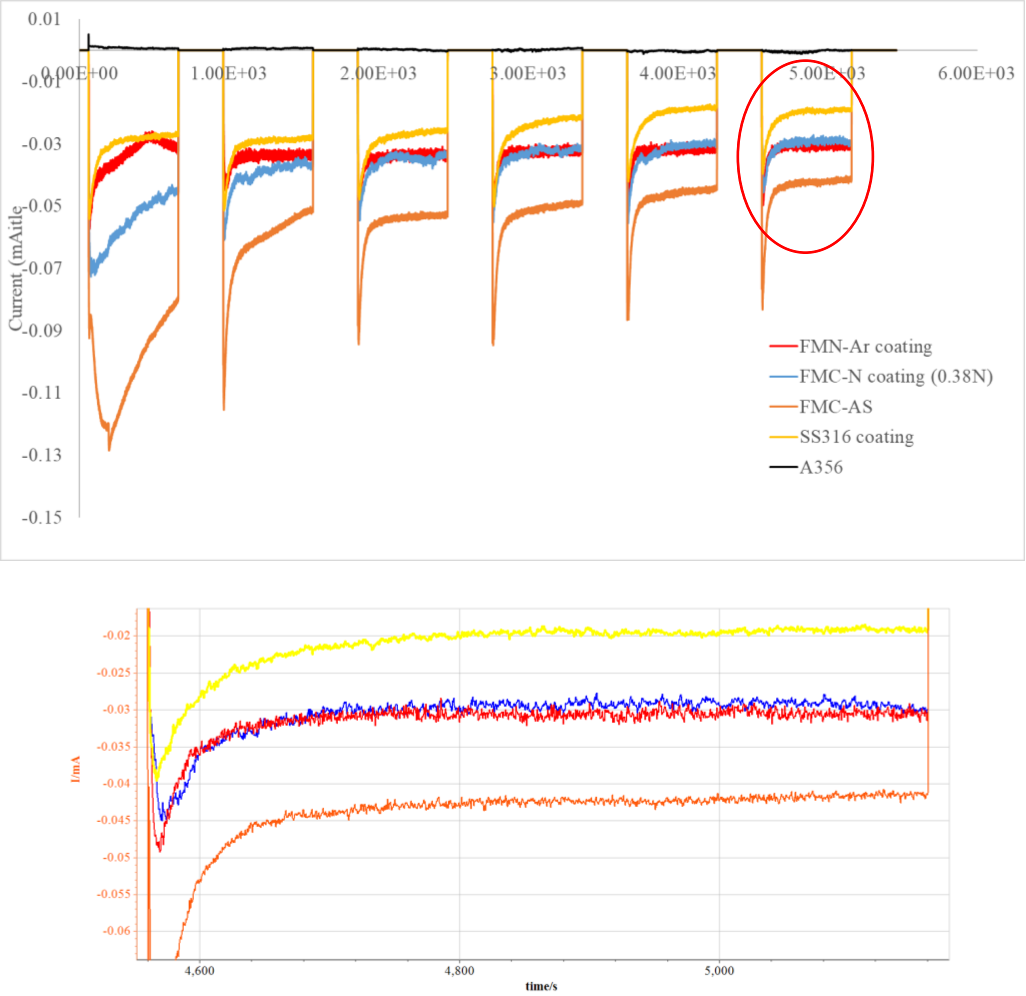

Fig 6.22 ZRA Profiles of Cold-Sprayed Coatings w.r.t A356 Coupons (6 Cycles)

Chapter 7 Optimization of Deposition Efficiency Using SS316

Paper 2: An attempt to understand powders for cold spray deposition

This chapter evaluates centrifugally atomized stainless steel 316 alloy powders for usability with cold gas dynamic deposition process. The evaluation was conducted by comparing the centrifugally atomized powder with conventional gas atomized stainless steel 316 powder in terms of powder properties as well as resultant cold sprayed coatings. This study included powder – size, shape, porosity, nano-hardness, grain orientation and coating – deposition efficiency, bond strength, micro hardness, corrosion, and wear properties. Powders produced with both techniques has similar size and shape. Thus, the effect of internal structure of the powder on cold spray deposit ability could be evaluated. A significantly higher deposition efficiency and bond strength was observed with gas atomization when compared to centrifugally atomized stainless-steel powders. Differences between the two powders is presented.

7.1 Deposition and Raw Materials

Commercially atomized powders from two reputed manufacturers were used in this study. To prevent readers from getting distracted from the results, the powder manufacturers are not disclosed.

The sample names in the article would be further abbreviated as G.A (Gas Atomized 316 powder and coating) and C.A (Centrifugal Atomized 316 powder and coating).

Table 7-1 represents the starting composition of the stainless powders used. A similar composition along with a similar particle distribution size (15-60µm) for both the powders was used. G.A and

CA powders had D10 value of 20 µm and 18.4 µm respectively; a D50 value of 31µm and 30.4 µm respectively and a D90 of 46.9 µm and 48.4 µm respectively.

Table 7-1 Composition of the SS Powders Used for Deposition

Composition	**Fe**	**Cr**	**Ni**	**Mn**	**C**	**Mo**	**Si**	**P**	**O**	**N**
G.A (Gas atomized)	Bal	17.02	11.59	0.43	0.008	2.39	0.5	0.04	.03	.01
C.A (Centrifugal atomized)	Bal	17	11.5	1.35	0.03	2.16	0.87	0.037	.04	.0588

To delineate the differences in deposition characteristics, coatings were sprayed on large aluminum 6061 plates (12”x12x”1/2”) to minimize the influence of target heating. The cold spray deposition parameters were kept identical for both types of powders as mentioned in Table 7-2. A convergent-divergent nozzle with a rectangular cross section was used in this study. The details of the nozzle and deposition parameter optimization can be found in our previous study [68]

Table 7-2 Deposition Parameters

Temperature (°C)	**Pressure (Mpa/psi)**	**Standoff (mm)**	**Carrier Gas (Mpa/psi)**	**Powder flow (g/min)**
600	3.447/500	10	0.47/68	20

7.2 Powder Precursor Characterization

The feedstock powders obtained from both C.A and G.A techniques were spherical. This is shown in the SEM micrographs of as received, and cross-section etched powder particles in Fig 7.1. The G.A powder showed many agglomerated satellites. The outer surface structure of G.A powder did not reveal complete structure. The cross-section shows that G.A powders had a near complete transition from the columnar dendrites to multi-crystalline anisotropic grains due to the cooling time during atomization, ranging from 5-10µm. The outer surface structure of C.A powder showed a cellular dendritic combination [71, 72].The cross section shows majority of the internal features of the C.A powder to be under 5µm. The differences in the solidification rates during atomization, leads to a different dendritic network in the powders.

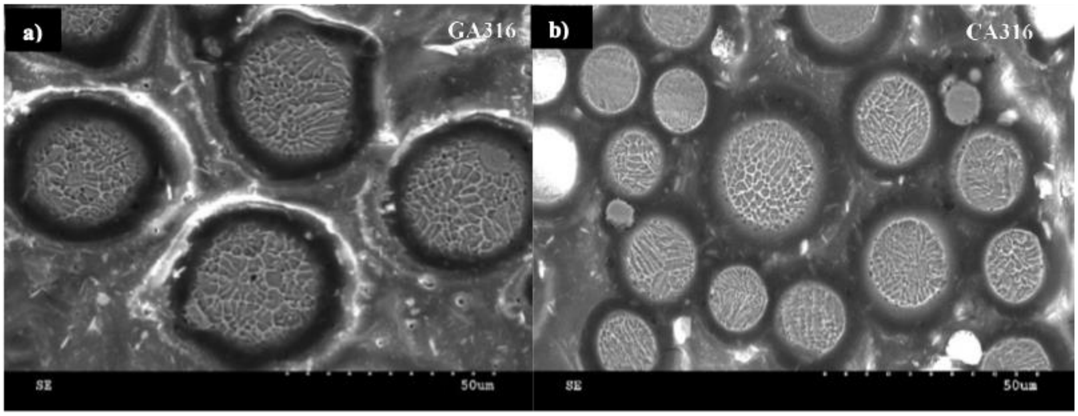

Fig 7.1 a), b) Etched Cross-Section of GA316 and CA316 Powders Respectively

A Microtrac Sync system was used to measure the particle size distribution and shape analysis using laser diffraction and dynamic image analysis respectively (Microtrac Retsch GmbH, Duesseldorf, Germany). A ZEISS Versa 620 X-ray Microscope was used to characterize the powder in 3D. The scan used a voltage of 140 kV and power of 21 W to image the powder prepared in glass capillary tubes. A pixel size of 0.75 µm was obtained with the 4x objective. The powder was segmented using commercially available software from Zeiss – Powder Analyzer. Visualization was completed in TXM3Dviewer, allowing for 2D cross-sections and 3D views to be obtained.

A snapshot of the morphology of the powder along with sphericity and roundness characteristics are shown in Fig 7.2. The statistics was calculated from well over 50,000 particles. There were a few irregular powders as visible in the snapshot but account for small fraction in both atomization techniques. The formula for sphericity is the ratio of minimum circumscribed and maximum inscribed circles and for the roundness is the ratio of area of the particle to the area of a circle with the same convex perimeter. While generally, the centrifugal powders exhibited higher sphericity and roundness, when segregated based on calculated particle diameters, both powders were identical below 35μm. Above this size, the centrifugal powder was more spherical and exhibited higher roundness.

Further insight into particle's internal porosity was obtained from micro-CT scan and are shown in Fig 7.3. The CA powder had a significantly lower fraction of fine pores with size of 15 microns or less and larger fraction of coarse pores compared to gas atomized powder. Correlating the pore sizes to particle diameters, it can be ascertained that beyond a certain particle diameter, approximately 30-60μm, the C.A powders exhibited slightly higher porosity compared to gas atomization.

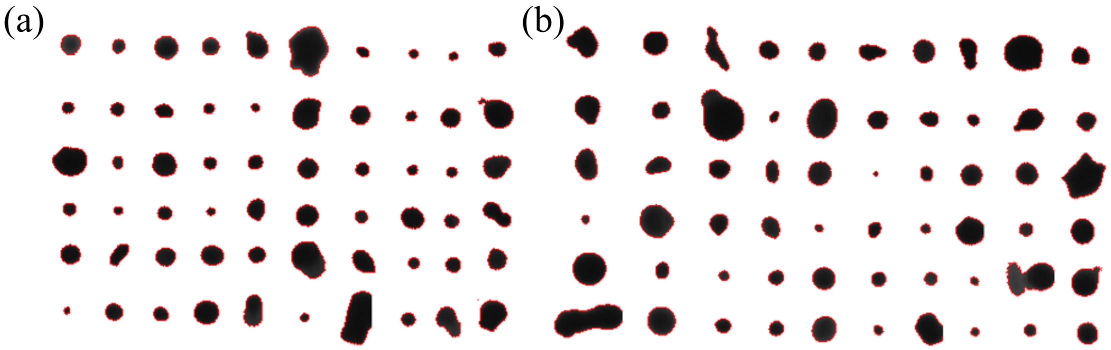

Fig 7.2 Snapshot of the Powder Particles From the Shape Analyzer a) G.A, b) C.A

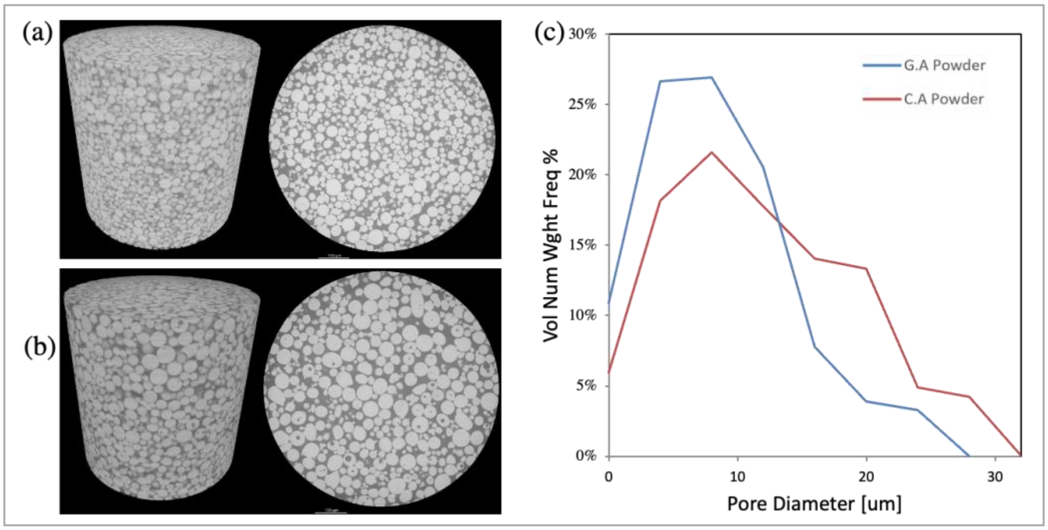

Fig 7.3 Micro-CT Scan Results Actual Scan Volume (a) G.A Powder (b) C.A Powder (c) Pore Size Distribution

Powder X-ray diffraction Fig 7.9 indicates a small presence of ferrite along with austenite in the as received stainless steel powders (G.A and C.A). From the diffraction pattern, the fraction of residual ferrite was higher in the C.A powder. This could be due to higher solidification rates that can be achieved in centrifugal atomization. Brewer et al. [73] have analyzed phase content within gas atomized stainless steel powders and have found powders with overall smaller size distribution particles had a higher fraction ferritic phase due to their higher solidification rate.

EBSD characterization of the powders in shown in Fig 7.5. About 10 -15 particles were analyzed from each of the atomization techniques. Fig 7.5 a, d shows typical IPF maps obtained from each of the powders, corresponding phase and IQ maps are shown in Fig 7.5b, c and Fig 7.5 e, f respectively. The phase maps clearly show that the ferrite content was present in smaller fragments of the powder and can be associated with higher solidification rates of the particle. The low angle grain boundaries (LAGB) <15deg and high angle grain boundaries (HAGB) are shown in blue/green and red, respectively. Overall mis-orientation angle and grain size distribution from different powders were extracted using OIM software. The grain boundary angle is superimposed on the IQ map.

The effect on grain structure due to differences in solidification kinetics achieved in gas and centrifugal techniques can be observed in terms of grain boundary angle and size distribution. From the obtained data set, we observed significantly lower fraction of grain boundaries < 5deg or sub grain boundaries with the centrifugally atomized powder. The absence of low angle grain boundaries could be due to higher solidification rates. Similar conclusion has been derived by other researchers [74]. Similar effect was found in the grain size distribution, while both atomization techniques produce grains of similar size, a lower solidification rate in the G.A powder appears to result in a combination of high fraction of LAGB leading to grain coarsening. While both powders had similar grain size of 1 to 6µm, some grain coarsening was present in the gas atomized powders. The G.A powders had at least one additional coarser grain significantly bigger in diameter with respect to the typical grain size present in the C.A powder.

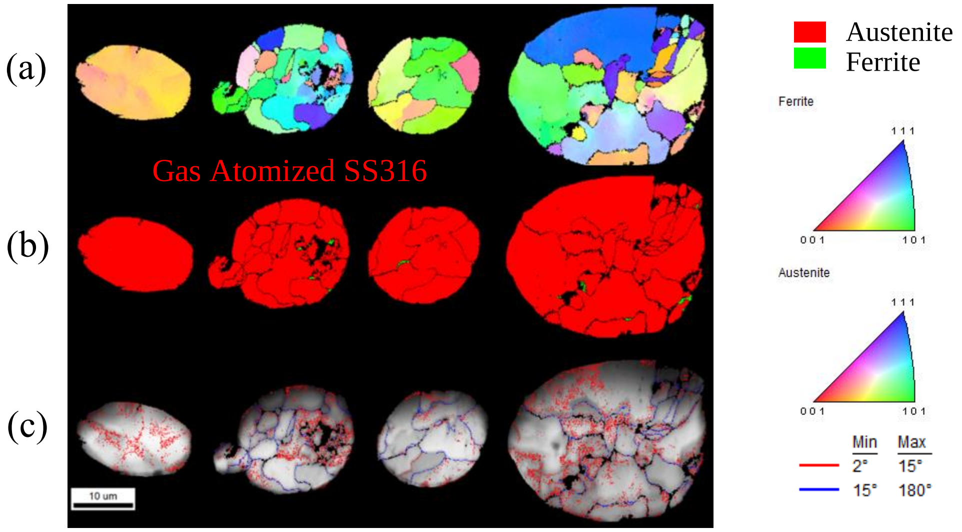

Fig 7.4 EBSD Data IPF (a) Phase Map (b) CI Map With Red (>2°,<15°) LAGB and Blue HAGB (>15°) Boundaries (c) for G.A Powder

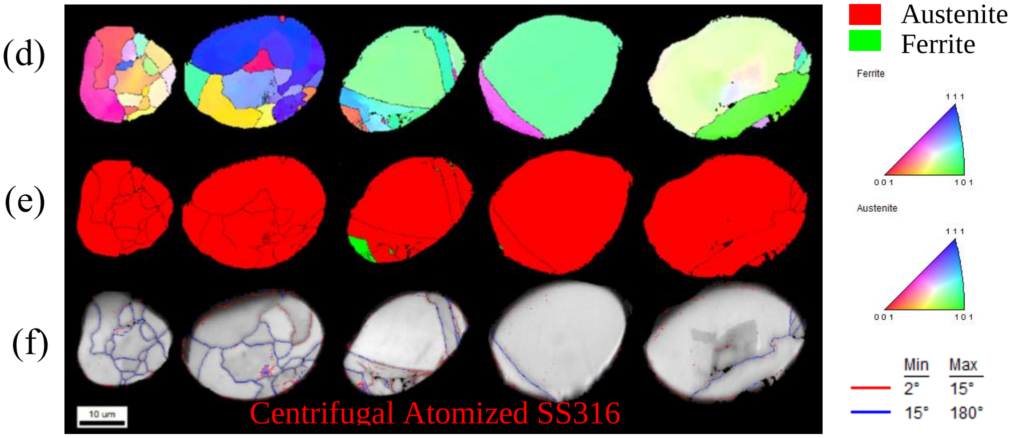

Fig 7.5 EBSD Data IPF (d) Phase Map I CI Map With Red (>2°,<15°) LAGB and Blue HAGB (>15°) Boundaries (f) for C.A Powder

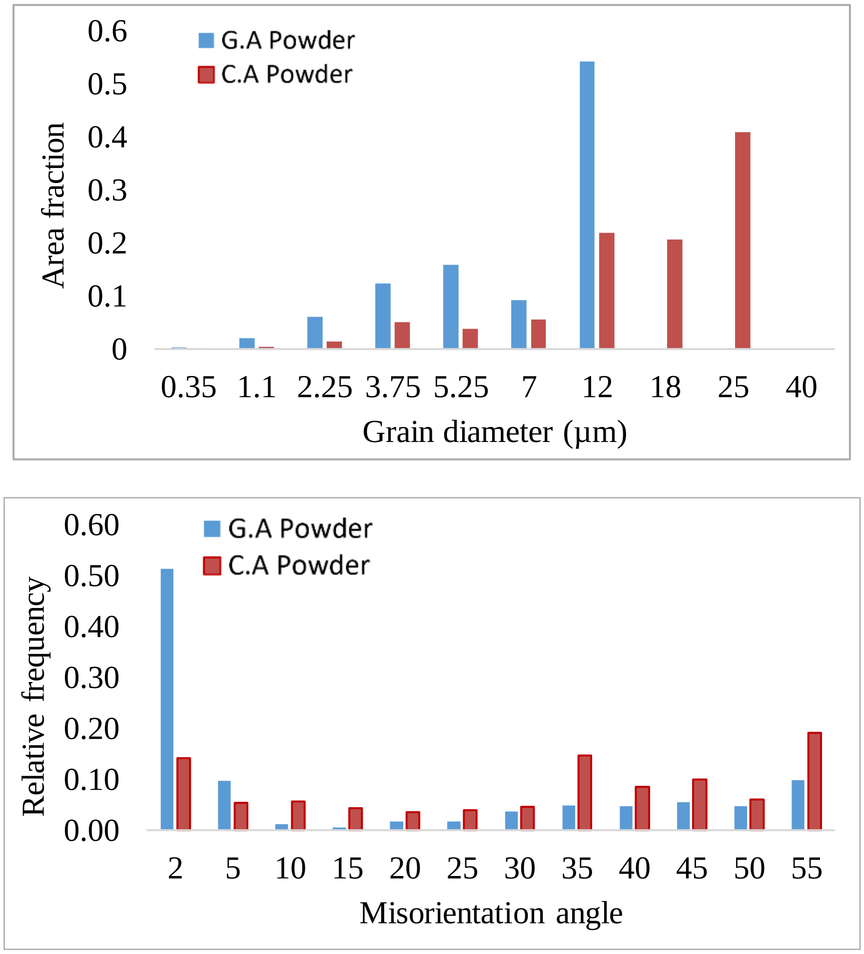

Fig 7.6 Grain Diameter and Misorientation Angles for GA and CA Precursors

Nano hardness was measured on the cross-section surface of both powder particles of similar size (30 µm). The nano-indentation curves are shown in Fig 7.7. This curve represents an average and 3sigma distribution in the loading section of the test. The C.A particles required a higher load for the given indenter displacement. An average hardness of 2.65 Gpa and 2.87 Gpa was recorded for G.A and C.A powders respectively. This higher hardness in the C.A powder could be due to the finer grain structure and higher fraction of HAGB observed with EBSD measurements. The difference in elastic modulus and hardness would also correspond to 2 different grains as studied by Roa et. al [75].

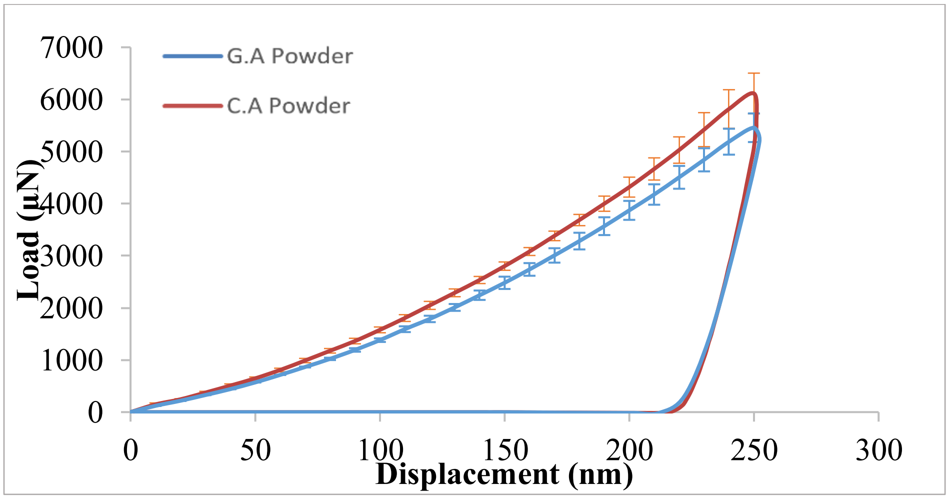

Fig 7.7 Nano-Indentation Plots of Both Steel Precursors

7.3 Coating Characterization

The deposition efficiency of C.A powder was significantly lower compared to G.A and required additional deposition layers to achieve the 1.3mm coating thickness. Table 7-3 represents the cold-sprayed deposition results. Cross-section images of both the coatings are presented in Fig 7.8. The arrow in the figures indicates the direction of particle travel during deposition. Inter-splat voids and boundaries were present in the coatings. It is typical in cold spray for a softer substrate to extrude around a harder particle [76]. Since a softer substrate (aluminum) was used, the initial layer of particle-substrate bonding occurs due to a phenomenon termed as surface-scrubbing. This results in extrusion of aluminum in between the particles which limits the hardness of the bottom layer [77]. Similar observation is present for the G.A coating. In comparison, its magnitude and occurrence are limited in the C.A coating.

Table 7-3 Deposition Results

Powder	**Layers to achieve** ~1.3mm coating thickness	**Deposition time**	**Deposition Efficiency (%)**	**Average Crystallite size (D) (nm)**
G.A	4	32mins 28sec	70.26±0.3	16.36
C.A	6	48mins 52sec	41.33±0.92	18.30

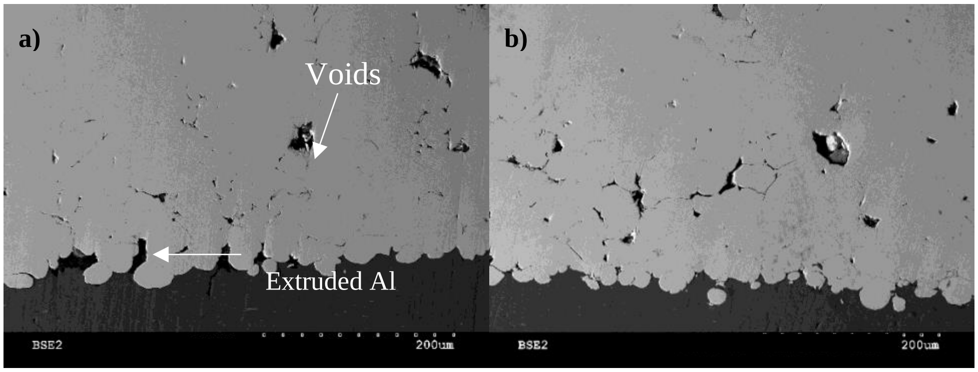

Fig 7.8 Cross-Section of Cold-Sprayed Coatings a) G.A b) C.A

Fig 7.9 shows the XRD of the powder and their respective coatings. A complete austenite phase was observed in both coatings. Peak shift and broadening are frequently observed in cold sprayed coatings [78].The shift occurs due to intensity of the residual stress which increases proportionately to the degree of cold work. The peak shift of ~0.8° is visible in the G.A coating and reveals higher degree of residual stress accumulated in the coating compared to the C.A coating. Significant peak broadening was observed in the FCC (γ) phases of both the coatings compared to the peaks of the precursors. It led to a change in the crystallite size compared to the precursor. A lattice parameter of ~0.41-0.42nm was calculated from the XRD patterns of both the powders and their respective coatings. Crystallite size reduced significantly from the precursor to its respective coating. The C.A powder had more crystallite size than G.A with a difference of ~0.1nm which reduced to ~0.02 nm in the respective coatings. The broadening and reduction in crystallite size for a coating corresponds to a non-uniform micro-strain which is a typical phenomenon observed in cold spray.

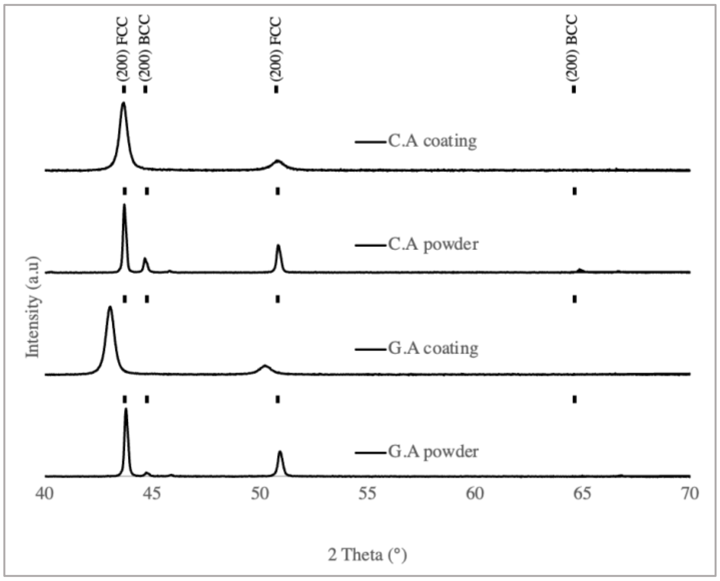

Fig 7.9 XRD Spectrum of As-Received Powders and Their Respective Coatings

Table 7-4 represents average results of the bond test. G.A coating showed higher bond strength than C.A coating. The location of bond failure is critical to understanding the bond quality of the coatings. The G.A coating experience adhesive failure of the FM1000 epoxy. For the C.A coating, cohesive failure occurred until at the initial layers of deposition. This shows that the bond strength for G.A coatings could be greater than 70Mpa and C.A coatings failed at 45 Mpa tensile strength. The lack of deformation or cold work in the C.A coating observed from the monotonic hardness levels resulted in poor mechanical anchoring reducing bond strength of the C.A coating significantly.

Table 7-4 Bond Strength of Coatings

	Bond strength (MPa)
G.A Coating	68.125 ± 1.10
C.A Coating	47.5 ± 0.76

Anodic polarization behavior for the coatings was analyzed as presented in Fig 7.10. Table 7-5represents a compiled result of the corrosion test. It can be seen from the slopes ßa and ßc that the corrosion behavior for both the stainless coatings were similar, the C.A coating had a nobler corrosion potential than G.A coating. Icorr values are indicative of the corrosion sensitivity/susceptibility of the metallic materials. Both C.A and G.A coatings had similar Icorr values depicting a similar corrosion behavior of the coatings [79]. Significant amount of passivation was observed in both the coatings due to the presence of chromium. A pitting corrosion which usually occurs in SS316L coatings was observed with Epit values close enough to Ecorr values [79]. The obtained values were aligned with the reference values by other researchers. The passivation transition for both G.A and C.A coatings explains that the coating thickness is beyond the minimum thickness to prevent the corrosion attack by interconnected porosity in the coating. This behavior also correlates to a near similar metallurgical composition of the coatings.

Table 7-5 Tafel Fit-SS316 Coating

Coating	**E_{corr} (mV)**	**I_{corr} (μA)**	**ßa**	**ßc**
G.A	-534.53	9.375	440.7	245.8
C.A	-483.514	9.456	438	253.2

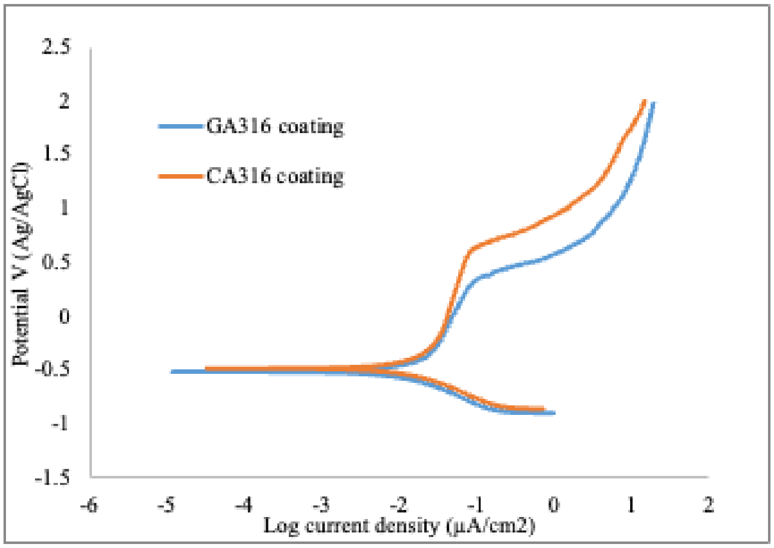

Fig 7.10 Polarization Curves for SS316 Coatings

7.4 Conclusions and Discussion

Under identical deposition conditions, the C.A powder resulted in lower deposition efficiency compared to coatings produced from G.A powder. The microhardness, bond, wear, and corrosion studies demonstrated that the extent of cold work and plastic deformation was inadequate in the C.A coating. This suggests that the C.A powder required a higher particle velocity to produce coatings comparable to that from the GA powder. Detailed results about wear, hardness and corrosion behavior of the coatings are elaborated in Paper 2.

The atomization techniques thus evidently have a significant impact on the deforming mechanisms for a cold sprayed coating despite a similar precursor composition. The C.A powders had a similar morphology, but significantly lesser deposition efficiency compared to G.A powders. The lack of bonding between C.A particles is evident from its lower bond-strength. EBSD and Nanoindentation measurements revealed some distinct differences in the precursors. This study also shows for the given powder nano-indentation serves a good technique for evaluation of properties to predict the cold-spray-ability of the material. Low deposition efficiency of the C.A powders require further validation in terms of other metals/alloys, consistency of the powder quality testing from other manufacturers and between lots.

Thus, the proposed high nitrogen steel composition can further be manufactured by gas atomization in-order to significantly improve the deposition efficiency for cold-spray. This will give rise to an extremely high value component in terms of optimum mechanical properties with an economically viable and efficient manufacturing process.

Chapter 8 Data-Model Development

8.1 Introduction

Machine learning and Artificial intelligence are a few of the niche emerging techniques. Industries have slowly begun deploying these two approaches in every possible way at the design, manufacturing as well as a logistic stage. Analyzing largely populated databases (bigdata) is one of the biggest tasks carried out in the industry since the beginning. However, the possibility of forecasting various outputs based on the available populated data has not been optimized for its accuracy. This heavily affects the decision making in the industry [80]. Prediction models are an approach to utilizing local data to help forecast the future needs or outputs with respect to current scenarios. These models known as prediction rules or prognostic models are successfully being deployed in the industry [81]. These models are being continuously optimized for their confidence levels and has been challenging for the data-analysts. This essentially has led to an extensive use of machine-learning based approach.

Additive Manufacturing and other 3D-printing techniques are currently facing lot of challenges in variability in the final product quality [82]. Few possible reasons for this variance can be pointed at anisotropy in the manufactured component, unoptimized process parameters etc. These are essentially limiting these techniques to be commercialized.

Feedback systems and data acquisition are very critical for all the AM techniques which can help the scientists re-iterate and optimize the results. These can help collect live-experimental data which can aid to understand the process in a better way and assess and optimize the variability

[83]. Neural Networks and other regression techniques have gained a high research interest due to their ability to predict and re-iterate the models.

8.1.1 Machine Learning Approaches used in AM/3D printing

Physics Based Simulation Approach:

Carrying out experiments to optimize any manufacturing process is not always possible due to the limitations of infra-structure and economics. Implementing changes in any process could be an expensive and a challenging task to any organization. Simulation approaches have thereby gained a lot of importance which allows easy visualization of the process performance. Software based simulations have aided researchers and engineers to easily troubleshoot, optimize and improve processes. Even though simulations are a widely accepted tool, they may demand a high computational power which in turn affects the economics as well. Making use of existing simulation data and machine learning to prepare models to predict output variables is thus now being practices in the industry.

Data-Driven Approach:

A variety of ML techniques can be used to monitor the process parameters. Typically, any manufacturing technique would not necessarily have a linear relationship or a direct correlation between the input and output variables [82]. Lu et al. [84] has successfully presented a non-linear relationship for the Directed Energy Deposition parameters. They used a back propagation neural network to improve the process.

Derived relationships were combined with a non-dominated, sorting, genetic algorithm to optimize process parameters. Additionally, they proposed using an unsupervised, machine learning approach - known as self-organizing maps - to further post-optimize the process.

Combined Approach:

Many a times, combining physics-based models and data-models to predict and optimize the parameters is also considered a good practice. This relatively provides a trade-off for the extensive use of computational power as well as extensive use of experimentations. Researchers in the L-PBF industry are successful in combining such approaches using machine learning [82].

8.2 Objective

Considering the variances in the cold spray process; utilization of data models can prove helpful for the further optimization. This study thus considers a Data-model based approach and a simulation-based approach to optimize the deposition process. Output parameters are defined in terms of microstructural porosity, deposition efficiency and maximum particle velocity. These parameters were chosen primarily as they affect the coating quality to a greater extent.

8.2.1 Research Approach

This piece of work focusses on using the data-model for parameter selection of the deposition process to yield a coating with optimized quality. The coating quality has been gauged in terms of Deposition efficiency, microstructure porosity and max particle velocity. SS316 powder has been used as a precursor for both Simulation based and experimental based models. The developed high nitrogen alloy has not been deployed for this concept due to its limited research availability.

Neural Networks, Multi-output regression and Decision trees were considered during the data-model. The output of each technique has been presented and discussed. All the codes were scripted using Python and coded using Jupyter notebook.

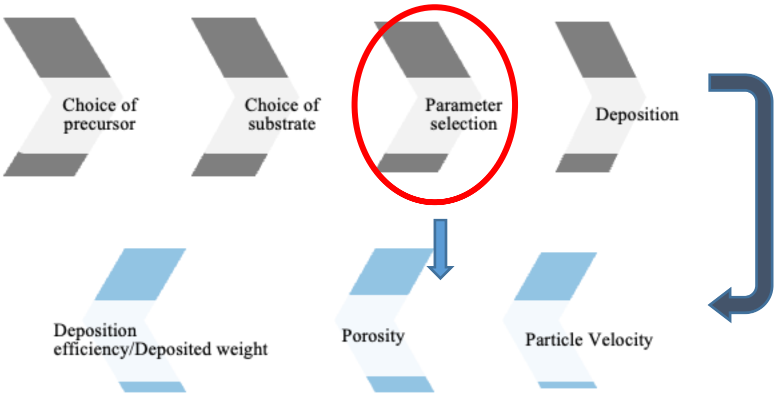

Fig 8.1 Variables Considered in Coating Development for Data Model

8.3 Methodology and Results

8.3.1 Simulation Approach

In this approach, maximum particle velocity was calculated at different standoff levels varying the input process parameters.

Fig 8.3 shows a few snippets of particle and gas velocity contours for certain parameters used in the data-training model. The contours represent the static velocity values at different levels of standoff distance between the nozzle and the substrate. While determining a specific value as the output parameter, a histogram was populated along the cross section of the nozzle for the particle velocities, and the maximum frequency value was chosen. The nozzle dimensions were used as mentioned in the work by Vikram et al. [68]. A total of 108 data points were used in this study. Table 8-1 shows a few sample datapoints used for the study. V0, V10, V20, V30 were the particle velocities populated at different standoff levels of 0mm,10mm,20mm,30mm respectively. A 3-level DOE was constructed.

Table 8-1 Sample Datapoints Used in Simulation Approach

Input				Output			
Powder feed g/min	**Gas Pressure (psi)**	**Gas Temp (°C)**	**Powder Temp (°C)**	**V0 m/s**	**V10 m/s**	**V20 m/s**	**V30 m/s**
6	500	600	0	694.80496	698.39273	654.36957	637.98379
6	500	600	600	651.19646	609.40599	659.45683	593.67429
6	500	600	250	609.41186	636.6604	567.63554	559.62923
6	500	400	0	636.14127	634.93027	601.00073	582.06122
6	500	400	600	592.93855	567.72489	562.13384	549.55982
6	500	400	250	543.62336	540.30202	521.92575	517.04652

Particle Velocity Contours and different Standoff planes

Parameters

Main gas: 500 psi
Powder flow: 6g/min
Main Gas/Powder inlet temperature: 600 °C,0°C

Main gas: 360 psi
Powder flow: 6g/min
Main Gas/Powder inlet temperature: 600 °C,0°C

Main gas: 250 psi
Powder flow: 6g/min
Main Gas/Powder inlet temperature: 600 °C,0°C

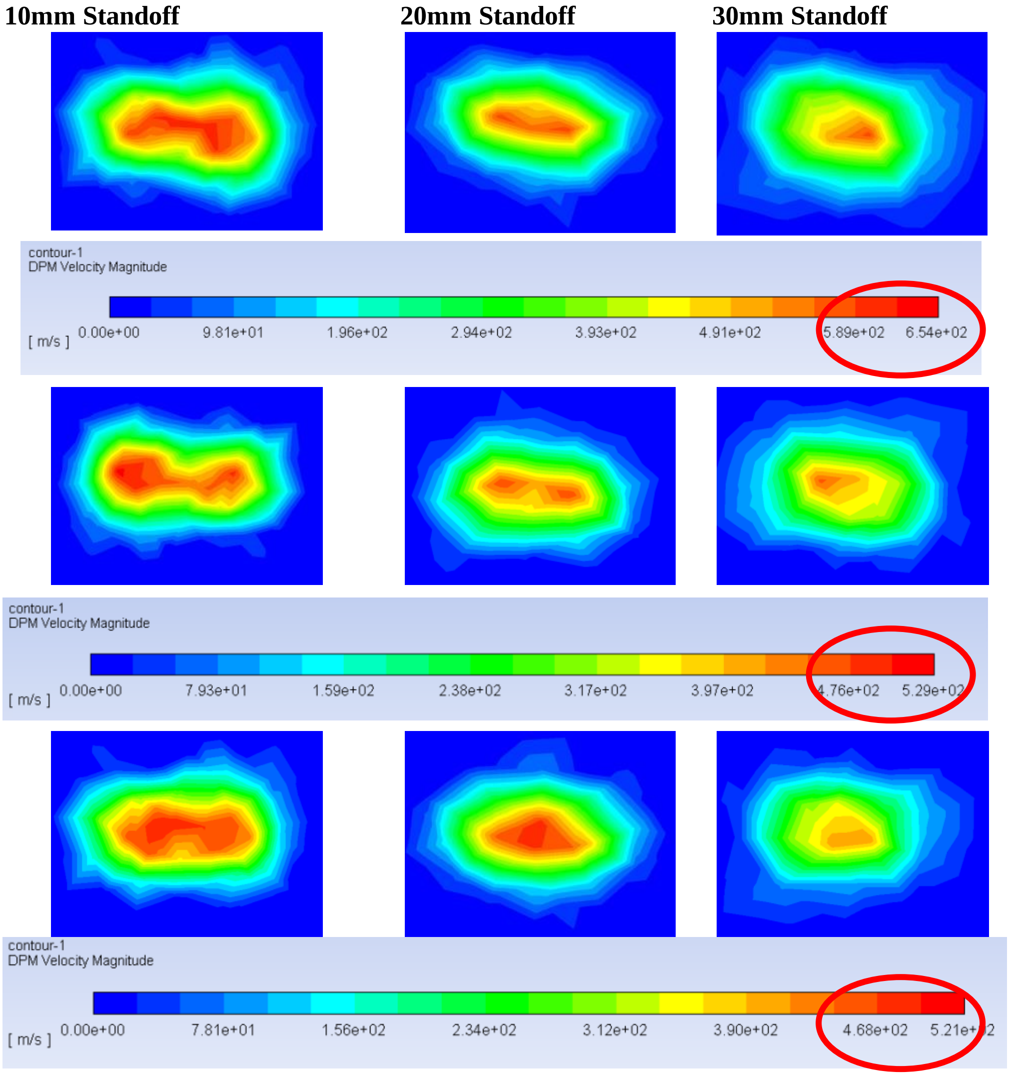

Fig 8.2 Particle Velocity Contour Snippets for Selected Parameter

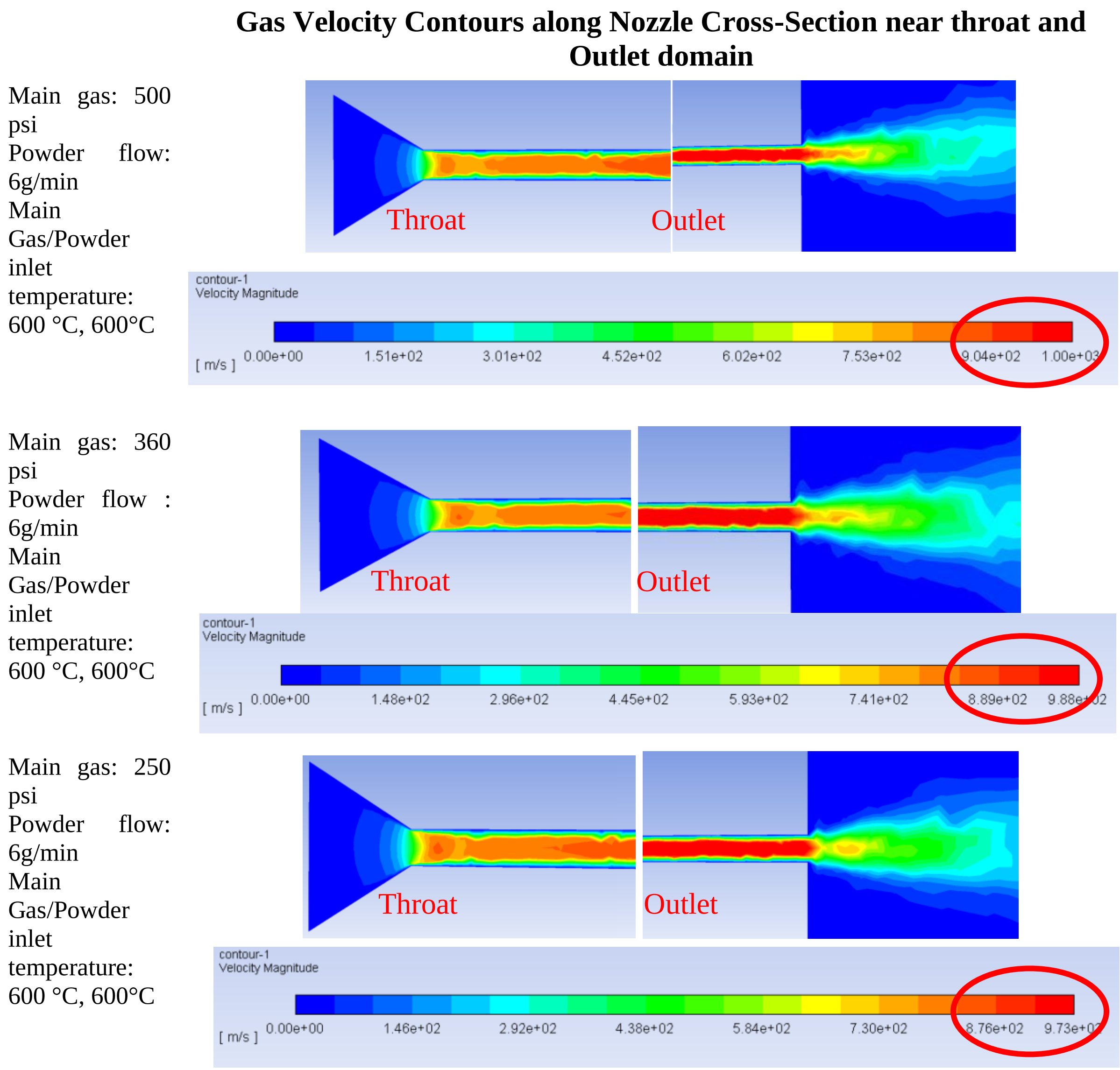

Fig 8.3 Gas Velocity Contour Snippets for Selected Parameter

Neural Network Approach:

A shallow neural network with 3 layers was constructed as presented in Fig 8.4. A total 42 parameters split as 10,12,10 for each layer were used. The input layer had 4 neurons while the output layer had 4 neurons. The input and hidden layer used a RELU activation while the output layer used a Linear activation. A batch size of 3 points was used with a total of 500 epochs for the training. Adam optimizer was used for achieving convergence in the error associated with MSE

(Mean Squared Error). These parameters and features were derived based on traditional design process for neural networks. The model was trained on 80% of the data points and tested on the remaining 20%. An average value of 5 computations was selected. Fig 8.5 displays the output from NN approach for standoff values of,10,20,30mm.

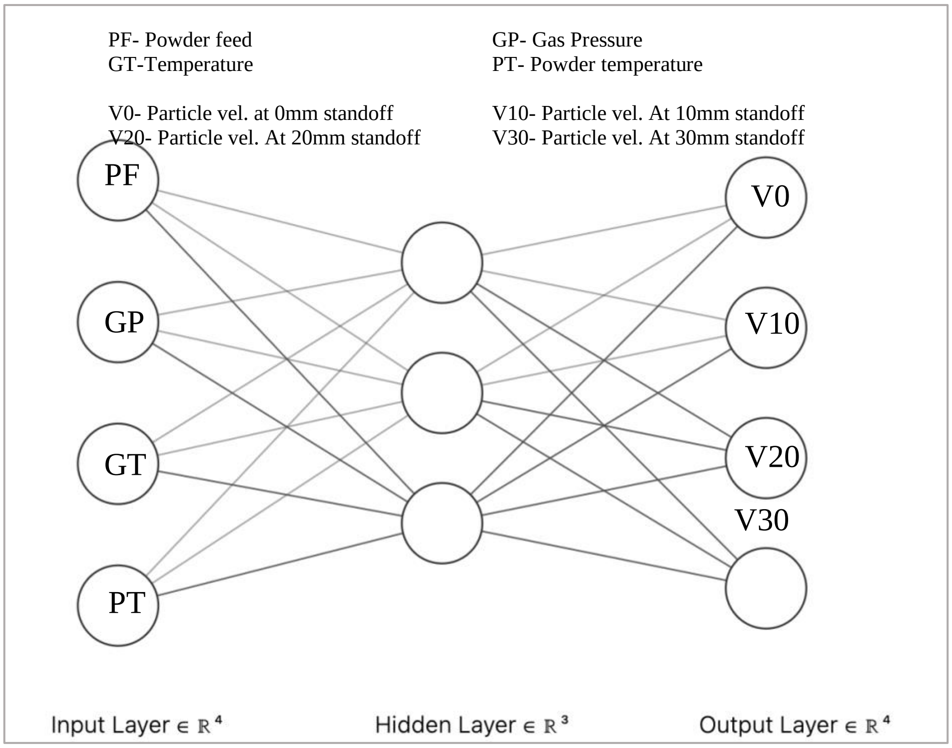

Fig 8.4 Constructed NN Layout

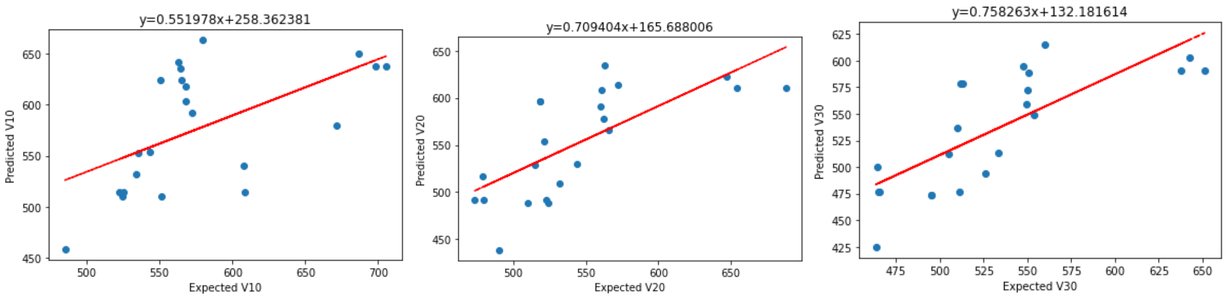

Fig 8.5 Scatter Plot of Expected and Predicted Particle Velocity at 10,20,30mm Standoff Using Neural Network

Regression Approach:

Fig 8.6 and Table 8-2 represent the output of the regression approach. An average r-squared value of 90% was reported for the regression. 80% of the datapoints were used for training while testing was done on the remaining 20%. The model was optimized for MSE with a regression score of about 95%.

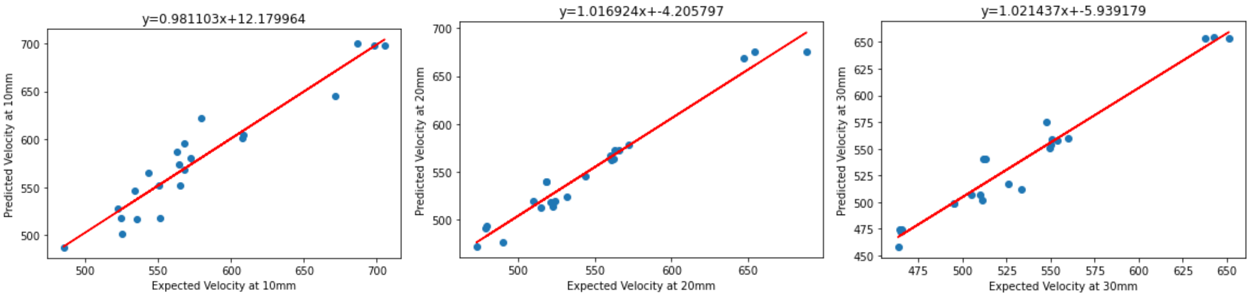

Fig 8.6 Scatter Plot of Expected and Predicted Particle Velocity at 10,20,30mm Standoff Using Regression

Table 8-2 R2 Values-Regression

	Velocity at 10mm	**Velocity at 20mm**	**Velocity at 30mm**
R-squared	0.9071	0.9543	0.9401

Decision Tree Approach:

Fig 8.7 and Table 8-3 represent the output of the decision-tree approach. An average r-squared value of 80% was reported. 80% of the datapoints were used for training while testing was done on the remaining 20%. The model was optimized for MSE with a regression score of about 80%

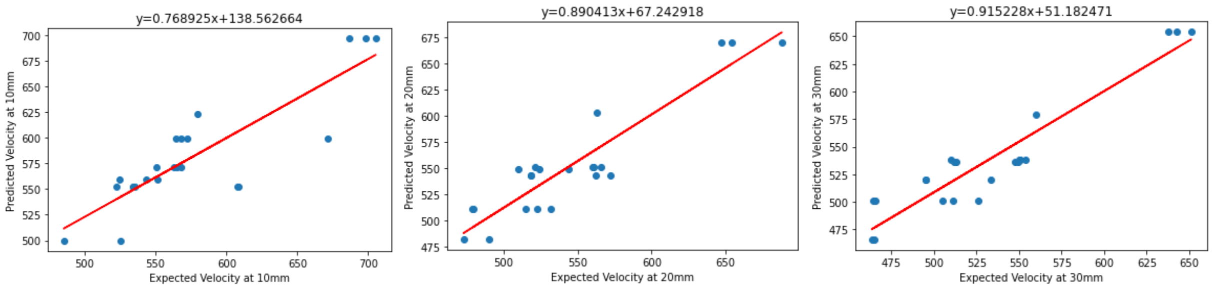

Fig 8.7 Scatter Plot of Expected and Predicted Particle Velocity at 10,20,30mm Standoff Using Decision Trees

Table 8-3 R2 Values-Decision Tree

	Velocity at 10mm	**Velocity at 20mm**	**Velocity at 30mm**
R-squared	0.7309	0.8281	0.8694

8.3.2 Experimental Approach

In this approach, cold-spray coatings were deposited using SS316 powder. Each experiment consisted of 1 sample and its replicate. A 2 level DOE was used for the input parameters to set-up the experiments. Output was determined as the deposited weight and its corresponding microstructural variability.

2D porosity was calculated at various positions within a 640 X 480-pixel SEM image. The measurement was done using image analysis software Image-j (Fiji) for a scale of 1pixels/micron. The porosity readings represent an average value of 10 images per experiment. Images with an area of 680µm X 480µm with a resolution of 640pixel X 480pixels were collected. A standard magnification 200x and a working distance of 15mm was maintained for all the SEM measurements. Standard image cleaning was carried out to measure an accurate area ratio with minimum threshold on every image.

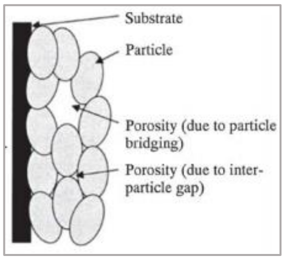

Fig 8.8 Porosity Representation in Cold Spray [85]

Researchers have established the use of image-j as a reliable source to measure porosity of cold-sprayed coatings [85, 86, 87, 88]. A variable porosity was also noticed in the replicates of the samples.

Table 8-4 Sample Dataset Used for Prediction (Experimental)

	Input					Output		
Sample ID (#)	**Gas pressure (psi)**	**Feed mm/s**	**Powder Feed (g/min)**	**Powder Preheat °C**	**Stand Off (mm)**	**Deposited Weight (gm)**	**Max Thickness (mm)**	**Porosity (%)**
1	500	10	150	600	10	3.56	2.13	1.415 **Fig 8.9
1.1	500	10	150	600	10	3.66	2.15	1.509
2	500	10	300	600	10	6.64	4.09	0.660
2.1	500	10	300	600	10	6.50	3.98	0.555
3	500	30	150	600	10	1.25	0.92	2.603
3.1	500	30	150	600	10	1.21	0.81	2.664
4	500	30	300	600	10	2.01	1.33	1.015
4.1	500	30	300	600	10	1.99	1.40	1.018
5	500	10	150	600	30	3.75	2.59	0.639
5.1	500	10	150	600	30	4.23	2.48	0.621
6	500	10	300	600	30	6.36	3.70	0.654
6.1	500	10	300	600	30	6.50	3.84	0.654

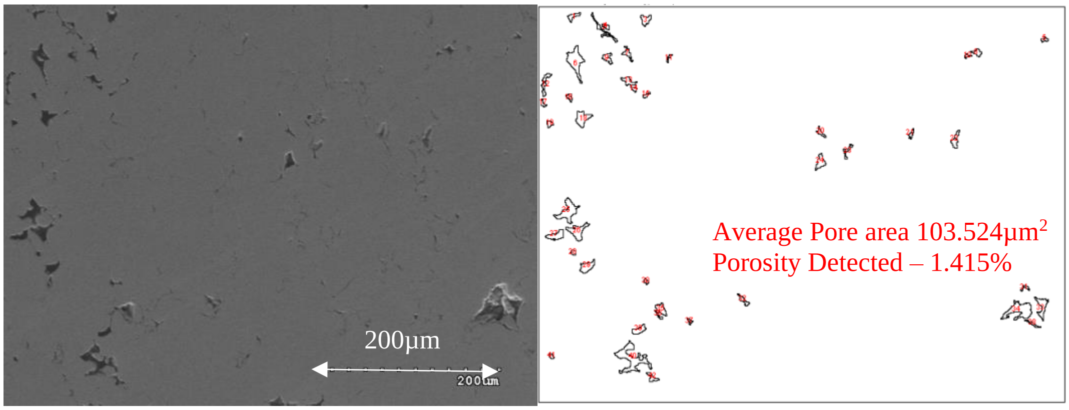

** This example represents the microstructure of Sample ID #1 (Average porosity- 1.438±0.34%)

Fig 8.9 Porosities Measured as Area Ratio a) SEM Image b) Translated Image for Pore Measurement

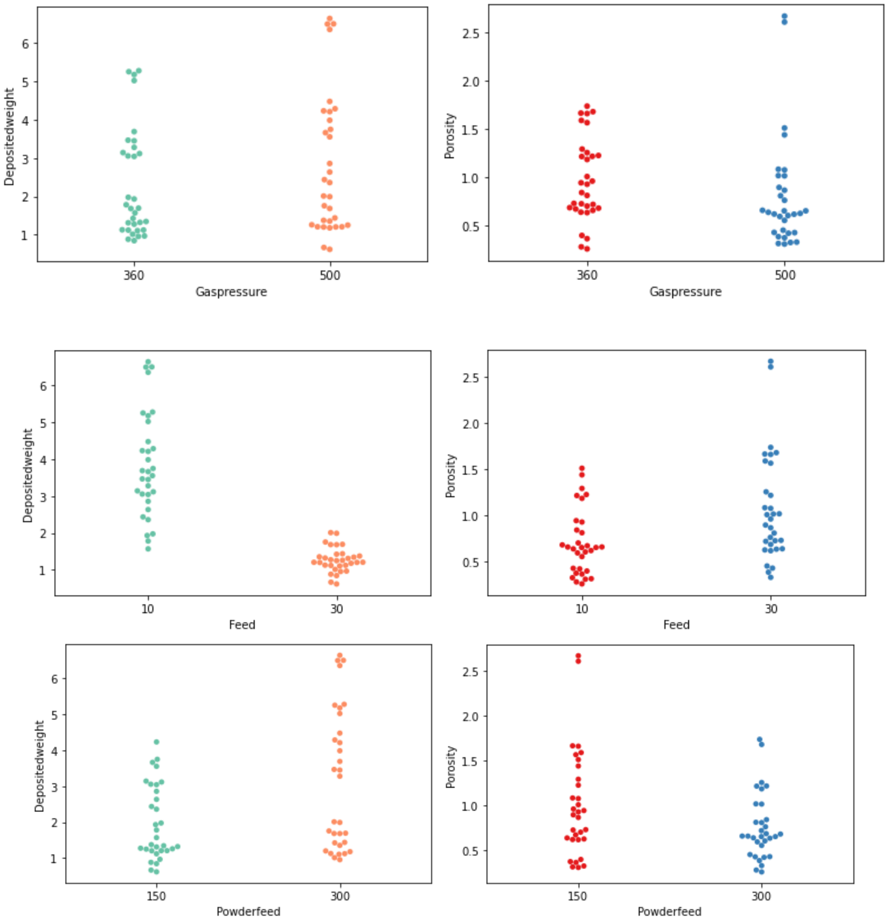

Fig 8.10 Pair Plots of Input Spray Variable Vs. Output Variables (Training Data)

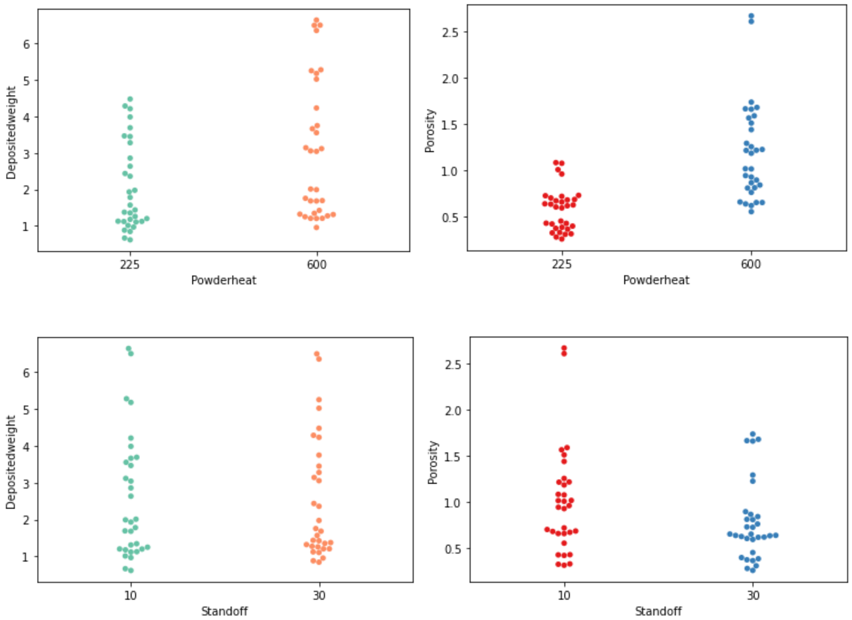

Fig 8.11 Pair Plots of Input Spray Variable Vs. Output Variables (Training Data) -contd.

Neural Network Approach:

A shallow neural network with 3 layers was constructed as presented in Fig 8.12. A total 29 parameters split as 12,9,8 for each layer were used. The input layer had 5 neurons while the output layer had 2 neurons. The input and hidden layer used a RELU activation while the output layer used a Linear activation. A batch size of 3 points was used with a total of 500 epochs for the training. Adam optimizer was used for achieving convergence in the error associated with MSE (Mean Squared Error). These parameters and features were derived based on traditional design process for neural networks. The model was trained on 80% of the data points and tested on the remaining 20%. An average value of 5 computations was selected. Fig 8.13 displays the output from NN approach for deposited weight and porosity prediction.

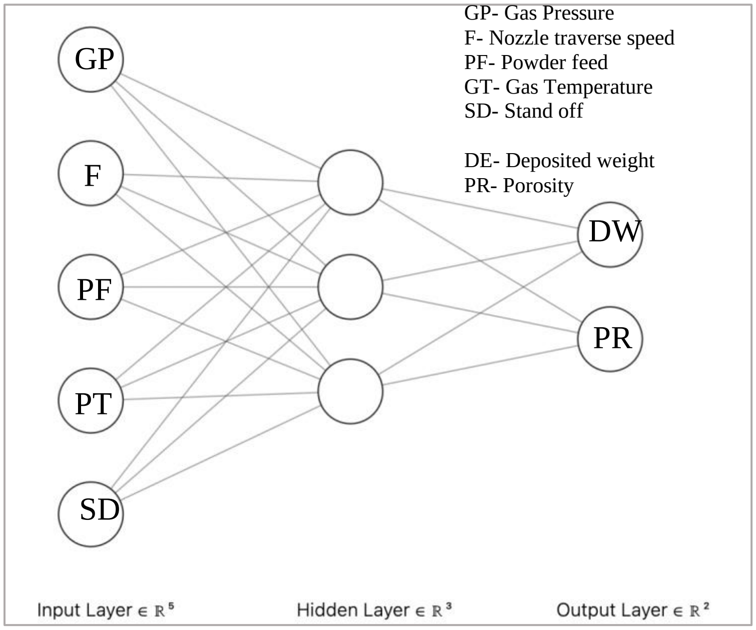

Fig 8.12 Constructed NN Layout

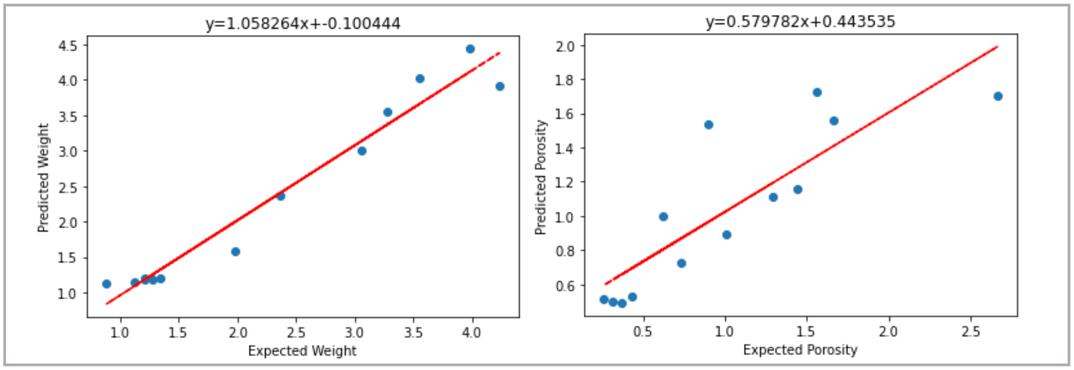

Fig 8.13 Scatter Plot of Expected and Predicted Deposition Weight and Microstructure Porosity Using Neural Network

Regression Approach:

Fig 8.14 and Table 8-5 represent the output of the regression approach. An average r-squared value of 80% was reported. 80% of the datapoints were used for training while testing was done on the remaining 20%. The model was optimized for MSE with a regression score of about 95%.

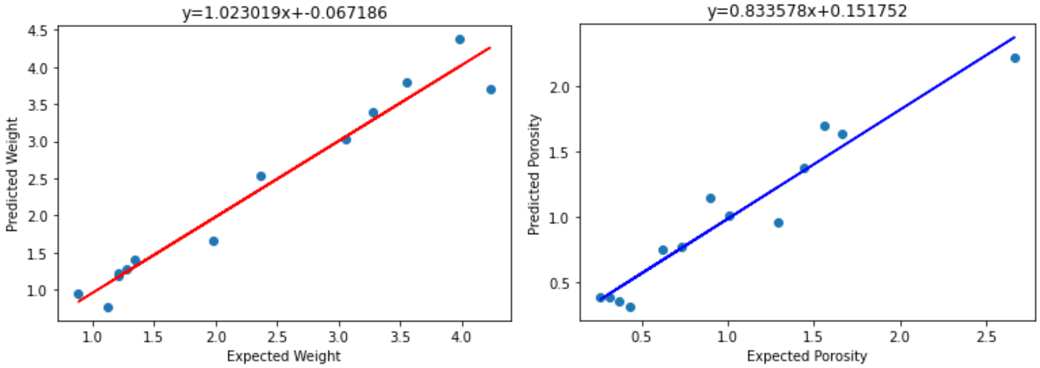

Fig 8.14 Scatter Plot of Expected and Predicted Deposition Weight and Microstructure Porosity Using Regression

Table 8-5 R-Squared Values-Regression

	Weight	**Porosity**
R-squared	0.956	0.921

Decision Tree Approach:

Fig 8.15 and Table 8-6 represent the output of the decision-tree approach. An average r-squared value of 80% was reported. 80% of the datapoints were used for training while testing was done on the remaining 20%. The model was optimized for MSE with a regression score of about 80%.

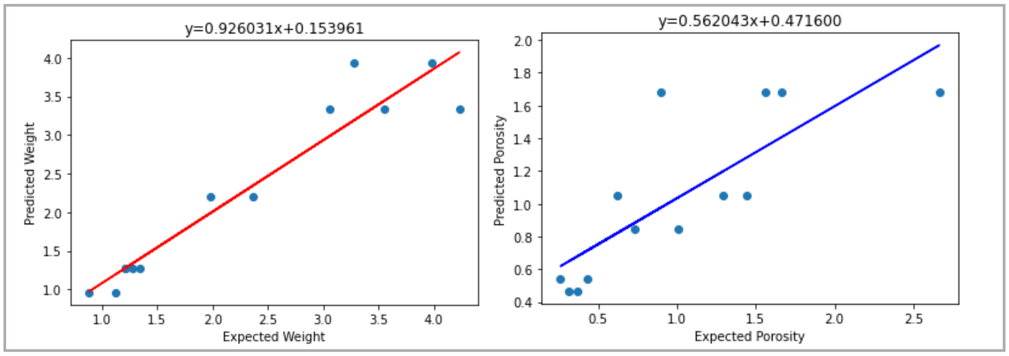

Fig 8.15 Scatter Plot of Expected and Predicted Deposition Weight and Microstructure Porosity Using Decision Tree

Table 8-6 R-Squared Values-Decision Tree

	Weight	**Porosity**
R-squared	0.916	0.626

8.4 Discussion

This work has thus demonstrated the ability of a prescriptive data-model to be used for process optimization in cold-spray technique. The prescribed data-model further optimization in-order to increase the prediction accuracy.

Decision-trees and multi-output regression led to near accurate prediction compared to the neural networks. An average r-squared value of 0.98 and 0.9 was reported for both the techniques. However, the Neural network prediction consisted of some outliers giving rise to a certain error in prediction. This prediction error could be further improvised by adding more training dataset. Overall, it was observed that the predicted values of porosity were less accurate than the weight prediction. This could be an account of inconsistent porosity along the cross-section. Since an average of 10 images was taken along the cross-section; few areas were observed to be dense, while few to be porous. Thus, a variability of porosity in a replicate i.e using same process parameters is possible. This could also be a result of the process parameters, which further demand fine-tuning.

Chapter 9 Conclusions and Suggestions

This work has thus presented a scalable treatment process to develop a high nitrogen powder using Fe-Mn-Cr composition simultaneously maintaining the nitrogen in dissolved form. A retreatment of existing HNS to improve its usability while dissolving the nitrogen in interstitial solid solution is also successfully presented. Functional coatings were prepared by solid state deposition which retain and represent the properties of the prepared precursors. Coatings with high corrosion resistance, high hardness and wear resistance were successfully developed. This delineates the usability of SS316 which uses alloying elements like Nickel and Molybdenum to promote corrosion resistance. A few optimizations and validations of the process and materials would ensure its commercial presence.

This developed material with a high nitrogen content would be a right candidate for applications which demand a high contact wear and corrosion resistance. Automotive industries can see this as a potential of using a lightweight substrate to coat with a protective layer of the nitrogen powder and deploy it in the parts of a vehicle. Automotive manufacturers like Porsche are involved in considerate amount of research in switching to light-weight components. However, there are limitations in terms of wear and softness. The proposed material could possibly be used as a protective coating on these components providing the necessary wear, corrosion resistance and strength. Due to absence of nickel there’s also a high potential of this material to be used in the bio-medical industry where corrosive resistance is an essential pre-requisite.

However, there are a few considerations which need to be addressed.

9.1 Implementations and Suggestions for Future Work

1. Microstructural validation of Nitride precipitates

This study extensively utilizes EBSD measurements to evaluate the presence of nitrides in the prepared powders. EBSD has been widely proven to be a good medium for detection of nitrides. However, the cold-sprayed coatings were not validated for nitride presence. A TEM study on the coatings would further give a clear information about the dissolved nitrogen in the powder as well as the coatings. Since cold-spray is a solid-state deposition technique with no metallurgical transformations, it is valid to claim that the nitrogen present in dissolved form would be present in the coatings without reoccurrence of Cr_2Nprecipitation.

2. Improvement of deposition efficiency of HNS using gas-atomization

Gas atomized powders for cold spray have been proven to show a maximum deposition efficiency [89]. Our work as mentioned in Chapter 7 also concludes a higher deposition efficiency for gas-atomized powders compared to centrifugal atomized. Thus, if the proposed composition is developed by gas-atomization technique, the cold sprayed coatings would have a higher deposition efficiency which would further increase the throughput of the process.

3. System design for batch powder treatment

Taking the findings of this study to a commercialized level; a system design for a larger batch size should be considered. This study involved powder treatment of 10/50g per batch with a stagnant style treatment. A continuous treatment could be further developed which would aid in batch production.

4. Homogeneity of Nitrogen in the alloy

A stagnant style powder treatment was used in this study. This led to agglomeration of powder particles which were further subjected to a milling process. Avoiding this agglomeration could further increase the cooling characteristics of individual particles because of more exposed surface area. This would further lead to a homogenous dissolution of nitrogen throughout the treated powder. A fluidized bed can essentially aid in development of an agglomerated free powder. This will also homogenize the nitrogen uptake due to high surface area exposed of individual particle.

5. Effect of various friction materials on the coatings.

In this study pin on disk friction was studied w.r.t WC (tungsten carbide) as a friction material. Friction materials like sintered metallic, stainless steel could have a different effect of friction which needs to be analyzed. A high temperature friction study is also recommended.

6. Improvement and optimization of deposition efficiency with cold spray

The HNS alloy developed in this study has a very high micro-hardness (HV0.3→~400). Plastic deformation of harder alloys is limited. This significantly affects the deposition efficiency due to lack of cold work of the particles on the substrate leading to a lesser deposition. An external heat source such as laser or an induction coil can be deployed to aid in localized heating which would soften the particles for better deposition. LACS (Laser assisted cold spray) is a widely accepted method of using an external laser beam to locally soften the powder particles for a better adhesion. Previous research has shown for LACS components to improve the deposition efficiency, local porosity and increase the bond-strength of the coating.

7. A combined approach of simulations and data-driven model using the developed high nitrogen alloy

The current prescribed model uses 2 separate approaches to predict simulation and experimental data individually using SS316 precursor. However, if both the approaches are combined using the developed High nitrogen precursor, it would make the process more robust, and the variability will be traced easily. Computational power also influences high cost to the industry for conducting accurate simulations which involve

8. In-situ integration of data model

Live feedback from the process would essentially increase the traceability of variance in the process. Thus, introducing and implementing sensors to measure parameters like powder particle velocity in the process would aid in collecting live process data(in-situ) which will further make the model more robust.

9.2 Appended Publications

1. N. S Karmarkar, V. Varadaraajan, P. S. Mohanty, S. Nagendiran, “A novel high nitrogen steel powder designed for minimized Cr_2N precipitations”, *Metallurgical and Material Transactions B*, under review.

2. N. S Karmarkar, V. Varadaraajan, P. S. Mohanty, C. Frederick, P. Bhattad, “An attempt to understand powders for cold spray deposition”, *Surface and Coatings Technology*, under review.

3. N. S Karmarkar, A. C. Jadhav, R. Viswesvaran, P. S. Mohanty, “Retention of dissolved high nitrogen content in coatings at atmosphere”, *In Manuscript.*

9.3 Other Publications/Conferences

1. Y. Chang, P.S. Mohanty, N. Karmarkar, M. T. Khan, Y. Wang, J. Wang,“Microstructure and properties of Cu–Cr coatings deposited by cold spraying”,*Vacuum*, Vol. 171,2020

2. N. Karmarkar, A. Koneru, P. S. Mohanty, Y. Wang, “Evaluation of cold-sprayed Cu-Cr coatings for vacuum switching applications”,*International Materials, Applications, & Technologies Conference and Exhibition*, St. Louis, MO USA,2021

3. A. Koneru, N. Karmarkar, P. S. Mohanty “Evaluation of vacuum breakdown characteristics of cold sprayed Cu-Cr Coatings”, *In Manuscript.*

References

[1] W. D. Callister and D. G. Rethwisch, Materials Science and Engineering-An Introduction, Wiley, 2013.

[2] Markets and markets, "Flat Steel Market by Process (Basic Oxygen Furnace, Electric Arc Furnace), Type (Sheets & Strips, Plates), End-Use Sector (Building & Infrastructure, Mechanical Equipment, Automotive & Other Transport), Region - Global Forecast to 2024," Markets and markets, Northbrook,Illinois, 2020.

[3] N. H. Pettersson, *Precipitation in Advanced Stainless Steels (Thesis),* Sweden: KTH Royal Institute of Technology, 2018.

[4] V. Gavriljuk and H. Berns, High Nitrogen Steels-Structure, Properties, Manufacture, Applications, Berlin,Heidelberg: Springer, 1999, pp. 1-71.

[5] J. S. Dunning, J. W. Simmons and J. C. Rawers, "Advanced Processing Technology for High-Nitrogen Steels," *The Journal of The Minerals, Metals & Materials Society (TMS),* vol. 46, pp. 40-42, 1994.

[6] Q. Wang, Y. Ren, C. Yao, K. Yang and R. Misra, "Residual Ferrite and Relationship Between Composition and Microstructure in High-Nitrogen Austenitic Stainless Steels," *Metallurgical and Materials Transactions A,* vol. 46, pp. 5537-5545, 2015.

[7] Y. N. Petrov, "Defects and diffusionless transformation in steel," *Naukova dumka, Kiev,,* p. 45, 1978.

[8] K. Irvine, T. Gladman and F. Pickering, "The strength of austenitic stainless steels," *The Journal of the Iron and Steel Institute,* vol. 207, pp. 1017-1028, 1969.

[9] H. Tsuge, Y. Tarutani and T. Kudo, "The Effect of Nitrogen on the Localized Corrosion Resistance of Duplex Stainless Steel Simulated Weldments," *Corrosion,* vol. 44, no. 5, pp. 305-314, 1988.

[10] H. Okamoto, "The effect of tungsten and molybdenum on the performance of super duplex stainless steels," *Proc. Application of Stainless Steels,* vol. 1, pp. 360-369, 1992.

[11] M.O.Spiedel, "Properties and Applications of High Nitrogen Steels," *High Nitrogen Steels--HNS 88,* pp. 92-96, 1989.

[12] G.Stein and I. Hucklenbroich, "Manufacturing and Applications of High Nitrogen Steels," *Materials and Manufacturing Processes,* vol. 19, no. 1, pp. 7-17, 2004.

[13] Schumacher.Patent USP 4039356, August 1977.

[14] Y. Tanaka, "Production of creep-resistant steels for turbines," in *Creep-Resistant Steels*, Woodhead Publishing, 2008, pp. 174-214.

[15] A.D.Patel, J. Hecht, J. Magee, R. Smith, G. Maurer and B. Friedrich, "On nitrogen pick-up during pressure-ESR of austenitic steels," in *TMS Annual Meeting*, Santa Fe/New Mexico/USA, 2009.

[16] J. C. Rawers, D. Govier and R. Doan, "Nitrogen addition to iron powder by mechanical alloying," *Materials Science and Engineering: A,* vol. 220, no. 1-2, pp. 162-167, 1996.

[17] H. Wriedt, N. Gokcen and R. Nafziger, "The Fe-N (Iron-Nitrogen) System," *Bull. Alloy Phase Diagrams,* vol. 8, no. 4, pp. 355-377, 1987.

[18] P. S. Mohanty, R. Visveswaran and V. Varadraajan, "Articles with nitrogen alloy protective layer and methods of making same". USA Patent US20200407830A1, 27 February 2019.

[19] P. S. Mohanty, V. Varadaraajan and S. Nagendiran, "High Nitrogen Steel Powder And Methods of making the same". USA Patent WO/2020/176616, 03 March 2020.

[20] M. A. Gharavi, G. Greczynski, F. Eriksson, J. Lu, B. Balke, D. Fournier, A. l. Febvrier, C. Pallier and P. Eklund, "Synthesis and characterization of single-phase epitaxial Cr2N thin films by reactive magnetron sputtering," *Journal of Material Science,* vol. 54, pp. 1434-1442, 2019.

[21] J. Simmons, D. Atteridge and J. Rawers, "Sensitization of High-Nitrogen Austenitic Stainless Steels by Dichromium Nitride Precipitation".

[22] J. W. Simmons, "Overview: high-nitrogen alloying of stainless steels," *Materials Science and Engineering: A*, vol. 207, no. 2, pp. 159-169, 1996.

[23] R.Sanjinés, P.Hones and F.Lévy, "Hexagonal nitride coatings: electronic and mechanical properties of V2N, Cr2N and δ-MoN," *Thin Solid Films,* vol. 332, no. 1-2, pp. 225-229, 1998.

[24] N. Pettersson, K. Frisk and R. Fluch, "Experimental and computational study of nitride precipitation in a CrMnN austenitic stainless steel," *Materials Science and Engineering: A,* vol. 684, pp. 435-441, 2017.

[25] E. U. Lee and R. Taylor, "High Nitrogen Stainless Steel," Department of Navy, Maryland, 2011.

[26] T. E. Gammal, R. Abdel-Karim, M. T. Walter, E. Wosch and S. Feldhaus, "High Nitrogen Steel Powderfor the Production of Near Net Shape Parts," *ISIJ International,* vol. 36, no. 7, pp. 915-921, 1996.

[27] F. Shi, Y. Qi and C. Liu, "Effects of Mo on the Precipitation Behaviors in High-Nitrogen Austenitic Stainless Steels," *Journal of Materials Science & Technology,* vol. 27, no. 12, pp. 1125-1130, 2011.

[28] F. Shi, L. Wang, W. Cui and C. Liu, "Precipitation behavior of M2N in a high-nitrogen austenitic stainless steel during isothermal aging," *Acta Metallurgica Sinica (English Letters),* vol. 20, no. 2, pp. 95-101, 2007.

[29] G. Stein and I. Hucklenbroich, "Manufacturing and Applications of High Nitrogen Steels," *Materials and Manufacturing Processes,* vol. 19, no. 1, pp. 7-17, 2004.

[30] P. A. Carvalho, I. F. Machado, G. Solorzano and A. F. Padilha, "On Cr2N precipitation mechanisms in high nitrogen austenite," *Philosophical Magazine, Taylor & Francis,* vol. 88, no. 02, pp. 229-242, 2008.

[31] N. H. Pettersson, D. Lindell, F. Lindberg and A. Borgenstam, "Formation of Chromium Nitride and Intragranular Austenite in a Super Duplex Stainless Steel," *Metallurgical and Materials Transactions A,* vol. 50A, pp. 5594-5601, 2019.

[32] C. Ornek and D. L. Engelberg, "Correlative EBSD and SKPFM characterisation of microstructure development to assist determination of corrosion propensity in grade 2205 duplex stainless steel".

[33] I. A. Yakubtsov, A. Ariapour and D. D. Perovic, "Effect of nitrogen on stacking fault energy of f.c.c. iron-based alloys," *Acta Materialia,* vol. 47, no. 4, pp. 1271-1279, 1999.

[34] FIZ Karlsruhe GmbH, "ICSD Database".

[35] A. Weddeling, K. Lefor, E. Hryha, S. Huth, L. Nyborg, S. Weber and W. Theisen, "Nitrogen uptake of nickel free austeniticstainless steel powder during heattreatment—an XPS study," *Surface and Interface Analysis,* vol. 47, pp. 413-422, 2015.

[36] N. Nakamura and S. Takaki, "Structural Control of Stainless Steel by Nitrogen Absorption in Solid State," *ISIJ International,* vol. 36, no. 7, pp. 922-926, 1996.

[37] JEOL, "JEOL SEM & TEM Posters," [Online]. Available: https://www.jeolusa.com/RESOURCES/JEOL-Posters/lc/47251/lcv/s/jeoledsperiodictable.

[38] S. Gates-Rector and T. Blanton, "The Powder Diffraction File: A Quality Materials Characterization Database," *Powder Diffraction,* vol. 34, no. 4, pp. 352-360, 2019.

[39] Element Materials Technology, "Element Materials Technology," [Online]. Available: https://www.element.com/.

[40] LECO, "Leco-736 Series Inert Gas Fusion," LECO, [Online]. Available: https://www.leco.com/product/736-series.

[41] B. C. Sousa, M. A. Gleason, B. Haddad, V. K. Champagne, A. T. Nardi and D. L. Cole, "Nanomechanical Characterization for Cold Spray: From Feedstock to Consolidated Material Properties," *Metals,* vol. 10, no. 1995, 2020.

[42] ASTM, *ASTM B117-Standard Practice for Operating Salt Spray (Fog) Apparatus,* West Conshohocken: ASTM International, 2019.

[43] B. Mike, C. Wall, S. Metzke, G. Clavel, M. Fichtner and C. Giordano, "A simple synthesis of MnN0.43@C nanocomposite: characterization and application as battery material," *Journal of Nanoparticle Research,* vol. 16, 2014.

[44] M. G. Heidlage, E. A. Kezar, K. C. Snow and P. H. Pfromm, "Thermochemical Synthesis of Ammonia and Syngas from Natural Gas at Atmospheric Pressure," *ndustrial & Engineering Chemistry Research,* vol. 56, no. 47, pp. 14014-14024, 2017.

[45] P.-Z. SI, J. Wei, W. Hia-Xia, Z. Min, G. Hong-Liang, C. Chul-Jin and L. Jung-Goo, "The High Nitrogen Pressure Synthesis of Manganese Nitride," *Chinese Physics Letters,* vol. 29, no. 12, 2012.

[46] T. Glück, "Mechanisms of nitriding electrolytic manganese metal," *The Chemical Engineering Journal,* vol. 54, pp. 167-173, 1994.

[47] M. D. Lyutaya and A. B. Goncharuk, "Manganese nitrides," *Soviet Powder Metallurgy and Metal Ceramics volume,* vol. 16, pp. 208-212, 1977.

[48] DM3D techology, "www.pomgroup.com," DM3D technology. [Online].

[49] V. G. Gavriljuk, "Nitrogen in lron and Steel," *ISIJ International,* vol. 36, no. 7, pp. 738-745, 1996.

[50] Ervin Industries Inc., "Ervin Technologies," Ervin Industries Inc., 2020. [Online]. Available: https://ervinindustries.com/ervin-technologies/centrifugal-atomization-technology.

[51] P. Behjati, A. Kermanpur, A. Najafizadeh, H. S. Baghbadorani, L. P. Karjalainen, J.G.Jung and Y.K.Lee, "Effect of Nitrogen Content on Grain Refinement and Mechanical Properties

of a Reversion-Treated Ni-Free 18Cr-12Mn Austenitic Stainless Steel," *Metallurgical and Materials Transactions A,* 2014.

[52] L. Ma, C. Zhou, X. Chen, Y. Hong, J. Zheng and L. Zhang, "Effect of nitrogen on nanomechanical behavior of austenitic stainless steel investigated by nanoindentation," *Materials Research Express*, vol. 5, no. 9, 2018.

[53] P. Jakupi, P. Keech, I. Barker, S. Ramamurthy, R. Jacklin, D. Shoesmith and D. Moser, "Characterization of commercially cold sprayed copper coatings and determination of the effects of impacting copper powder velocities," *Journal of Nuclear Materials,* vol. 466, pp. 1-11, 2015.

[54] P. Jakupi, J. Noel and D. Shoesmith, " The Electrochemical Society Intergranular Corrosion Resistance of Σ3 Grain Boundaries in Alloy 22," *Electrochemical and Solid-State Letters,* vol. 13, no. 3, 2009.

[55] D. Cui, "Preparation of Nanocrystalline High Nitrogen Stainless Steel Spherical Powders by High Energy Ball Milling," in *International Conference on Electrical and Control Engineering*, Wuhan,China, 2010.

[56] M. Cisneros, H. F. lopez, H. Mancha and E. Rincon, "Processing of Nanostructured High Nitrogen Stainless Steel by Mechanical Alloying," *Metallurgical and Materials Transactions A,* vol. 36, no. 5, pp. 1309-1316, 2005.

[57] R. Amini, E. Salahinejad, M. Hadianfard, M. Marasi and T. Sritharan, "Characterization of Fe–Cr–Mn–N amorphous powders with a wide supercooled liquid region developed by mechanical alloying," *Materials Science and Engineering A* , vol. 527, pp. 1135-1142, 2010.

[58] N. G. Razumov, A. A. Popovich and Q. Wang, "Thermal Plasma Spheroidization of High-Nitrogen Stainless Steel Powder Alloys Synthesized by Mechanical Alloying," *Metals and Materials International,* vol. 24, pp. 363-370, 2018.

[59] F. I. Alresheedi and J. E. Krzanowski, "X-ray Diffraction Investigation of Stainless Steel—Nitrogen Thin Films Deposited Using Reactive Sputter Deposition," *Coatings 10,* vol. 10, 2020.

[60] C. N. Achilles, G. W. Downs, R. T. Downs, R. V. Morris, E. B. Rampe, D. W. Ming, S. J. Chipera, D. F. Blake, D. T. Vaniman, T. F. Bristow, A. S. Yen, S. M. Morrison, A. H. Treiman, P. I. Craig, R. M. Hazen, V. M. Tu and N. Castle, "Amorphous phase characterization through x-ray diffraction profile modeling: implications for amorphous phases in gale crater rocks and soils.," in *49th Lunar and Planetary Science Conference*, 2018.

[61] J. P. Patel and P. H. Parsania, "3 - Characterization, testing, and reinforcing materials of biodegradable composites," in *Biodegradable and Biocompatible Polymer Composites*, Woodhead Publishing Series in Composites Science and Engineering, 2018, pp. 55-79.

[62] F. Borgioli, "From Austenitic Stainless Steel to Expanded Austenite-S Phase: Formation, Characteristics and Properties of an Elusive Metastable Phase," *Metals*, vol. 10, no. 2, 2020.

[63] V. K. Champagne, The Cold Spray Materials Deposition Process-Fundamentals and Applications, Elsevier Science, 2007.

[64] T. Schmidt, F. Gärtner, H. Assadi, H. Richter, T. Stoltenhoff, H. Kreye and T. Klassen, "From Particle Acceleration to Impact and Bonding in Cold Spraying," *Journal of Thermal Spray Technology,* vol. 18, pp. 794-808, 2009.

[65] C.-J. Li, W.-Y. Li, Y.-Y. Wang, Guan-JunYang and H.Fukanuma, "A theoretical model for prediction of deposition efficiency in cold spraying," *Thin Solid Films,* vol. 489, no. 1-2, pp. 79-85, 2005.

[66] J. Karthikeyan, "The advantages and disadvantages of the cold spray coating process," in *The Cold Spray Materials Deposition Process*, Woodhead Publishing, 2007, pp. 62-71.

[67] J. Villafuerte, "Considering Cold Spray for Additive Manufacturing," Advanced Materials and Processes, Windsor, 2014.

[68] V. Varadaraajan and P. Mohanty, "Design and optimization of rectangular cold spray nozzle: Radial injection angle, expansion ratio and traverse speed," *Surface and Coatings Technology,* vol. 316, pp. 246-254, 2017.

[69] S. Seethammaraju and M. Rangarajan, "Corrosion of stainless steels in acidic, neutral and alkaline saline media: Electrochemical and microscopic analysis," in *IOP Conference Series: Materials Science and Engineering,* 2019.

[70] X. Zhu and Y. Zhang, "Investigation of the Electrochemical Corrosion Behavior and Passive Film for Fe-Mn, Fe-Mn-Al, and Fe-Mn-Al-Cr Alloys in Aqueous Solutions,," *Corrosion,* vol. 54, no. 1, pp. 3-12, 1998.

[71] A. Leicht, *Aspects of Building Geometry and Powder Characteristics in Powder Bed Fusion,* Gothenburg, 2018.

[72] K. Wu, G. Liu, B. Hu, F. Li, Y. Zhang, Y. Tao and J. Liu, "Solidification Characterization of a New Rapidly Solidified Ni–Cr–Co Based Superalloy," *Materials Characterization,* vol. 73, pp. 68-76, 2012.

[73] L.N.Brewer, J.F.Schiel, E.S.K.Menon and D.J.Woob, "The Connections between Powder Variability and Coating Microstructures for Cold Spray Deposition of Austenitic Stainless Steel," *Surface and Coatings Technology,* vol. 334, pp. 50-60, 2018.

[74] A. Das, S. Sunil and R. Kapoor, "Effect of Coooling Rate on the Microstructure of a Pressure Vessel Steel," *Metallography, Microstructure and Analysis*, vol. 8, pp. 795-905, 2019.

[75] J. Roa, G. Fargas, A. Mateo and E. Jemenez-Pique, "Dependence of nanoindentation hardness with crystallographic orientation of austenite grains in metastable stainless steels," *Materials Science and Engineering: A,* vol. 645, pp. 188-195, 2015.

[76] S. Dosta, G. Bolelli, A. Candeli, L. Lusvarghi, I. G. Cano and J. M. Guilemany, "Plastic Deformation Phenomena during Cold Spray Impact of WC-Co Particles onto Metal Substrates," *Acta Materialia,* vol. 124, pp. 173-181, 2017.

[77] M. Grujicic, J. Saylor, D. Beasley, W. DeRosset and D. Helfritch, "Computational Analysis of the Interfacial Bonding between Feed-Powder Particles and the Substrate in the Cold-Gas Dynamic-Spray Process," *Applied Surface Science,* pp. 211-227, 2003.

[78] A. Moridi, Powder Consolidation Using Cold Spray, 2017: Springer International.

[79] B. Dikici, H. Yilmazer, I. Ozdemir and M. Isik, "The Effect of Post-Heat Treatment on Microstructure of 316L Cold-Sprayed Coatings and Their Corrosion Performance," *Journal of Thermal Spray Technology,* vol. 25, no. 4, pp. 704-714, 2016.

[80] A. Brnabic and L. M. Hess, "Systematic literature review of machine learning methods used in the analysis of real-world data for patient-provider decision making," *BMC Medical Informatics and Decision Making,* vol. 21, 2021.

[81] E. W. Steyerberg, Clinical Prediction Models-A Practical Approach to Development, Validation, and Updating, Springer, 2019.

[82] S. A. Razvi, S. C. Feng, A. N. Narayanan, Y.-T. T. Lee and P. W. Witherell, "A Review Of Machine Learning Applications In Additive Manufacturing," in *International Design Engineering Technical Conferences & Computers and Information in Engineering Conference*, 2019.

[83] M. Mani, B. M. Lane, M. A. Donmez, S. C. Feng, S. P. Moylan and R. R. F. Jr., "Measurement Science Needs for Real-time Control of Additive Manufacturing Powder Bed Fusion Processes," NIST Interagency/Internal Report (NISTIR), 2015.

[84] Z. L. Lu, D. C. Li, B. H. Lu, A. F. Zhang, G. X. Zhu and G. Pi, "The prediction of the building precision in the Laser Engineered Net Shaping process using advanced networks," *Optics and Lasers in Engineering,* vol. 48, no. 5, pp. 519-525, 2010.

[85] S. H. Zahiri, D. Fraser, S. Gulizia and M. Jahedi, "Effect of Processing Conditions on Porosity Formation in Cold Gas Dynamic Spraying of Copper," *ASM International*, vol. 15, pp. 422-430, 2006.

[86] S. W. Glass, M. R. Larche, M. S. Prowant, J. D. Suter and J. P. Lareau, "Cold spray NDE for porosity and other process anomalies," in *AIP Conference Proceedings*, 2018.

[87] J. W. Murray, M. V. Zuccoli and T. Hussain, "Heat Treatment of Cold-Sprayed C355 Al for Repair: Microstructure and Mechanical Properties," *Journal of Thermal Spray Technology*, vol. 27, pp. 159-168, 2018.

[88] Y. Wang, J. Adrien and B. Normand, "Porosity Characterization of Cold Sprayed Stainless Steel Coating Using Three-Dimensional X-ray Microtomography," *MDPI-Coatings*, vol. 8, 2018.

[89] H. Fukanuma and N. Ohno, "A Study of Adhesive Strength of Cold Spray Coatings," in *ASM International*, 2004.